Iowa State University
Digital Repository

2008

Production of a new wastewater treatment coagulant from fly ash with concomitant SO2 removal from flue gas

Ling Li
Iowa State University

Recommended Citation

Li, Ling, "Production of a new wastewater treatment coagulant from fly ash with concomitant SO2 removal from flue gas" (2008). *Retrospective Theses and Dissertations*. 15655.
https://lib.dr.iastate.edu/rtd/15655

Production of a new wastewater treatment coagulant from fly ash with

concomitant so$_2$ removal from flue gas

by

Ling Li

A dissertation submitted to the graduate faculty

in partial fulfillment of the requirements for the degree of

DOCTOR OF PHILOSOPHY

Major: Civil Engineering (Environmental Engineering)

Program of Study Committee:

J. (Hans) van Leeuwen, Co-major Professor
Jacek A. Koziel, Co-major Professor
Robert C. Brown
Shihwu Sung
Samir S. Khanal

Iowa State University

Ames, Iowa

2008

UMI Number: 3307082

INFORMATION TO USERS

The quality of this reproduction is dependent upon the quality of the copy
submitted. Broken or indistinct print, colored or poor quality illustrations and
photographs, print bleed-through, substandard margins, and improper
alignment can adversely affect reproduction.

In the unlikely event that the author did not send a complete manuscript
and there are missing pages, these will be noted. Also, if unauthorized
copyright material had to be removed, a note will indicate the deletion.

UMI®

TABLE OF CONTENTS

LIST OF FIGURES

LIST OF TABLES

ACKNOWLEDGEMENTS

This project was conducted under the direction of my major professor, Dr. J (Hans) van Leeuwen, I appreciate all his help and support through my research. I would also like to thank my previous advisor, Dr. Maohong Fan for his directions on experimental design and valuable suggestions on my dissertation. I also thank Dr. Robert C. Brown for his great help in providing space and equipment for the experimental needs. I would also thank Dr. Lingshuang Cai, Dr. Warren E. Straszheim and Dr. Basudeb Saha for their help in the analysis of samples. In addition, I would express my gratitude to Dr. Jacek A. Koziel, Dr. Shihwu Sung, Robert Brown, and Dr. Samir Khanal for their suggestion on my research and dissertation.

Finally, I would like to express my deepest appreciation to my family members, for all their support and encouragement during these years.

ABSTRACT

Sulfur dioxide (SO_2) is one of major air pollutants emitted from coal combustion. When it is emitted into the environment, it imposed many adverse health and environmental impacts, such as impairment of respiratory system, reduction of visibility and acid rain. Traditional sulfur dioxide removal technologies have the disadvantages disposal of large amount of by-products with low market value.

Fly ash, a by-product of coal combustion rich in iron and aluminum oxides and sodium chlorate as an oxidant were utilized in this project to produce a complex coagulant with the removal of sulfur dioxide in simulated flue gas. Conversion efficiency of iron and aluminum oxides in fly ash was temperature dependant. The removal efficiency of sulfur dioxide was influenced by reaction temperature, diffusing method, and sulfur dioxide initial concentration. The produced complex coagulant performed better in the removal of total suspended solid (TSS) and turbidity in wastewater treatment.

Investigations of reaction kinetics showed that the reaction orders of iron and aluminum oxides under the same reaction temperature are the same. Empirical Arrhenius expressions were derived based on rate constants at each reaction temperature. Reaction kinetics of iron and aluminum oxides in ground and unground fly ash were compared and analyzed. The mass transfer process of sulfur dioxide absorption was semi-quantified using a film model.

CHAPTER 1. INTRODUCTION

During coal combustion, a major harmful gas in flue gas released to the air is SO_2, which has become a worldwide problem. The conventional flue gas cleaning method involves wet or dry scrubbing with lime or limestone. The disadvantage of this kind of technique is the discharge of large amount of waste slurry containing calcium sulfite and sulfate, which has very little value for any further application and is usually disposed of in landfills.

Fly ash is a by-product of coal combustion. Typically, it contains mixtures of sulfates, oxides, and silicates. Iron, aluminum and silicon are the major elements in fly ash while other minor compounds, like calcium, magnesium, sodium, potassium are also present. A large percentage of fly ash goes disposed in landfilling. However, landfilling of fly ash wastes land resources and may increase the amount of particulate materials in the air during windy conditions. Fly ash is rich in aluminum and iron oxides, which are essential raw materials for the production of water and wastewater treatment coagulants. Therefore, extraction of iron and aluminum oxides from fly ash makes it possible to use a waste material for wastewater treatment.

This project is aimed at producing a wastewater treatment coagulant with the removal of SO_2 with fly ash and an oxidant.

This dissertation includes five chapters and an appendix.

Chapter 1 is a general introduction. Chapter 2 describes SO_2 reduction technologies and application of fly ash as a review paper submitted to Power Plant Chemistry.

Chapter 3 describes investigations into the influencing factors of Fe_2O_3 and Al_2O_3 conversion efficiency, and SO_2 removal efficiency. Chapter 3 also evaluates the performances of the produced complex coagulant in wastewater treatment. Chapter 4 presents studies on reaction kinetics of Fe_2O_3 and Al_2O_3 in fly ash with H_2SO_4 and mass transfer evaluation of SO_2 absorption. Chapter 3 and Chapter 4 have both been submitted as publications to Journal of Hazardous Materials. Chapter 5 is a conclusion, summarizing the findings in Chapter 3 and 4, and provides some recommendations for future research. Appendix is a review paper about applications of iron based nanoparticles in environmental remediation published in Critical Review in Environmental Science and Technology.

CHAPTER 2. REDUCTION OF SULFUR EMISSIONS IN FLUE GAS AND APPLICATIONS OF FLY ASH FROM POWER PLANTS: A REVIEW

A paper submitted to Power Plant Chemistry

Ling Li, Maohong Fan, Robert C. Brown, Jacek A. Koziel, J(Hans) van Leeuwen

2.1 ABSTRACT

Flue gas and fly ash are the two most important wastes from power plants. This review focuses on technologies for SO_2 removal from emissions and on properties and applications of fly ash. Flue gas desulfurization (FGD) technologies are the most commonly used methods in the removal of SO_2 in flue gas. Influencing factors of SO_2 removal efficiency and optimal operation conditions are considered. Physical and chemical properties of fly ash make it possible to be used in various fields, such as cement production, concrete admixtures, soil amendment, low-cost adsorbent of certain types of contaminants in wastewater and production of effective wastewater coagulants.

2.2 INTRODUCTION

Since all fossil fuels contain a certain amount of sulfur, ranging from 0.1-5% [1], significant amounts of SO_2 are emitted from power plants following oxidation during combustion. Emission of SO_2 from fossil fuels is the major contributor to acid rain,

which causes material damage, and acidification of natural water bodies and soil.
Such acidification could be a disaster for many aquatic life forms, soil fertility and
plant diversity. SO_2 can undergo complex photochemical reactions to form
light-scattering aerosols, the main concern of which is the impairment of visibility.
Investigations estimate that 0.1 ppm SO_2 with 50% relative humidity could reduce the
visibility to 5 miles [2].

Legislation to controls SO_2 emissions, desulfurization of power plant flue gases and
removal of sulfur from crude oil and coals has contributed to the decline of SO_2
emissions over the past 30 years. However, SO_2 emissions still total over 60 million
metric tons in 2000 worldwide [3]. In the United States, although the emission of SO_2
has been decreased by one third over the past 30 years, the amount was still more than
20 million tons in 2000, 75-80% of which was released during fuel combustion [4].
Since fuel-fired power plants are responsible for most of the SO_2 emissions, it is
important to reduce SO_2 concentrations in these flue gases.

Another important waste from power plants is fly ash, which is a fine particulate
material that is produced by the combustion of pulverized coal and carried out by flue
gas. Coal fired power plants produce significant amounts of fly ash each year.
According to the American Coal Ash Association (ACAA) data, combustion of coal
in the United States alone produced approximately 68 million tons of fly ash in 2001
[5]. Fly ash contains primarily oxides of Si, Al, Fe and Ca, with smaller concentration
of Na, K, Mg, Ti, sulfate and various trace elements. The chemical properties of fly
ash make it possible to be used in many fields, such as construction, highway

applications and agriculture. Currently, over 20 million tons of fly ash finds useful application annually in the United States [5]. However, 70-75% fly ash generated is still disposed in landfills. Considering landfill space limitations and transportation cost, and in addition water pollution through leachates, landfilling is not a good solution for fly ash disposal. Some researchers observed trace elements leaching from fly ash, resulting in ground water and soil contamination [6]. In addition, the transportation and disposal of fly ash will increase particulate material concerns in the air during windy days. This paper provides a review on sulfur removal technologies and the useful application of fly ash from power plants.

2.3 SO$_2$ REMOVAL TECHNOLOGIES

Possible measures that may be used to control SO$_2$ emissions from fuel combustion include burning low-sulfur fuels, reducing sulfur content in the feed, and emission control technologies. Low-sulfur fuels such as natural gas, low-sulfur oil and low-sulfur gas are not easily available and relatively expensive. Therefore, these fuels may not be economically viable alternatives. For high-sulfur coals, blending with low-sulfur coals can reduce the total sulfur content to meet the limit of SO$_2$ emissions [7-9]. There are different models predicting the appropriate blending quantities of coals with different sulfur contents [10-13]. Although a number of linear or non-linear models can be used to determine the predicted sulfur content, it is still difficult to optimize the combustion conditions simply based on the model. In addition to sulfur content, many other characteristic parameters, such as heating value, ignition

temperature, burnout efficiency, and ash content, also need to be considered [7]. Due

to its complexity, it is difficult to optimize each parameter in a blended coal.

Therefore, a case-by-case investigation is needed in order to determine suitable

blending conditions. Considering the cost of low-sulfur coals, a reasonable ratio of

coal price to sulfur content needs to be introduced.

The most commonly accepted SO_2 emission control method is flue gas desulfurization

(FGD). There are mainly two categories of FGD systems: dry and wet FGD systems,

which are defined simply by whether or not the active reagent is added in liquid

slurry.

2.3.1 DRY FLUE GAS DESULFURIZATION (DRY FGD)

2.3.1.1 DRY FGD PROCEDURE

Dry powdered sorbent is injected into the furnace in conjunction with pulverized coal

or combustion gas in the dry FGD systems. In general, SO_2 removal efficiency of dry

FGD is in the range of 40-60%. It is known that $CaCO_3$ decomposes rapidly at 800 °C,

and the produced CaO can react with SO_2 to form $CaSO_3$ and $CaSO_4$, resulting in the

reduction of SO_2. Therefore, lime or limestone is usually blended with the coal as a

SO_2 sorbent [11, 14]. In conventional furnaces, the combustion temperature is usually

higher than 1200 °C. At such a high temperature, the thermal instability of sulfate

products has to be considered in the control of SO_2 removal efficiency. In addition,

the short residence time of SO_2 and/or H_2S in the coal bed makes it an inefficient

contact between the gas phase and the solid sorbent [7]. Studies showed that simply

blending limestone or lime with pulverized coal results in the removal of 15-20% only

of sulfur in conventional furnaces, which would not meet the SO_2 removal

requirement, at least 70% to achieve a SO_2 emission rate less than 0.6 lb/10^6 BTU or

90% to achieve a SO_2 emission rate less than 1.2 lb/10^6 BTU [15, 16]. Injecting the

sorbents into the combustion gas can achieve a higher SO_2 removal efficiency [17-19].

Generally, SO_2 removal efficiency by this method is about 40-60% [7]. Further

investigations demonstrated that blending $CaCO_3$ with pulverized coal was only able

to remove 26.6% SO_2, however, injecting it directly with the combustion gas

improved the SO_2 removal efficiency to 56.6% [20]. A two-stage desulfurization

process showed that combining sorbents with feed coal and injecting them into

combustion gas could improve SO_2 removal efficiency to about 75% [21]. An

application of the combined two-stage desulfurization process gave an in-furnace SO_2

removal of 75-77% and a total SO_2 removal of 85-90% [22, 23].

2.3.1.2 INFLUENCING FACTORS OF DRY FGD

The influencing factors on sulfur removal efficiency in the sorbent injection process

include Ca/S ratio, injection location, particle size and structure of the sorbents, and

temperature. The optimal molar ratio of Ca/S is 2 and it is suggested to be maintained

in a very limited range [7]. Further increase of Ca/S ratio has little benefit. Studies on

the influence of Ca/S ratio on SO_2 removal showed that when the molar ratio of Ca/S

was increased from 2 to 6, the SO_2 removal efficiency was improved only by 1% from

23% to 24% [21]. The SO_2 removal efficiency was reported to increase as the sorbent

particle sizes decrease in a certain range [7]. At Ca/S ratio of 2, a decrease in sorbent

particle size from 10μm to 1μm improved SO_2 removal from 40% to 50% [24].

Ultrafine sorbent particles (d< 1μm) can be beneficial in increasing the reaction rate of the combustion process. However, grinding cost, destruction of pore volume and increase of diffusion resistance inside the particles should be considered. Therefore, the optimal sorbent particle size in an injection process is suggested to be approximately 5μm [7]. The porosity structure of the sorbent particles also has an important impact on SO_2 removal in the limestone injection process. Suitable pore size distribution is reported to be effective in providing more surface area, which contributes higher sorbent reactivity and higher CaO conversion [25]. It was reported that for sorbents with particle sizes in the range of 1-5 μm, pore diameters of 5-30 nm are desirable [26]. Temperature also affects SO_2 removal. A limestone sorbent can effectively capture SO_2 at 700-800 ℃, but it has a low efficiency in absorbing SO_2 at lower temperatures. At high temperature, the thermal instability of sulfate products can be a big concern in the removal of SO_2 [7].

2.3.1.3 IMPROVEMENTS OF DRY FGD

Some studies showed that by adding proper amounts of clay minerals, including silicates together with limestone into the blended coal, the desulfurization efficiency of limestone can be improved in a certain temperature range [27, 28]. Although certain kinds of clay minerals can improve the SO_2 removal efficiency, other clay minerals such as bentonite and zeolite have every little effect on improving sulfur removal [29]. Further investigation on zeolites found that it emits sulfur VOCs, which could have an adverse effect on SO_2 removal [30].

Application of a fluidized bed, together with dry scrubbing could increase SO_2 removal efficiency greatly. Investigation showed that dry scrubbing with limestone in a fluidized bed removed more than 90% of SO_2 from the original concentration of 5000 ppm [31].

In some FGD processes, the flue gas is contacted with a fine mist of sorbent slurry. These processes are sometimes referred to as semi-dry or wet-dry scrubbing. Since the fly ash in such systems is not removed prior to the scrubber, the flue gas leaving the scrubber contains both fly ash and sorbent particles. Therefore, a particulate collection system such as baghouse or fabric filter is needed. The removal efficiency of SO_2 in a semi-dry system can be as high as 80% when a sufficient amount of sorbent is injected. In addition, when fabric filter is applied, SO_2 removal efficiency can be improved to over 90% [1]. In semi-dry FGD systems, ammonia can also be used as the sorbent instead of lime or limestone in dry FGD systems. Both bench-scale and pilot-plant tests showed that reduction with NH_3 can remove SO_2 from flue gas effectively [32, 33]. However, SO_2 removal efficiency is sensitive to the NH_3/SO_2 ratio and reaction temperatures [33, 34]. It was reported that over 95% SO_2 removal was achieved when NH_3 was injected into the combustion gas at a NH_3/SO_2 molar ratio of slightly less than 2 and at a temperature range of 54-85 ^{o}C [35]. However, the amount of solid waste produced in dry FGD systems is a serious concern. A 1000 MW power plant using a fluidized bed dry scrubbing system could produce 800,000 tons of solid particles each year to be disposed of [1].

2.3.2 WET FLUE GAS DESULFURIZATION (WET FGD)

2.3.2.1 WET FGD PROCESS AND INFLUENCING FACTORS

Over 70% of FGD systems in the United States use the wet FGD method [36]. Wet

FGD is also increasingly recognized as a multi-pollutant control method. It can

achieve high removal efficiency of acid gases, including SO_2, fine particulate matter

and heavy metals, such as mercury. The flue gas containing SO_2 enters a spray tower

or absorber where it is in contact with lime or limestone slurry. Lime or limestone in

the slurry reacts with SO_2 to form insoluble calcium sulfite. In order to make

commercially valuable calcium sulfate (gypsum) from a wet FGD process,

compressed air is bubbled through the sulfite slurry to oxidize sulfite to sulfate. This

procedure is known as forced oxidation. Both lime and limestone wet scrubbing can

achieve over 90% SO_2 removal efficiency for both high and low sulfur coals, some of

them as high as 99% [37]. Considering the cost of the material, limestone is more

popular for large FGD systems since it is cheaper than lime [38]. Under given

operation conditions, SO_2 removal efficiency depends on the limestone content in the

slurry and limestone characteristics. It was reported that limestone with smaller

particle sizes performed better in SO_2 removal. That is because smaller particles can

be slurried more easily, resulting in increased the reactivity of limestone [38]. Studies

on using coarse granular limestone as sorbent in wet FGD process showed that the

slurry consumption was much higher than that of using fine particle limestone [39].

Further analysis of limestone structures by scanning electron microscopy (SEM) and

X-ray diffraction (XRD) showed that limestone with higher purity had a better

dissolution rate [38]. The ratio of the recycled slurry used to absorb flue gas and flue

gas flow rate (L/G) and pH of the slurry have great impacts on SO_2 removal and

operation cost. A good design could minimize L/G ratio, thus minimizing slurry and

power consumption. The optimum pH value is suggested to be ranging from 5.5 to 5.7

and Ca/S ratio ranging from 1.03 to 1.05 in wet FGD systems [40].

2.3.2.2 IMPROVEMENTS OF WET FGD

Earlier studies found that organic acids with buffering capacity would enhance the

dissolution of limestone in the acidic slurry [41]. Further investigations showed that

certain types of dibasic organic acids, including adipic acid, glutaric acid, and

succinic acid are capable of providing good buffering and forced oxidation [42]. It is

important to maintain the pH value in the optimum range in wet FGD systems. Since

the concentration of SO_2 in the spray tower or absorber changes as the reaction goes

on, the pH fluctuates accordingly. Therefore, adding organic acids with good

buffering capacity can help in maintaining the pH in the optimal range for SO_2

absorption. A recent study showed that adding acetic acid greatly improved SO_2

removal efficiency. When granular limestone was used directly as the sorbent, only

60.7% SO_2 was removed. However, when 10 mmol/L acetic acid was used, the

removal efficiency of SO_2 was improved to 87% under the same operation conditions

[43].

One problem of wet FGD with lime or limestone is that scaling occurs inside the

scrubber and reduces SO_2 removal efficiency. The addition of $MgSO_4$ and $MgSO_3$

could not only reduce scaling but also increase SO_2 removal efficiency [44]. Wet

FGD systems also have disposal problems for the slurry since the by-products are of low market value and need to be disposed in a landfill.

In some coastal power plants, seawater has been successfully utilized to absorb SO_2. Because seawater is alkaline in nature, it has some neutralizing capacity with respect to the acidification caused by the absorption of SO_2. After SO_2 absorption in seawater, the effluent flow is aerated to oxidize sulfide to sulfate, which is a natural ingredient in seawater. When the seawater containing sulfate is returned to the sea, the increase of sulfate is within natural variations. In addition, with the active sulfur bacteria, sulfates in seawater are converted to sulfides, which can be fixed into organic materials [45]. In seawater FGD systems, no solid waste is produced, but this advantage is only available in power plants along the coast.

Table 2.1 summarizes dry and wet FGD systems by SO_2 removal efficiency and influencing factors.

2.3.3 OTHER FLUE GAS DESULFURIZATION TECHNOLOGIES

Circulating fluidized-bed absorber (CFBA) is another SO_2 removal technology. In CFBA systems, the humidified flue gas flows through the fluidized bed containing sorbent particles, typically slaked lime. The CFBA unit is usually followed by particulate collection equipment [46]. Ollero et al. conducted a pilot-plant study at a 500 MW power plant. The SO_2 concentration in the flue gas was 350-3000 ppm. Their results showed that high SO_2 removal efficiency (95 to 97%) and high sorbent utilization can be reached under suitable operating conditions.

Pulsed corona and dielectric barrier discharges are plasma based SO_2 removal technologies aimed at oxidizing SO_2 in the gas phase. In plasma based SO_2 removal systems, SO_2 is oxidized to SO_3 or H_2SO_4 by either free O or OH radicals, which are dissociated from SO_2 itself or moisture by plasma [47, 48]. Experimental investigations showed that SO_2 removal efficiency can be greater than 80% for a simulated flue gas stream containing 1000 ppm SO_2 [47]. Sun et al. [49] further proved that the dielectric barrier discharge technology was capable of removing up to 99% SO_2 under low concentrations (400 ppm) and suitable moisture content. Although pulsed corona discharge is effective in removing SO_2, there are two disadvantages, which are high-energy requirement and non-uniformity produced oxidizing radicals [50].

When SO_2 is present in the air, it is a pollutant that needs to be removed; on the other hand, SO_2 can be used as an important raw material in industry. SO_2 can be converted to sulfuric acid by oxidation. Sulfuric acid has wide application in producing sulfur containing fertilizers, such as superphosphate of lime and ammonium sulfate, or sodium sulfate, which is an important chemical in the soap, paper and glass industries [51, 52]. Shi et al. used SO_2 in acetic acid and lactic acid recovery from calcium acetate and calcium lactate solutions. Their investigation demonstrated that the recovery processes of acetic acid and lactic acid by SO_2 at room temperature are applicable [53, 54]. Fan et al. developed an effective SO_2 removal method aiming at producing polymeric ferric sulfate (PFS), a commonly used water treatment coagulant, at the same time [55, 56].

Table 2. 1 Summary of dry and wet flue gas desulfurization (FGD) systems

FGD Process	SO$_2$ removal, %	Optimal values of operating parameters	Ref.	Improvements and benefits	Ref.
Dry FGD	40-60	Ca/S ratio: 2	7, 21	Two stage dry FGD: increases SO$_2$ removal to 85-90%	22, 23
		Sorbent particle size: 1-5 μm	7, 25, 26	Fluidized bed: increases SO$_2$ removal to over 90%	31
		Sorbent pore diameter: 5-30 μm	26	NH$_3$ injection: increases SO$_2$ removal to over 95% and reduces slurry production in semi-dry FGD systems	32-35
		Temperature: 700-800 ºC	7		
Wet FGD	>90	L/G ratio: minimized	40	Buffer with certain kinds of organic acids: helps in maintaining pH in the optimal range	41-43
		Ca/S ratio: 1.03-1.05	40	Add MgSO$_4$ and MgSO$_3$ helps in reducing scaling problems	44
		pH: 5.5-5.7	40	Sea water absorption: no solid waste is produced	45

2.4 PROPERTIES AND APPLICATIONS OF FLY ASH

2.4.1 FLY ASH PROPERTIES

2.4.1.1 PHYSICAL PROPERTIES OF FLY ASH

Fly ash is a fine particulate material that is produced by the combustion of pulverized coal and carried out by flue gas. The characteristics of fly ash can vary in a wide range among combustion methods, coal sources, and particle shape. The color of fly ash varies from tan to dark gray, depending on the chemical components. Light colored fly ash typically indicates high lime content. Reddish or brownish color is associated with iron content and dark gray colored fly ash usually has unburned

carbon contents, as measured by the loss on ignition (LOI). Normally, fly ash particles

are of spherical shape and exhibit smooth surface texture. Giere et al. [57]

investigated the micro and nano-chemistry of fly ash particles and found that the

single fly ash particles are either hollow or filled with a serious of smaller particles.

The size of most fly ash particles is in the range of 0.01 to 0.1 mm. This size range

and the sphere shape improve the fly ash fluidity, which contributes to a cementing

effect (pozzolanic activity), meaning that it will react with free lime and water to

produce cementitious compounds. The American Society of Testing Materials

(ASTM) classifies fly ash as Class C or Class F mainly based on calcium oxide

content. Class C is generally produced from sub-bituminous coal and contains more

than 20% CaO, and Class F is usually derived from bituminous and anthracite coals

and has less than 10% CaO [5]. Class C is self-cementing since it contains enough

CaO. For Class F fly ash, additional lime is usually added if it is used in producing

cements [58]. Fly ash usually has a bulk density of 1.01-1.43 g/cm^3, and specific

gravity of 1.6-3.1g/cm^3. Investigations on 23 fly ashes from across the United States

showed that the pH range was from 4.2 to 11.8 [5]. The pH of fly ash depends largely

on the sulfur content of the parent coal. Eastern coals in the U. S contain high sulfur

contents and produce acidic fly ashes and western coals are low in sulfur, producing

alkaline fly ashes [59].

2.4.1.2 CHEMICAL PROPERTIES OF FLY ASH

The chemical composition of fly ash depends greatly on the mineral chemistry of the

coal sources, additives used in the combustion or post-combustion processes, and the

pollution control technologies [5]. Fly ash contains primarily oxides of Si, Al, Fe and

Ca, with smaller concentration of Na, K, Mg, Ti, sulfate and various trace elements.

Table 2.2 gives a normal range of chemical compositions of fly ash produced from

different coal sources. X-ray diffraction (XRD) was used in measuring the fly ash

structure quantitatively and it was found out that the most abundant crystalline phases

in fly ash are quartz, mullite, ferrite spinel, anhydrite and lime. Mullite is an

aluminosilicate crystalline compound, which has a composition ranging from

$3(Al_2O_3) \cdot 2(SiO_2)$ to $2(Al_2O_3) \cdot 3(SiO_2)$ [60]. Among those, quartz and mullite are the

major crystalline phases [6].

Table 2. 2. Normal percent range of chemical composition of fly ash [7]

Compounds	Bituminous (%)	Sub-Bituminous	Lignite (%)
SiO_2	20-60	40-60	15-45
Al_2O_3	5-35	20-30	10-25
Fe_2O_3	10-40	4-10	4-15
CaO	1-12	5-30	15-40
MgO	0-5	1-6	3-10
SO_3	0-4	0-2	0-10
Na_2O	0-4	0-2	0-6
K_2O	0-3	0-4	0-4
LOI	0-15	0-3	0-5

2.4.2 APPLICATIONS OF FLY ASH

Coal fired power plants produce significant amounts of fly ash each year. According

to the ACAA data, combustion of coal in the United States alone produced

approximately 68 million tons of fly ash in 2001 [5].

Some European countries, such as Germany and the Netherlands, utilize fly ash to almost 100% [61]. The United States uses considerably less: about 70 to 75 % of fly ash generated is disposed of in landfills. However, considering landfill space limitations and transportation cost, landfilling is a poor solution to fly ash disposal. In addition, the transportation and disposal of fly ash will increase particulate material concerns in the air during windy days. Moreover, much of the fly ash is capable of being reused, it may find applications in many fields, such as construction, highway applications and agriculture. Currently, over 20 million tons of fly ash is used annually in the United States [5]. The fly ash produced in 2001 as an example, 22 million tons, or about 30% of the total fly ash production was used, over 60% of which used in producing cement and concrete [5].

2.4.2.1 APPLICATION OF FLY ASH IN CEMENT AND CONSTRUCTION

Fly ash is rich in siliceous or siliceous and aluminous materials, which could react with $Ca(OH)_2$ at ordinary temperatures to produce cementitious compounds in the presence of water. There are specific criteria for fly ash suitability in cement/concrete applications. First of all, fly ash has to meet the fineness requirement, since the rate of pozzolanic activity and the workability of the concrete are affected greatly by the fly ash particle size. A minimum of 66 percent passing the 0.044 mm sieve is required by ACAA [5]. Chemical composition is also important. Since the chemical composition of fly ash varies from site to site, the reactive aluminosilicate and calcium aluminosilicate (represented as SiO_2, Al_2O_3 and CaO) components should be checked regularly to meet the criteria. The content of SO_3 should be limited to 5% and

available alkalis should not exceed 1.5 % [5]. High LOI (unburned carbon) is not

desired. Traditionally, Class C or high calcium fly ash is added into Portland cement

to improve some of the cementitious properties, such as increase ultimate strength,

durability, chemical resistance, reduced permeability [5, 62]. The EPA headquarters

in Washington D.C. was constructed with cement containing fly ash. Fly ash concrete

was used in severe exposure applications such as the decks and piers of the Sunshine

Skyway Bridge in Tampa Bay, Florida.

Recent research showed considerable interest in converting fly ash into cementitious

materials without Portland cement. Rostami and Brendley used low carbon Class F fly

ash, sand, gravel, which were mixed together with sodium hydroxide, sodium silicate

solutions to make concrete [61]. Their results showed that compared to Portland

cement, the fly ash based cement had higher ultimate strength, better acid resistance,

and better freeze-thaw durability. A variety of new technologies have been developed

for manufacturing fly ash-based cement, in which fly ash, a calcium (or magnesium)

reinforcing solution, and a modifier are used as the raw materials [63-67]. Yoon and

Yun introduced a new method to produce a glass-ceramic from fly ash and waste

glass. Proper mixing ratio and temperature will generate practical glass ceramic with

good mechanical strength and bending strength [68]. Mohanty and Chugh developed a

new method of making automotive brake lining using fly ash and other ingredients. In

their research, the brake lining raw material contains more than 50% fly ash. The fly

ash based brake lining is 50 to 60% lighter in weight than current commercial

materials for similar friction [69].

2.4.2.2 APPLICATION OF FLY ASH IN SOIL MODIFICATION

Although applications of fly ash in soil modification and agriculture are not very popular yet, it has been proven that fly ash can be used to improve the physical and chemical properties of coarse or sandy soils [58, 70-73]. Since fly ash is comprised mostly of silt-sized particles, it can be used to improve the coarse-textured soils and increase the soil moisture holding capacity, which is helpful in increasing plant growth. Pathan et al. investigated the properties changes of soils by mixing different amount of fly ash with it. Their results showed that with a proper fly ash to soil ratio, the water holding capacity was increased three times, which could increase plant growth [73]. Depending on its pH, fly ash can be either acidic or alkaline, which makes it useful in modifying the pH of soils [72, 75]. This is especially useful when alkaline fly ash is added to neutralize acidic soils [71]. Beside oxides of Si, Al, Ca and Fe, fly ash also contains smaller amount of P, N, K, Na, Mg, which makes it potentially useful as a fertilizer supplement [75]. A 4-month greenhouse experiment showed that application of 20% and 40% fly ash with soil increased the yield of rice significantly [76]. Another two-year field experiment found that when fly ash is combined with chemical fertilizer, the uptake of N, P, K and other nutrients were higher, resulting in higher crop yield [75]. An investigation on fly ash as a soil amendment and fertilizer conducted by Kalra et al. showed similar results [70]. The most important concern of using fly ash as a soil amendment is the possible release of trace elements. The toxicity characteristic leaching procedure (TCLP) experiments indicated that the potential for release harmful trace element was below U.S. EPA

regulatory levels and did not prove to impose adverse effects on plant growth [58, 73].

However, the composition of fly ash varies from site to site, laboratory evaluation of

physical and chemical properties should be conducted prior to the use of fly ash for

soil amendment.

2.4.2.3 APPLICATION OF FLY ASH IN ENVIRONMENTAL REMEDIATION

Fly ash has been used as a low-cost adsorbent in the removal of dyes in industrial

wastewater [77-80]. Mohan et al. investigated the effects of different factors, such as

temperature, pH value, fly ash particle sizes and adsorbent doses on the adsorption

procedure. Their findings showed that the adsorption of the dye increased with

increasing temperature and was inversely proportional to the particle size of fly ash

[78]. Dyeing effluents from textile industry imposes great threats to the environment

since it contains highly toxic metal complexes [79]. Chatterjee et al. investigated the

adsorption and photocatalysis of dye removal from textile wastewater using fly ash

and sunlight. Their results revealed that the capacity of fly ash adsorption of dyes was

very good and Fe(III) in the fly ash acted as a photocatalyst in breaking down dye

molecules to non-hazardous products [80]. Ravikumar et al. used a mixture of 1:1

carbon and fly ash in the adsorption of dyes and found out that under optimum

conditions, complete removal was achieved [81]. Alkaline fly ash can also be used in

improving phosphate removal of sand infiltration system [82].The fly ash used in this

research contained high calcium concentration, thus the precipitation of phosphate

with calcium can be enhanced. Moreno et al. [83] used fly ashes from power plants to

synthesize zeolite, which was successfully used in purifying acid mine waters.

The U.S. EPA confirms that fly ash from coal combustion does not need to be regulated as a hazardous waste. However, it may still impose some environmental concerns since fly ash from different sources may contain different trace elements, such as Ni, V, As, Be, Cd, Ba, Cr, Cu, Mo, Zn, Pb, Se and Ra. Though these elements are usually found in extremely low concentrations, their presence should be considered in the fly ash applications.

Based on the fact that fly ash is rich in aluminum and iron oxides, which are essential raw materials for the production of water and wastewater treatment coagulants, and sulfur dioxide can be oxidized to sulfur trioxide, which can be used in making sulfuric acid, our research group conducted a project aimed at removal of sulfur dioxide with fly ash and sodium chlorate as an oxidant with production of a wastewater treatment coagulant. The results showed that the produced coagulant containing both polymeric ferric sulfates (PFS) and polymeric aluminum sulfates (PAS) performed well in the removal of total suspended solid (TSS) and turbidity. At the same time, SO_2 was removed effectively by reacting with sodium chlorate in the fly ash slurry [84]. This investigation provided a possible application of the two important power plant wastes, fly ash and flue gas.

2.5 CONCLUSIONS

This review deals with the most recent SO_2 removal technologies for flue gas and applications of fly ash from power plants. Dry and wet FGD systems are the most commonly accepted SO_2 emission control methods. In dry FGD systems, dry

powdered lime or limestone is injected directly with pulverized coal or into the combustions gas. Although the desulfurization system is relatively simple, dry FGD is only able to remove 40 to 60% of SO_2. Only a small part of the sorbent can be utilized due to the thermal instability of sulfate products at high temperatures and low reaction rate of the combustion procedure. The Ca/S ratio, sorbent particle sizes and pore size distribution of the sorbent particles also play important roles in the removal of SO_2. Suitable values for Ca/S ratio and particle size of the sorbent are 2:1 and 5μm respectively. Increasing the Ca/S ratio beyond this has very limited benefits to the removal of SO_2. In wet FGD systems, the equipment cost is relatively high because a spray tower or an absorber is needed. However, over 90% of the SO_2 can be removed for both lime and limestone sorbent. The ratio of the recycled slurry and flue gas flow rate (L/G) and pH of the slurry are the most important impact factors on SO_2 removal and operation cost. Minimum L/G ratio is desired to minimize slurry and power consumption. Optimum pH value is suggested to be 5.5 to 5.7 and Ca/S ratio is 1.03 to 1.05. Certain kinds of dibasic organic acids are helpful in increasing SO_2 removal under certain operation conditions. Main problems caused by wet FGD include scaling and disposal of the low market value slurry. Circulating fluidized-bed absorber (CFBA) and plasma based SO_2 removal technologies are also available on the market. These new technologies are able to remove SO_2 up to 99%. However, energy consumption and equipment cost should be considered. It was reported that SO_2 can also be used as the raw material to produce sulfuric acid, sulfur containing fertilizers, and polymeric ferric sulfate, a wastewater treatment coagulant. It also can

be used in the recovery of acetic acid and lactic acid recovery from calcium acetate and calcium lactate solutions.

Most fly ash is disposed in landfilling in the United States. However, fly ash can find applications in many fields due to the complicated physical and chemical properties. In general, fly ash is rich in oxides of Si, Al, Fe and Ca, with smaller concentration of Na, K, Mg, Ti and sulfate. The siliceous or siliceous and aluminous components in fly ash make it possible to react with $Ca(OH)_2$ to produce cementitious compounds in the presence of water. Studies showed that fly ash based cements and ceramic materials have better performance in various applications. Particle size and chemical composition are the two most important factors impacting the production of fly ash based cementitious materials. Because of the silt-sized particles and minor nutrient compounds such as P, N, K, Na, Mg, fly ash can also be used as soil modification and fertilizer supplements to improve the physical and chemical properties of coarse or sandy soils. Proper fly ash to soil ratio needs to be considered under all circumstances. In addition, case-by-case tests are recommended due to the complexity of fly ash properties. Fly ash can also be used as a low cost adsorbent to remove dyes from textile wastewaters. Fly ash can also be used as the raw material to produce complex coagulant containing both PFS and PAS. Although fly ash is not regulated as a hazardous waste, some fly ashes may contain trace amounts of heavy metals which may have adverse impacts on the environment. Therefore, experimental studies and governmental regulatory actions are still needed.

2.6 REFERENCES

[1] Wark, K., Warner, C. F., Davis, W. T., *Air pollution: its origin and control*, 3rd edition **1998**. Addison, Wesley, Longman, United States.

[2] National Air Pollution Control Administration, **1970**.Washington D.C.

[3] Smith, S.J., Conception, E., Andres, R., Lurz, J. **2004**. Pacific Northwest National Laboratory Report.

[4] USEPA, 1997 Compliance Report: Acid Rain Program, EPA-430-R-98-012, USEPA, Office of Air and Radiation, **1998**. Washington D.C.

[5] American Coal Ash Association, **2003.** Fly ash facts for highway engineers.

[6] Mohapatra, R., Rao, J.R., *J. Chemical Technology and Biotechnology* **2001**, 76, 9.

[7] Cheng, J., Zhou, J., Liu, J., Huang Z., Cao X., Zhao X., Cen K., *Progress in Energy and Combustion Science* **1994**, 29(5), 381.

[8] Lyu, J., Gunasekaran, A., Chen, C., Kao, C., C*omputers and Industrial Engineering* **1995**, 28(4), 861.

[9] Cheng, J., Zhou, J., Cao, X., Cen, K., *J. of Coal Science and Engineering* **2000**, 6(1), 57 (in Chinese).

[10] Qiu, J., Zhang, X., Liu, H., Wang, Q., Li, F., Zeng, H., *Combustion Science and Technology* **2002**, 174(3), 51.

[11] Qiu, J., Li, F., Zheng, C., Zhou, H., *Fuel* **1999**, 78(8), 963.

[12] Yin, C., Luo, Z., Ni, M., Cen, K., *Fuel* **1998**, 77(15), 1777.

[13] Yin, C., Zhou, J., Luo, Z., Yao, Q., Cao, X., Tang, L., Wu, X., Cen, K., *J. China Coal Society* **1997**, 22(4), 343 (in Chinese).

[14] Sheng , C., Xu, M., Zhang, J., Xu, Y., *Fuel Process Technology* **2000**, (64), 1.

[15] Sage, P.W., Ford, N.W.J., *Process Institution of Mechanics Engineering A: Journal of Power Energy* **1996**, 210(3), 183.

[16] USEPA, Standards of Performance for New Stationary Sources, **1980**, 8210-8213.

[17] Cheng, J., Cao, X., Song, Y., Liu, J., Fan, H., Zhou, J., Cen, K., *Process of Chinese Society of Electrical Engineering* **2002**, 22(10), 142 (in Chinese).

[18] Cheng, J., Lv, H., Yang, Z., Xue, Q., *Power System Engineering* **1996**, 12(3), 47 (in Chinese).

[19] Holder, R.G., Milner, C.N., Minchener, A.J., *Institution of Chemical Engineers Symposium Series* **1991**, 123, 227.

[20] Zhou, J., Cheng, J., Cao, X., Liu, J., Zhao, X., Huang, Z., Cen, K., *Energy* **2001**, 26 (8), 759.

[21] Cen, K., Cheng, J., Cao, X., Zhou, J., Liu, J., *Power Engineering* **2000**, 20(6), 1 (in Chinese).

[22] Cheng, J., Zhou, J., Liu, J., Fan, H., Cao, X., Li, Z., Cen, K., *Process of Chinese Society of Electrical Engineering* **2002**, 22(9), 128 (in Chinese).

[23] Liu, J., Zhou, J., Cheng, J., Cao, X., Zhao, X., Cen, K., *Process of Chinese Society of Electrical Engineering* **2003**, 23(2), 153 (in Chinese).

[24] Muzio, L.J., Offen, G.R., *Jof Air Pollution Control Association* **1987**, 37(5), 642.

[25] Ye, Z., Wang, W., Zhong, Q., Bjerle, I., *Fuel* **1995**, 74(5), 743.

[26] Wang, W., Bjerle I., *Chemical Engineering Science* **1998**, 53(11), 1973.

[27] Chang, L., Zhu, S., Ye, J., Xie, K., *Environmental Chemistry* **1998**, 17(6), 532 (in Chinese).

[28] Li, N., Liu, W., Qian, J., *Shanghai Environmental Science* **1998**, 17(12), 21 (in Chinese).

[29] Li, N., Liu, W., Lu, J., Qian, J., *Environmental Protection* **1998**, 4, 43 (in Chinese).

[30] Cai, L., Koziel, J.A., Nguyen, A.T., Liang,Y., Xin. H., *J. Environmental Quality* **2007**, 36(1), 184.

[31] Van Houte, G., *J. Air Pollution Control Association* **1978**, 28 (10), 1030.

[32] Shale, C.C., Simpson, D.G., Lewis, P.S., *Chemical Engineering Progress Symposium* **1978**, 67(115), 52.

[33] Stromberger, M.J., **1984,** The removal of sulfur dioxide from coal-fired boiler flue gas by ammonia injection. M.S thesis, University of Cincinnati, Cincinnati.

[34] Keener, T.C., David, W.T., **1988** Final report to the Ohio coal development office, Columbus, OH.

[35] He, B., Zheng, X., Wen, Y., Tong, H., Chen, M., Chen, C., *Energy Conversion and Management* **2003**, 44(13), 2175.

[36] USEPA, Database of information collected in the electric utility steam generating unit mercury emissions information collection effort, **2001**.

[37] Kaminski, J., *Applied Energy* **2003,** 75(3), 165.

[38] Gutierrez O.F.J., Vidal, F., Ollero, P., Salvador, L., Cortes, V., I*ndustrial and Engineering Chemistry Research* **2006**, 45(4), 1466.

[39] Kikkawa, H., Nakamoto, T., *Industrial and Engineering Chemistry Research* **2002**, 41(12), 3028.

[40] Warych, J., Szymanowski, M., *Chemical Engineering and Technology* **2002**, 25(4), 427.

[41] Rochelle, R.T., King, C.J. *Industrial and Engineering Chemistry Fundamentals* **1977**, 16(1), 67.

[42] Chang, J.C.S., Mobley, J.D., *J. Air Pollution Control Association* **1983**, 33(10), 955.

[43] Liu, S., Xiao, W., *International Journal of Chemical Reactor Engineering* **2006** 4(24), 1.

[44] Raymond, W.J., Sliger, S.J., *Chemical Engineering Progress* **1978**, 74(2), 75.

[45] Rader, P., Botelho, C., **2003,** *Power Gen Latin America*, Sao Paolo, Brazil.

[46] Ollero, P., Futierrez, F.J., Cabanillias, A., Otero, J., *Industrial and Engineering Chemistry Research* **2001**, 40(23), 5640.

[47] Chang, M., Balbach, J.H., Rood, M.J., Kushner, M.J., *J. Applied Physics* **1991**, 69(8), 4409.

[48] Dong, L., Wu, Z., Yang, J., Chi, X., **2003**, Annual Report Conference on Electrical Insulation and Dielectric Phenomena, Albuquerque. Albuquerque, New. Mexico, U.S.A.

[49] Sun, W., Pashaie, B., Dhali, S., Honea, F.I., *J. Applied Physics* **1995**, 79(7), 3438.

[50] Onda, K., Kasuga, Y., Kato, K., Fujiwara, M., Tanimoto, M., *Energy Conversion and Management* **1997**, 38(10), 137.

[51] Stankowski, S., Murkowski, A., Malinowski, R., *Folia Universitatis Agriculturae Stetinensis* **1998**, 190, 277.

[52] Satrio, J.A.B., Jagtap, S.B., Wheelock, T.D., *Industrial and Engineering Chemistry Research* **2002**, 41(15), 3540.

[53] Shi, Y., Fan, M., Li, N., Brown, R.C., Sung, S., *Biochemical Engineering Journal* **2005,** 22(3), 207.

[54] Shi, Y., Fan, M., Xu, M., Brown, R.C., van Leeuwen, J.(H)., *Biochemical Engineering Journal* **2005**, 24(2), 157.

[55] Fan, M., Brown, R.C., Sung, S., Zhuang, Y., **2000**, *Proceedings - Annual International Pittsburgh Coal Conference 17th*, Pittsburgh, PA, U.S.A.

[56] Butler, A.D., Fan, M., Brown, R.C., Cooper, A.T., van Leeuwen, J.(H)., Sung, S., *Chemical Engineering Journal* **2004**, 98(3), 265.

[57] Giere, R., Carleton, L.E., Lumpkin, G.R., *American Mineralogist* **2003**, 88(11-12), 1853.

[58] Daniels, W.L., Stewart, B., Haering, K., Zipper, C., Powell River Project. Virginia Polytechnic Institute and State University, 2002.

[59] Adriano, D.C., Weber, J.T., *Journal of Environment Quality* **2001**, 30, 596.

[60] Hower, J.C., Robertson, J.D., Thomas, G.A., *Fuel* **1995**, 75(4), 403.

[61] Antiohos, S.K., Tsimas, S., *Waste Management* **2007**, 27(5), 675.

[62] Rostami, H., Brendley, W., *Environmental Science and Technology* **2003**, 37 38(15), 3454.

[63] Cai, C., Chu, Q., Wang, Y., *Shanghai Huanjing Kexue* **2006**, 25(2), 51 (In Chinese).

[64] Zhou, C., Wu, M., *Faming Zhuanli Shengqing Gongkai Shuomingshu* **2007**, CN 1002-8713, 20050812 (patent written in Chinese).

[65] Ma, B., Zhang, M., Jian, S., Luo, Z., Bai, J., *Faming Zhuanli Shengqing Gongkai Shuomingshu* **2006**, CN 1001-9476, 20060627 (patent written in Chinese).

[66] Wang, D., Chen, L., *Faming Zhuanli Shengqing Gongkai Shuomingshu* **2006**, CN 1007-7649, 20050622 (patent written in Chinese).

[67] Lin, K., Lin, C., *Zhuoguo Huanjing Gongcheng Xuekan* **2006**, 16(1), 39.

[68] Yoon, S., Yun, Y., *Journal of Material Science* **2006**, 41(13), 4315.

[69] Mohanty, S., Chugh, Y.P., *Tribology International* **2007**, 40(7), 1217.

[70] Kalra, N., Jian, M., Joshi, H.C., *Bioresource Technology* **1998**, 64(3), 163.

[71] Kalra, N., Harit, R.C., Sharma, S.K., *Bioresource Technology* **2000**, 75(1), 91.

[72] Majumdar, K., Singh, N., *Chemosphere* **2007**, 66(4), 630.

[73] Pathan, S.M., Aylmore, L.A.G., Colmer, T.D., *J. Environment Quality* **2003**, 32(2), 687.

[74] Yunusa, I.A.M., Eamus, D., DeSilva, D.L., *Fuel* **2006**, 85(16), 2337.

[75] Rautaray, S.K., Ghosh, B.C., Mittra, B.N., *Bioresource Technology* **2003**, 90(3), 275.

[76] Singh, L.P., Siddiqui, Z.A., *Bioresource Technology* **2003,** 86(1) 73.

[77] Gupta, G.S., Prasad, G., Singh, V.N., *Water Research* **1990**, 24(1), 45.

[78] Mohan, D., Singh, K.P., Singh, G., Kumar, K., *Industrial and Engineering Chemistry Research* **2002**, 41(15), 3688.

[79] Rao, V.V.B., Rao, S.R.M., *Chemical Engineering Journal* **2006**, 116(1), 77.

[80] Chatterjee, D., Ruj, B., Mahata, A., *Catalysis Communications* **2001**, 2(3-4), 113.

[81] Ravikumar, K., Ramalingam. S., Krishnan, S., Balu, K., *Dyes and Pigments* **2006**, 70(1), 18.

[82] Cheung, K.C., Venkitachalam, T.H., *Chemosphere* **2000**, 41(1-2), 243.

[83] Moreno, N., Querol, X., Ayora, C., *Environmental Science and Technology* 2001, 35(17), 3526.

[84] Li, L., Fan, M, Brown, R.C., Koziel, J. A., van Leeuwen, J(Hans)., *J. Hazardous Materials* (submitted)

THE AUTHORS:

Ling Li (PhD, Environmental Engineering, Iowa State University, Ames, IA, USA) has worked on removal of SO_2 from flue gas using fly ash waste from power plants.

Maohong Fan (PhD, Materials Science and Engineering, Georgia Institute of Technology, Atlanta, GA, USA) is a senior research scientist. His research areas include identification and removal of conventional and emerging contaminants in water and wastewater, and pollutants in air.

Robert C. Brown (PhD, Professor, Mechanical Engineering, Chemical and Biological Engineering, Agricultural and Biosystems Engineering, Agricultural and Biosystems Engineering, Ames, IA, USA) is the founding director of the Bioeconomy Institute (BEI) at ISU, a university-wide initiative that coordinates research, educational, and outreach activities related to biobased products and bioenergy.

Jacek A. Koziel (PhD, Associate Professor, Agricultural and Biosystems Engineering, Ames, IA, USA) has worked on air quality and livestock odor measurements, novel methods for odor characterization and control, biotechnology and purification of fuel ethanol.

J(Hans) van Leeuwen (PhD, Professor, Civil and Environmental Engineering, Agricultural and Biosystems Engineering) researches ethanol production and purification. He also studies physical-chemical treatment of water and wastewater, and air pollution control. He also researches purification of ethanol with ozonation and activated carbon to make food-grade alcohol.

Contact:
J(Hans) van Leeuwen
376 Town Engineering
Iowa State University
Ames, IA   50011
Phone: 515-294-5251
Email: leeuwen@iastate.edu

CHAPTER 3 PRODUCTION OF A NEW WASTEWATER TREATMENT COAGULANT FROM FLY ASH WITH CONCOMITANT FLUE GAS SCRUBBING

A paper submitted to the Journal of Hazardous Materials

Ling Li[a], Maohong Fan[b], Robert C. Brown[c], Jacek A. Koziel[d], J(Hans) van Leeuwen*[a,,d]

[a] Department of Civil and Environmental Engineering, Iowa State University, Ames, IA, 50011

[b] School of Materials Science and Engineering, Georgia Institute of Technology, Atlanta, GA, 30332

[c] Center for Sustainable Environmental Technologies, Iowa State University, Ames, IA, 50011

[d] Department of Agricultural and Biosystems Engineering, Iowa State University, Ames, IA, 50011

* Corresponding author. Tel.:+1-515-294-5251, Fax: +1-515-294-8216, Email: leeuwen@iastate.edu

3.1 ABSTRACT

The research focused on the production of a complex wastewater coagulant containing polymeric sulfates of aluminum and iron from fly ash. At the same time, SO_2 in the simulated flu gas was removed by absorption in a fly ash slurry and oxidized with sodium chlorate. Extraction efficiency of iron and aluminum oxides from fly ash was affected greatly by reaction temperature and time. The extraction efficiency increases as temperature increases. Removal efficiency of SO_2 was influenced by temperature, SO_2 feed concentration and feed gas dispersing method. The produced complex coagulant containing both polymeric ferric sulfate (PFS) and polymeric aluminum sulfate (PAS) was proven to be effective in removing total

suspended solids (TSS) and turbidity in wastewater. The complex coagulant is more effective than conventional iron and aluminum sulfates in turbidity removal.

Key words: Fly ash; SO_2 removal; Coagulant; Wastewater treatment

3.2 INTRODUCTION

Coal remains the most important source of energy in most countries. Coal from most sources contains appreciable fractions of sulfur, which is oxidized and released as sulfur dioxide mainly during combustion. Although the total emission of SO_2 to atmosphere has been reduced over the past 30 years, it still amounted to over 60 million metric tons in 2000 worldwide [1]. Overall, about 80% of the SO_2 released to the atmosphere is from coal combustion [1, 2]. Sulfur dioxide is a severe lung irritant, and the main source of acid rain, which causes acidification of water bodies and soils, damages plants, corrodes metals, and increases secondary fine particulate matter in the air [2, 3]. Traditional flue gas desulfurization processes involve calcium sorbents, either dry or wet. Although some of these methods can achieve more than 90% SO_2 removal from the flue gas [2, 4, 5], their byproducts are either of low market value or produce waste, requiring separation and/or dewatering, and disposal, typically by landfilling. However, SO_2 could be used as an important raw material in industry.

New technologies based on recovering SO_2 from flue gas have been investigated. Pulsed corona and dielectric barrier discharges are effective desulfurization technologies aimed at oxidizing SO_2 with the production of SO_3 or H_2SO_4 [6-8]. In recent studies in our research group, SO_2 has also been used in the recovery of acetic

acid and lactic acid from calcium acetate and calcium lactate solutions [9, 10], and as a raw material in the production of polymeric ferric sulfate (PFS), an effective water treatment coagulant [11, 12].

Fly ash is a fine particulate material that is produced by the combustion of pulverized coal and carried out by flue gas. The physical and chemical properties of fly ash depend on the coal source, additives used in the combustion or post-combustion processes, and the pollution control technologies [13]. Normally, fly ash particles are spherical and exhibit smooth surface texture [13] and the size of fly ash particles is in the range of 0.01 to 0.1 mm [14]. Oxides of Fe, Al, and Si are the major elements in fly ash while other minor compounds, like Ca, Mg, Na, K, are also present. The typical concentrations of Si, Al, Fe, Ca, Mg, Na and K oxides in bituminous coals of the United States, are in the ranges of 20-60%, 5-35%, 10-40%, 1-12%, 0-5%, 0-4%, and 0-3%, respectively [13].

Combustion of coal in the United States alone produced approximately 68 million tons of fly ash in 2001, of which only about 30% was used, the rest was disposed of in landfills [13]. Transportation and disposal of fly ash will increase the amount of particulate materials in the air during windy conditions. Landfilling is not an optimal solution to fly ash disposal for this and other reasons. The major application of fly ash is in the concrete industry [13]. The addition of high calcium fly ash into Portland cement can improve some of the cementitious properties, such as ultimate strength, durability, chemical resistance and reduced permeability [13, 15]. Varieties of new technologies have been developed for manufacturing fly-ash based cements [16, 17].

Fly ash has been used to improve the physical and chemical properties of coarse or sandy soils [18, 19]. Since fly ash is composed mostly of silt-sized particles, it can be used to improve the properties of coarse-textured or sandy soils and increase the soil moisture holding capacity, which is helpful in increasing plant growth [20-24]. For the same reasons, fly ash can also be used to stabilize soils at beef cattle feedlots [25]. Considering fly ash also contains smaller amounts of P, N, K, Na, and Mg, some studies have investigated the possibility of fly ash as a fertilizer supplement [20, 22, 26, 27]. Fly ash has also been used as a low-cost adsorbent in industrial wastewater treatment, such as dyes [28-33], improved phosphorus removal [34], and purifying acid mine water [35].

Fly ash is rich in aluminum and iron oxides, which are essential raw materials for the production of water and wastewater treatment coagulants. This paper investigates the extraction of iron and aluminum oxides from fly ash to make a polymeric complex coagulant with the oxidation of SO_2. It is aiming at analyzing (a) factors effecting conversion efficiency of iron and aluminum oxides to Fe^{3+} and Al^{3+} ions, (b) investigating SO_2 removal efficiency and (c) evaluating the produced the capability of complex coagulant in wastewater treatment.

3.3 MATERIALS AND METHODS

3.3.1 CHARACTERISTICS OF FLY ASH

The particle size and other physical properties of the fly ash sample were analyzed by a Hitachi -2460N scanning electron microscope (SEM) at the Material Analysis

and Research Laboratory at Iowa State University. The chemical properties of the fly ash were provided by the manufacturer, HeadWaters Resource. The fly ash sample was analyzed by SEM as received.

3.3.2 EXPERIMENTAL ASPECTS

3.3.2.1 APPARATUS
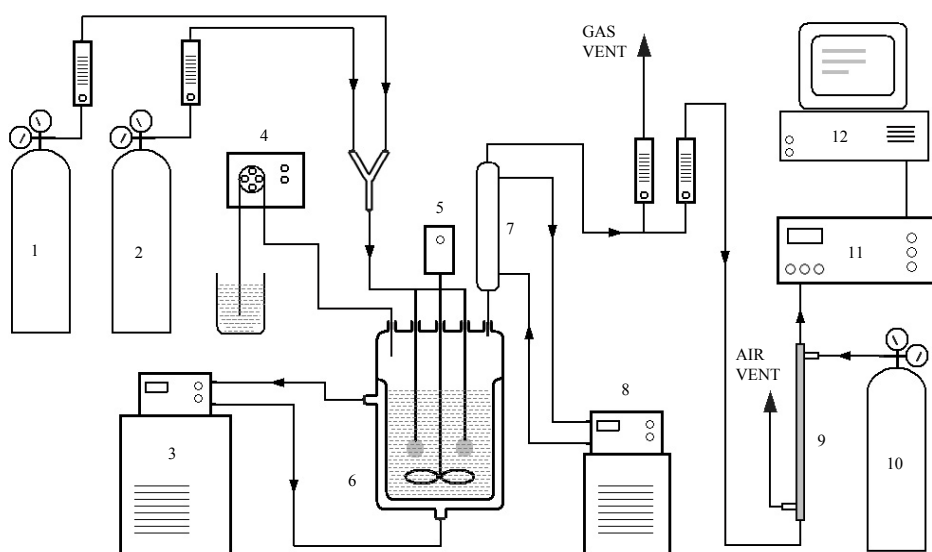
1. Nitrogen tank   2. SO$_2$ mixture tank   3. Reactor heater unit   4. Oxidizer pump
5. Stirrer motor   6. Jacketed reactor   7. Condenser   8. Condenser chiller unit
9. Sample gas dryer   10. Air tank   11. Gas analyzer   12. Data acquisition computer

Fig.3. 1 Laboratory flue gas scrubber for the simultaneous synthesis of a complex coagulant from fly ash and flue gas

A schematic diagram of the reaction system is shown in Fig. 3.1. The reaction was conducted in a 500 ml jacketed glass reactor (ChemGlass Inc., Vineland, NJ, USA) with a polytetrafluoroethylene (Teflon) propeller connected to the center inlet, stirring at 200 rpm. Fly ash slurry was introduced into the reactor through a funnel, which was connected to the second inlet on the reactor lid. The funnel was then removed and the

inlet was sealed by a stopper. A pump was connected to this inlet to dose oxidizer as needed periodically. A thermometer for monitoring the reaction temperature was connected to the third inlet. The flue gas was simulated by a N_2-SO_2 mixture, which passed through the fourth inlet on the lid into the reaction tank. The outlet gas stream passed through a condenser, connected to the fifth inlet. The condenser was used to chill the outlet gas stream and return the condensate back to the reactor. The gas stream entered a ZRF NDIR gas analyzer (Fuji Electric Co., Tokyo, Japan). A Dow Corning Fluid (Dow Chemical Co., Midland, MI, USA) was circulated through the reactor jacket by using a Neslab RTE 111heater unit.

3.3.2.2 OPERATION PROCEDURES

Each bath used 100 ml water and 100 g fly ash with Fe_2O_3 content of 25.48% and Al_2O_3 content of 21.03%. Stoichiometric quantities of SO_2, sulfuric acid and sodium chlorate were calculated. To eliminate the interference of soluble alkaline salts in the reaction, the fly ash was pretreated by adding hot water to remove trace amounts of Na_2O, K_2O, MgO and CaO [36]. The fly ash slurry was heated for about 30 min, and then settled for 1 hour and filtered. The insoluble fly ash particles were then dried at 110 °C for 2 hours. Then the fly ash slurry was added into the reactor and was stirred at 200 rpm at room temperature for 1 hour to make a homogeneous distribution. When the temperature reached the desired value, 50 ml 96% H_2SO_4 was introduced into the system through a funnel and the simulated flue gas was bubbled through the stirred fly ash slurry at the same time. SO_2 at 4% was mixed with N_2 to simulate flue gas. The final concentration of SO_2 was controlled at 4000 ppm and 2000 ppm, which is at the

high end of sulfur dioxide concentration in flue gas [37]. Sodium chlorate was added into the reaction system after the simulated flue gas was introduced, resulting in the oxidation of SO_2. This experiment was run at seven different temperatures: 70, 80, 90, 100, 110, 120, and 130 °C. The reaction for each run was conducted for 6 hours. The mixture was sampled with a 1 ml pipette at 30 min intervals to monitor the change of Fe^{3+} and Al^{3+} ions and to develop the reaction kinetics.

The reactions are described as follows. Fe_2O_3 and Al_2O_3 in fly ash react quickly with the added H_2SO_4 to produce Fe^{3+} and Al^{3+} (reaction 1 and 2).

$$Fe_2O_3 + 6H^+ \Rightarrow 3H_2O + 2Fe^{3+} \tag{1}$$

$$Al_2O_3 + 6H^+ \Rightarrow 3H_2O + 2Al^{3+} \tag{2}$$

At the same time, $NaClO_3$ oxidizes SO_2, resulting in additional SO_4^{2-} and H^+,

$$NaClO_3 + 3H_2O + 3SO_2 \Rightarrow 3SO_4^{2-} + 6H^+ + Na^- + Cl^- \tag{3}$$
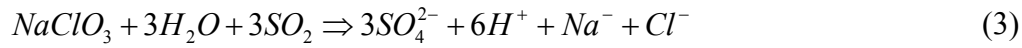
Hydrolysis (4, 5 and 6) follows with hydroxides from water dissociation,

$$H_2O \Leftrightarrow H^+ + OH^- \tag{4}$$

$$2Fe^{3+} + \frac{6-n}{2}(SO_4^{2-}) + n(OH^-) \Rightarrow [Fe_2(OH)_n(SO_4)_{\frac{6-n}{2}}] \tag{5}$$

$$2Al^{3+} + \frac{6-m}{2}(SO_4^{2-}) + m(OH^-) \Rightarrow [Al_2(OH)_m(SO_4)_{\frac{6-m}{2}}] \tag{6}$$
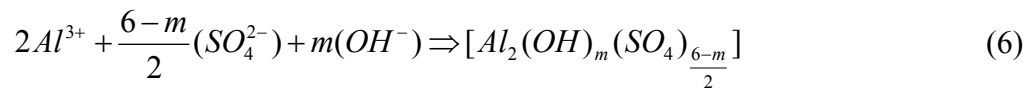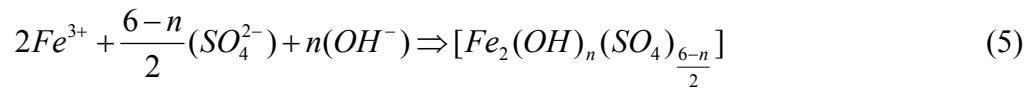
Polymerization (7 and 8) will proceed under certain conditions to form polymeric ferric sulfate (PFS) and polymeric aluminum sulfate (PAS), two components of the complex polymer [12].

$$p[Fe_2(OH)_n(SO_4)_{\frac{6-n}{2}}] \Rightarrow [Fe_2(OH)_n(SO_4)_{\frac{6-n}{2}}]_p \tag{7}$$

$$q[Al_2(OH)_n(SO_4)_{\frac{6-m}{2}}] \Rightarrow [Al_2(OH)_m(SO_4)_{\frac{6-m}{2}}]_q \tag{8}$$
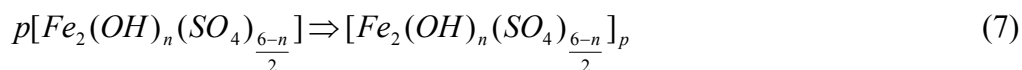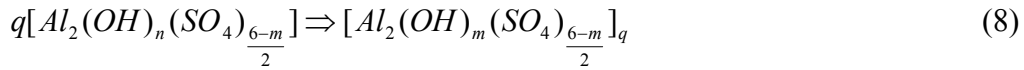
3.3.2.3 ANALYSIS OF SO$_2$ IN THE GAS STREAM FROM THE REACTOR

The concentration of SO$_2$ in the gas stream was analyzed with a ZRF NDIR gas analyzer. The reading range of the gas analyzer is 0-10% SO$_2$ concentration by volume [12]. Before each run, the instrument was calibrated with a 0.5% SO$_2$ gas. The concentration of SO$_2$ in the inlet gas stream was controlled at 2000 ppm or 4000 ppm with N$_2$ and SO$_2$ using flow meters (Fig. 3.1).

3.3.2.4 ANALYSIS OF AL^{3+} IN THE PRODUCED COAGULANT

The Al^{3+} concentrations in the produced coagulant were analyzed with an Agilent 4500 ICP-MS. The samples were diluted 100,000-200,000 times prior to ICP-MS analysis. The instrument was calibrated with standard solutions at 10, 20, 50, 100, 150 and 200 ppb prior to each analysis. An instrument blank was run before each sample set.

3.3.2.5 ANALYSIS OF FE^{3+} AND FE^{2+} IN THE PRODUCED COAGULANT

The analysis of total iron in the produced coagulant was completed with a HACH 3000 spectrophotometer. The samples were diluted 1,000-2,000 times prior to analysis. Hydroxylamine hydrochloride was added into the diluted samples to reduce ferric iron to ferrous iron, which reacts with orthophenanthroline to form an orange-red Fe(II)-orthophenanthroline complex. The reaction is described by Equation 9.

$$Fe^{2+} + 3PhH^+ \leftrightarrow Fe(Ph)_3^{2+} + 3H^+ \tag{9}$$
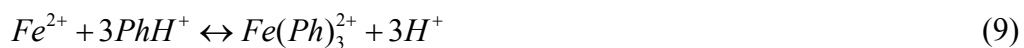
The instrument was calibrated with standard Fe (II) - orthophenanthroline complex solutions at 1, 2, 5, 8, 10, 20 ppm prior to each analysis. An instrument blank was run before each sample set. All the samples were run at 510 nm wavelength.

A potassium permanganate titration method is used to determine ferrous iron concentration in the final product. The method is based on the following reaction:

$$MnO_4^+ + 5Fe^{2+} + 8H^+ = Mn^{2+} + 5Fe^{3+} + 4H_2O \tag{10}$$
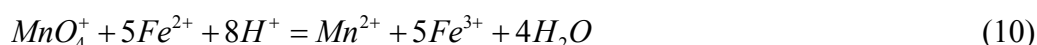
The ferrous iron concentration can be expressed as below:

$$X_2 = \frac{(V-V_0) \times C \times 0.5585}{m} \times 100 \times 5 \tag{11}$$

where V(ml) is the volume of potassium permanganate consumed at the end point, V_0 (ml) is the volume of potassium permanganate consumed by distilled water at the end point, C is the concentration (M) of the standard potassium permanganate solution, m is the mass (g) of sample and 0.5585 is the mass of 0.001 mol iron.

3.3.2.6 PERFORMANCE OF THE PRODUCED COAGULANT COMPLEX

The complex coagulant produced at 130°C was used to test the removal capabilities of total suspended solid (TSS) in wastewater from ethanol fermentation and turbidity removal from a kaolinite suspension (Wilkinson Kaolin Assoc. Ltd.). The performance of the produced coagulant was tested using a Philips & Bird Model FB 700 six-jar tester. The turbidity was measured with a Cole Parmer Model 8391-40 turbidity meter.

For the TSS removal, 1000 ml of the wastewater was filled in the jar tester and stirred at 130 rpm for 10 min, in order to maintain a homogeneous TSS distribution.

The coagulant sample was weighed carefully to make 50, 100, 150, 200, 250, and 300 ppm total concentration of $Fe^{3+} + Al^{3+}$ in the wastewater sample. After the coagulant was added, the wastewater was stirred at 30 rpm for 10 min and then at 5 rpm for 10 min. The pH in the test was adjusted to 5, 6, and 7 by adding H_2SO_4 and NaOH solutions.

For the turbidity removal, kaolinite was added to 1000 ml tap water and stirred at 130 rpm for 10 min. The coagulant sample was weighed carefully to make 1, 5, 10, 20, 30, and 50 ppm total concentration of $Fe^{3+} + Al^{3+}$ in the wastewater sample. After the coagulant was added, the wastewater was stirred at 30 rpm for 10 min and then at 5 rpm for 10 min. The pH in the test was adjusted in the range of 5.5 to 9.5 by adding H_2SO_4 and NaOH solutions. The original turbidity of each water sample was 92.7 NTU.

3.4 RESULTS AND DISCUSSION

3.4.1 CHARACTERISTICS OF FLY ASH

The fly ash sample with the highest Fe_2O_3 and Al_2O_3 contents and the lowest concentrations of alkali oxides was chosen from samples from three difference sources as provided by Headwaters Resources Inc. The chemical properties of the fly ash as tested with the American Society for Testing and Materials (ASTM) standard method D4326, X-ray fluorescence (XRF) techniques by the fly ash supplier are listed in Table 3.1.

Table 3. 1Composition of fly ash

Elements as oxides	SiO_2	Al_2O_3	Fe_2O_3	CaO	Na_2O	SO_3
wt%	43.65	21.03	25.48	2.58	1.25	1.03
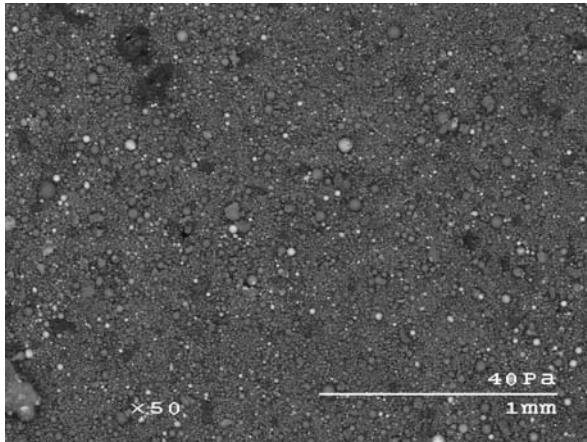
Fig.3. 2 SEM micrograph of fly ash sample, x50
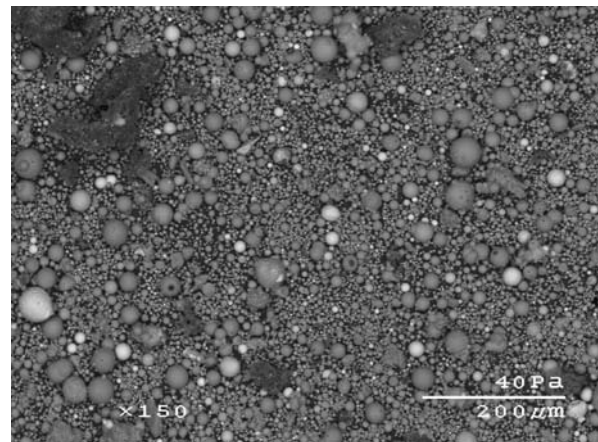
Fig.3. 3 SEM micrograph of fly ash sample, x150
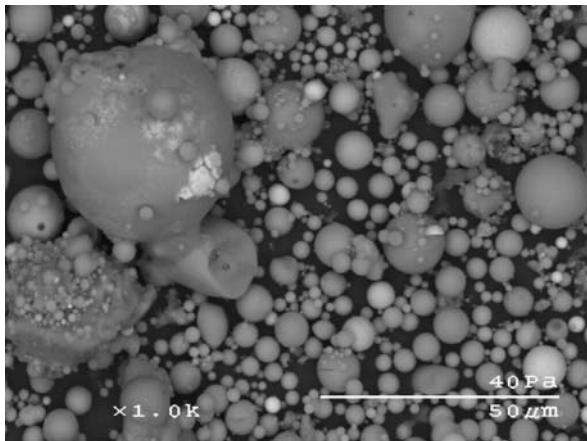
Fig.3. 4 SEM micrograph of fly ash sample, x1000
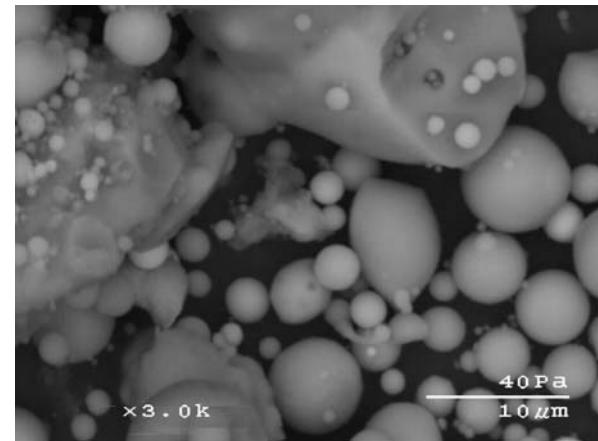
Fig.3. 5 SEM micrograph of fly ash sample, x3000

Micrographs of fly ash at different magnifications are shown in Fig. 3.2-Fig. 3.5. The figures show that the particles in fly ash are smooth, spherical and glassy, and some of the aluminum oxides are combined together with silicon oxides. The dark spots were identified as iron oxides by the SEM. The light spots were identified as mullite, which has a crystalline structure derived from aluminosilicate minerals [38-40]. Research on fly ash structures demonstrated that the aluminosilicate particles have complex structures and the silicate and aluminum compounds are fused together [38, 40].

3.4.2 CHARACTERISTICS OF THE PRODUCED COAGULANT

The color of the produced complex coagulant containing both PFS and PAS varied from light greenish yellow to dark brown at different temperatures. A quality standard for the produced coagulant was developed based on previous work [12, 41]. The indices are listed in Table 3.2.

Table 3. 2 Quality indices of the produced complex coagulant

Index	pH (1 % sln)	$(Fe^{3+} + Al^{3+})$(%)	Fe^{2+} (%)	density (g/cm^3)	basicity (%)
Desired value	2.0-3.0	≥ 5.0	≤ 0.1	≥ 1.23	≥ 10.0
Tested value*	2.13	5.26	0	1.45	10.8

*: data from coagulant produced at 130°C.

It is important to maintain the 1% solution pH in complex coagulant because a suitable pH will help to assure the stability of the product. If the pH is too high, the stability will decrease with the tendency of precipitation [12]. The pH was measured with a Corning pH meter 320. Density was measured with a 10 ml Gay-Lussac density bottle.

Another important standard for the produced complex coagulant is basicity, which was calculated by Eq. (12).

$$Basicity = \frac{(V_0 - V) \cdot c \times (18.62 \times X_{Fe^{3+}} + 8.99 \times X_{Al^{3+}})/1000}{m \cdot (X_{Fe^{3+}} + X_{Al^{3+}})} \times 100 \tag{12}$$

where V_0 is the volume (ml) of consumed sodium hydroxide standard titrant by the blank (distilled water) sample at the stoichiometric point; V is the volume (ml) of sodium hydroxide standard titrant consumed by the complex coagulant sample at the stoichiometric point; c is the concentration (M) of the standardized sodium hydroxide solution; m is the mass (g) of the complex coagulant sample; and $X_{Fe^{3+}}$ and $X_{Al^{3+}}$ are

the mass concentrations of Fe^{3+} and Al^{3+} in the complex coagulant sample; 18.62 is

the mass of 1/3 mol iron and 8.99 is 1/3 mol aluminum. The basicity is the mass ratio

of OH^- to Fe^{3+} and Al^{3+} in the complex coagulant by definition. It is also a

measurement of the degree of the hydrolyzation of the complex coagulant [12, 41].

3.4.3 EFFECTS OF TIME AND TEMPERATURE ON THE PRODUCTION OF THE COAGULANT

The concentrations of Fe^{3+} and Al^{3+} in the prepared complex coagulant are listed in

Tables 3.3 and 3.4. The conversion efficiency is defined as the ratio of the mass of

Fe^{3+} or Al^{3+} in the product to the mass of iron or aluminum in the fly ash. The

conversion efficiency of Fe^{3+} and Al^{3+} are indicated in Fig. 3.6 and 3.7.

Tables 3.3 and 3.4 show that the concentrations of Fe^{3+} and Al^{3+} in the prepared

complex coagulant increase when either reaction temperature or time increases. A

similar trend is shown in Fig. 3.4 and 3.5 for the conversion efficiency. The effect of

reaction temperature on the conversion of iron and aluminum oxides in a specific time

is in agreement with reaction rate theory, which holds that the rate of a chemical

reaction increases with temperature. Furthermore, temperature has different effects on

Fe^{3+} and Al^{3+} conversion. Table 3.3 and Fig. 3.6 indicate that after 360 min of

reaction at 130 °C, the concentration of Fe^{3+} in the complex coagulant solution is

3.38% and Fe^{3+} conversion efficiency is 73%. Fe^{3+} conversion efficiency increases

significantly when the temperature is higher than 100 °C, but there is no obvious

increase at lower temperatures. For Al^{3+}, after 360 min of reaction at 130 °C, the

concentration in solution is 1.88% and conversion efficiency is 37.48%. Al^{3+}

conversion efficiency is increased from 15.76% to 21.77% when the temperature

increases from 70 ℃ to 80 ℃. Then the conversion efficiency increases gradually

until the temperature reaches 120 ℃. The fused structure of aluminosilicate is part of

the reason of relatively lower conversion efficiency of Al_2O_3.

Table 3. 3 Concentrations of Fe^{3+}(wt)% in the complex coagulant produced under different conditions

time, min	70 ℃	80 ℃	90 ℃	100 ℃	110 ℃	120 ℃	130 ℃
0	0.0000	0.0000	0.0000	0.0000	0.0000	0.0000	0.0000
30	0.2516	0.2535	0.3586	0.5127	0.7112	0.6505	0.9081
60	0.2815	0.3106	0.5036	0.6070	0.8451	0.9083	1.1794
90	0.3263	0.3780	0.6086	0.7657	1.0882	1.2554	1.3731
120	0.4010	0.4299	0.6636	0.8451	1.1923	1.5231	1.7121
150	0.4508	0.4973	0.7786	1.0088	1.3561	1.5975	1.9059
180	0.5304	0.5700	0.8936	1.1378	1.5297	1.8503	2.1868
210	0.5703	0.6374	1.0136	1.2072	1.7579	2.0784	2.5065
240	0.6499	0.6945	1.1286	1.3561	1.9513	2.2420	2.6712
270	0.7196	0.7878	1.2436	1.4404	2.1101	2.5246	2.8359
300	0.8790	0.9331	1.2686	1.5644	2.1746	2.6237	3.0102
330	0.9238	0.9694	1.3836	1.7479	2.3680	2.8617	3.2137
360	0.9686	1.0472	1.5886	1.9166	2.6508	3.1294	3.3783

Table 3. 4 Concentrations of Al^{3+}(wt)% in the complex coagulant produced under different conditions

time, min	70 °C	80 °C	90 °C	100 °C	110 °C	120 °C	130 °C
0	0.0000	0.0000	0.0000	0.0000	0.0000	0.0000	0.0000
30	0.2764	0.3362	0.3965	0.4886	0.5127	0.6883	0.6125
60	0.3267	0.3984	0.5118	0.5535	0.5784	0.7673	0.7027
90	0.3494	0.4539	0.6129	0.6315	0.6454	0.9610	0.8660
120	0.4257	0.4747	0.6786	0.7379	0.6931	1.0682	1.0066
150	0.4565	0.6002	0.6995	0.7725	0.7796	1.1806	1.0947
180	0.4944	0.6433	0.7909	0.8624	0.8684	1.2850	1.1897
210	0.5668	0.7156	0.8870	0.9176	0.9917	1.4029	1.2262
240	0.6086	0.7706	0.9358	0.9729	1.0555	1.4851	1.3745
270	0.6642	0.8296	0.9722	1.0390	1.1558	1.5651	1.5180
300	0.6820	0.9163	1.0540	1.1275	1.1827	1.6597	1.6094
330	0.7129	1.0356	1.1362	1.1871	1.3378	1.7029	1.7710
360	0.7905	1.0919	1.2574	1.3793	1.4703	1.8202	1.8798
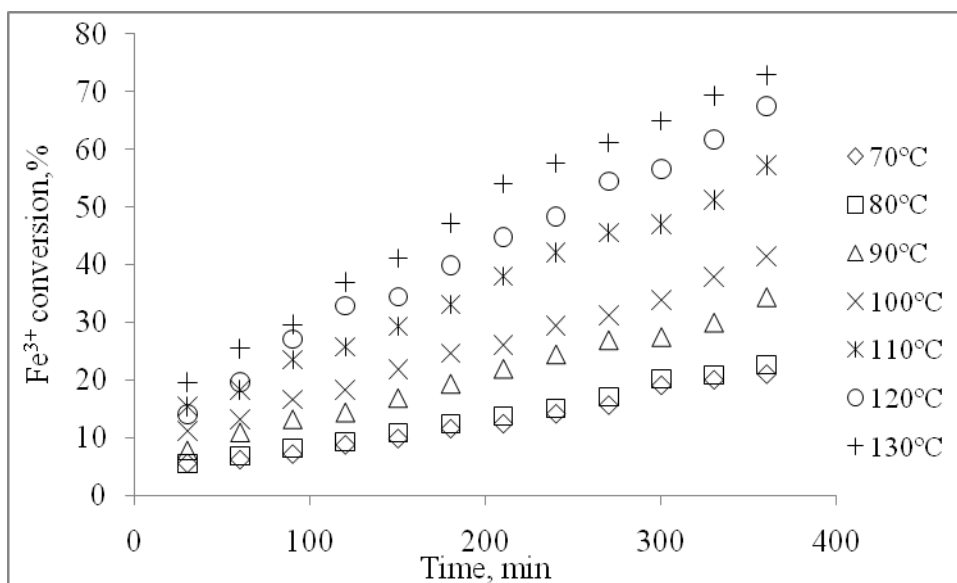
Fig.3. 6 Effect of reaction temperature and time on the conversion efficiency of Fe^{3+}
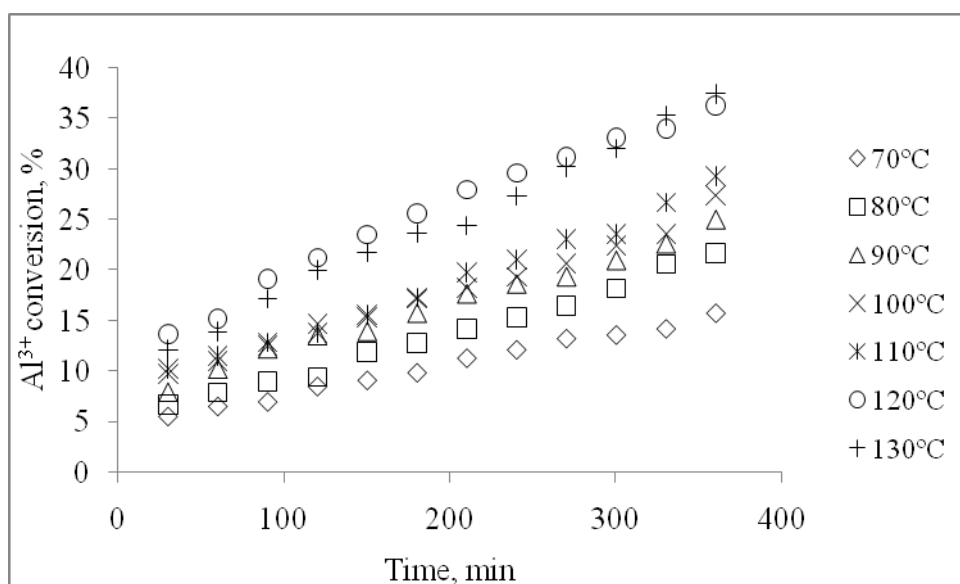
Fig.3. 7 Effect of reaction temperature and time on the conversion efficiency of Al^{3+}

The concentrations of Fe^{2+} in the prepared complex coagulant are listed in Table

3.5, which indicates that there is no Fe^{2+} in the products under each reaction

condition.

Table 3. 5 Concentrations of Fe^{2+}(wt)% in the complex coagulant produced under different conditions

time, min	70 °C	80 °C	90 °C	100 °C	110 °C	120 °C	130 °C
0	0	0	0	0	0	0	0
30	0	0	0	0	0	0	0
60	0	0	0	0	0	0	0
90	0	0	0	0	0	0	0
120	0	0	0	0	0	0	0
150	0	0	0	0	0	0	0
180	0	0	0	0	0	0	0
210	0	0	0	0	0	0	0
240	0	0	0	0	0	0	0
270	0	0	0	0	0	0	0
300	0	0	0	0	0	0	0
330	0	0	0	0	0	0	0
360	0	0	0	0	0	0	0

3.4.4 REMOVAL OF SO_2

As shown in Fig. 3.8 and 3.9, as the temperature increases, the SO_2 removal efficiency decreases. This result indicates that SO_2 removal is not favored by higher temperatures, although high temperature can increase conversion efficiency of Fe_2O_3 and Al_2O_3. Two dispersing methods were used in the removal of SO_2. One method used a bubbling tube immersed into the liquid at the bottom of the reaction tank, and the other attached a porous diffuser to the end of the tubing. Fig. 3.8 and 3.9 indicate that at low temperatures, the two dispersing methods make no significant difference in SO_2 removal efficiency, which is greater than 90% under either condition. However, at higher temperatures, the use of diffuser results in higher removal efficiency as shown in Fig. 3.8 and 3.9. For example, in the system with a SO_2 diffuser, the removal efficiency increased from 65% to 78% at 130 °C after 360 min. Further

investigation on reaction kinetics indicated that the reaction of SO_2 with ClO_3^- is mass transfer controlled. The mass transfer resistance for the gas phase could be reduced significantly due to the use of a diffuser. This indicates that a diffuser increases the overall mass transfer coefficient, thus the removal efficiency of SO_2 can be improved. .Experimental results also show that when other conditions are the same, lower initial concentration of SO_2 also helps in increasing removal efficiency, as shown in Fig. 3.10.
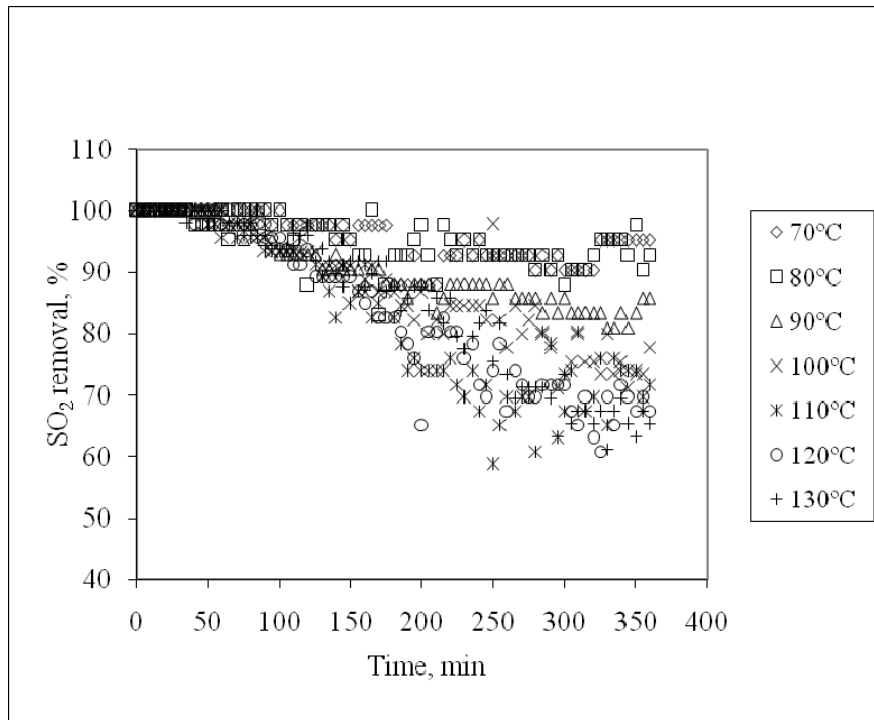
Fig.3. 8 Removal efficiency of SO_2 with feed concentration of 4000 ppm and bubbling dispersing method
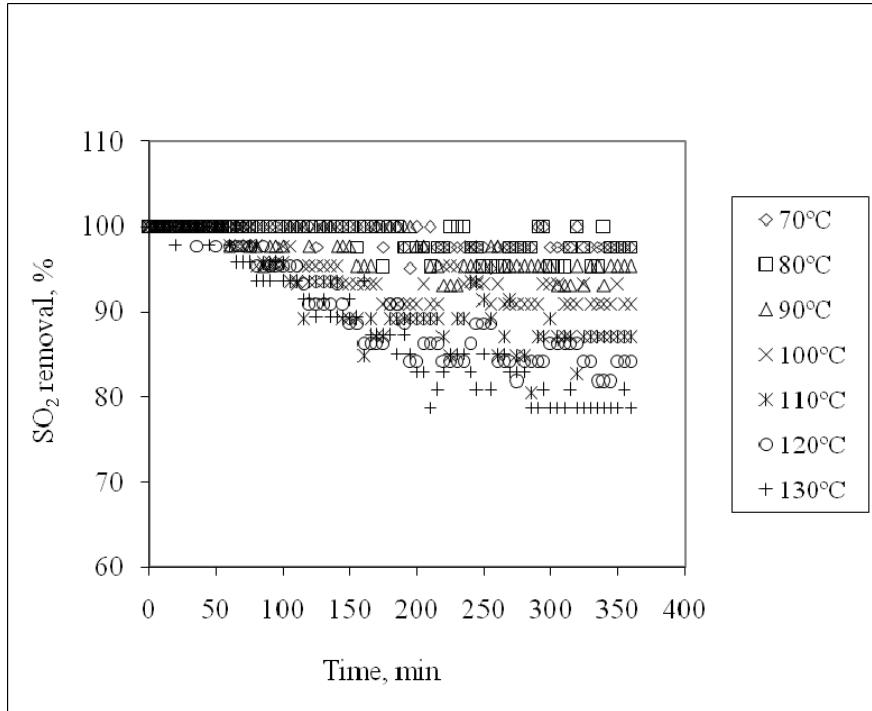
Fig.3. 9 Removal efficiency of SO$_2$ with feed concentration of 4000 ppm and diffuser dispersing method
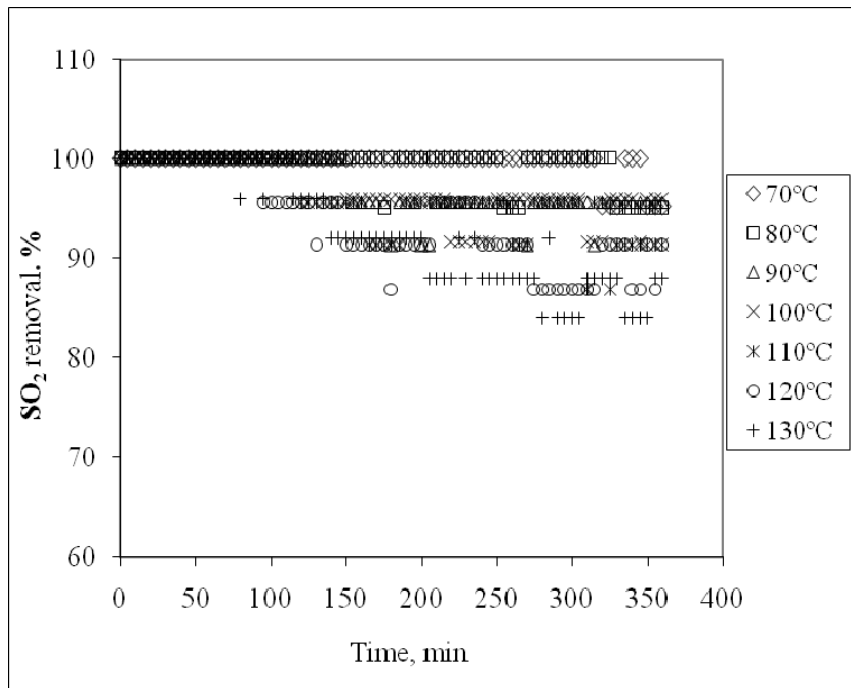
Fig.3. 10 Removal efficiency of SO$_2$ with feed concentration of 2000 ppm and diffuser dispersing method

3.4.4 PERFORMANCES OF THE PRODUCED COAGULANT

The performance of the produced coagulant was tested in a jar-tester system. The effects of pH and coagulant dosages on TSS and turbidity removal were investigated.

3.4.4.1 TOTAL SUSPENDED SOLID REMOVAL

The wastewater used in TSS removal testing was from ethanol fermentation in our research group, containing particles with densities very close to that of water. After 1 week storage in the refrigerator without the addition of the coagulant, no settlement was observed. When the complex coagulant was added in association with stirring to flocculate, a TSS removal of at least 78% was achieved. The results are presented in Table 3.6, which shows that at neutral pH levels, 150-200 ppm will be the optimal dosing range for the maximum TSS removal. Lower or higher coagulant dosages lead to lower TSS removal. The original TSS in the feed was 11 g/L. At the same dosage, the TSS removal was favored by a higher pH value. At pH 5, the TSS removal is only 78.28% at a coagulant dosage of 50 ppm. However, the TSS removal can be higher than 99% at pH 7 at the same dosage.

Table 3. 6 TSS removal by the produced complex at different pH

Coagulant dosage, ppm	Total suspended solid removal, %		
	pH=5	pH=6	pH=7
50	78.28	98.74	99.13
100	92.89	99.01	99.19
150	95.54	99.17	99.15
200	95.54	99.35	99.48
250	91.46	99.18	99.07
300	90.40	98.50	99.17

3.4.4.2 TURBIDITY REMOVAL

Kaolinite (0.4g) was added into 1 L tap water to make an original turbidity of 92.7NTU. The NTU of the water was measured with a turbidity meter after standing for 20 min. Turbidity removal at different coagulant dosages and pH values were analyzed. The performance of the complex coagulant at different dosages for turbidity removal at pH 7.15 is presented in Fig. 3.11. This figure shows that an optimal dosage of 10-20 ppm complex coagulant reduced the residual turbidity to 1.21-1.03 NTU with turbidity removal of 98.7-98.9%.
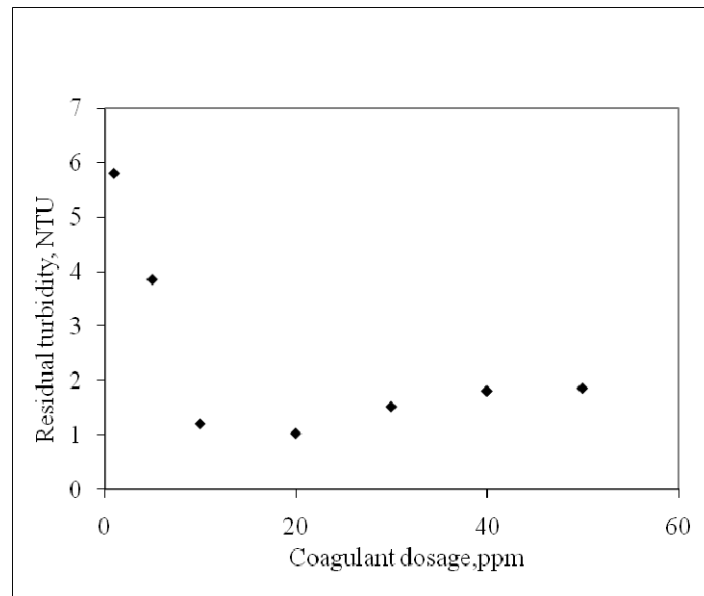
Fig.3. 11 Evaluation of the produced complex coagulant in removing turbidity (pH=7.15)

The effects of pH on the turbidity removal are shown in Fig.3.12. The data from this experiment shows that the optimal pH range for the turbidity removal is 6.5-8.5, with the lowest residual turbidity of 1.27 NTU (98.63% removal). Therefore, the turbidity removal by the produced complex coagulant is in favor of neutral to slight alkaline conditions.
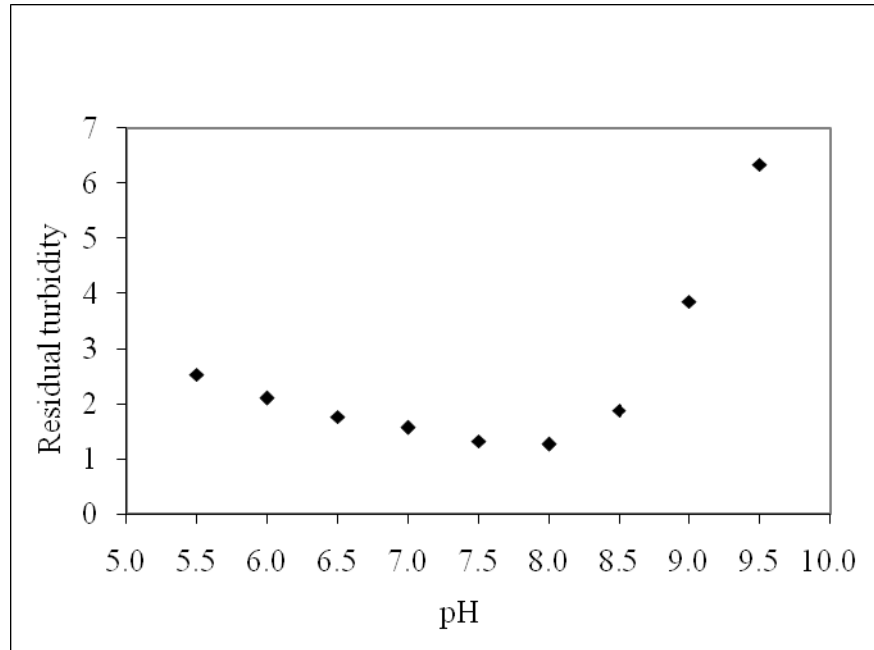
Fig.3. 12 Turbidity removal at different pH (coagulant dosage 10 ppm)
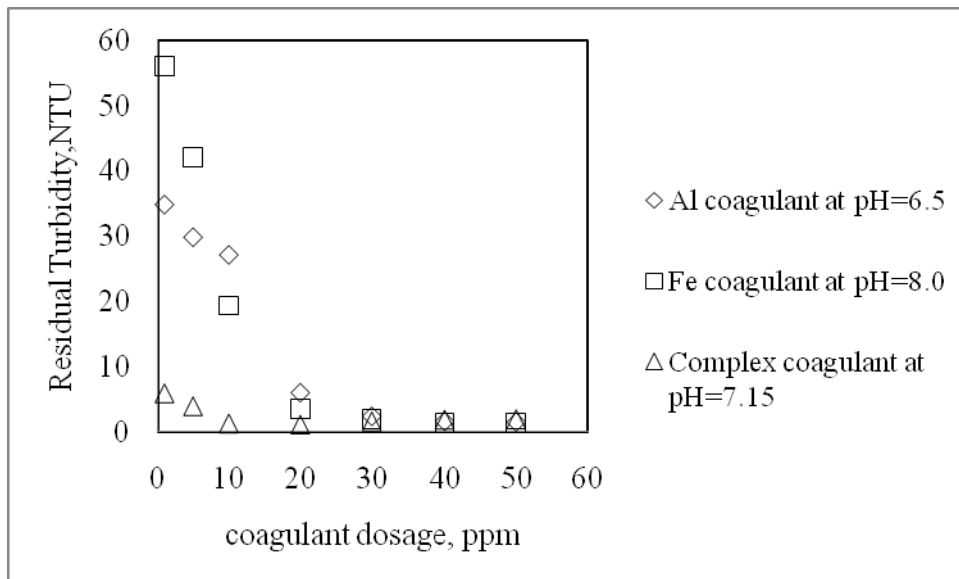
Fig.3. 13 Comparison of turbidity removal of different coagulant (at optimal pH for each)

The results of the comparison of the performance the complex coagulant and conventional iron sulfate and aluminum sulfate coagulants are presented in Fig. 3.13. This figure shows that the complex coagulant has significant advantages when the coagulants dosages are lower than 20 ppm, and it is capable of removing 94% turbidity at a dosage of 1 ppm, which indicates that the complex coagulant is over

85% more effective than both conventional sulfates coagulants. Therefore, at the same turbidity removal level, the consumption of the complex coagulant is much less than either iron sulfate or aluminum sulfate coagulant, and leaves less iron or aluminum residue in the treated water.

3.5 CONCLUSIONS

Fly ash containing high concentrations of Fe_2O_3 and Al_2O_3 was successfully used in producing complex coagulant by reacting with sulfuric acid. Sulfur dioxide was removed simultaneously by reacting with sodium chlorate, the added oxidant. There are several factors affecting the SO_2 removal efficiency. First of all, the removal efficiency of SO_2 is greatly influenced by the reaction temperature. Secondly, the gas dispersing methods also impact the SO_2 removal efficiency. In addition, the concentration of SO_2 in feed can play an important role in SO_2 removal. The conversion of Fe_2O_3 and Al_2O_3 in fly ash is affected greatly by both reaction temperature and time. The produced complex coagulant is effective in removing TSS in an ethanol fermentation wastewater and turbidity in kaolinite suspended in tap water. The removal of turbidity has an optimal pH range of 7.5-8.5. For TSS removal, the complex coagulant favors neutral pH value. The produced complex coagulant performed much better than the conventional iron and aluminum sulfates at low concentrations. A possible concern of this procedure is the produced waste, since the inactive silicate and aluminosilicate cannot be extracted. However, the waste could be

used in producing cement if the physical and chemical properties meet the requirement. More research is warranted to test this hypothesis.

3.6 ACKNOWLEDGEMENT

3.7 REFERENCES

References

1. S.J. Smith, E. Conception, R. Andres, J. Lurz, Historical Sulfur Dioxide Emissions 1850-2000, Pacific Northwest National Laboratory Report, 2004.

2. K. Wark, C. F. Warner, W. T. Davis, Air pollution: its origin and control, 3rd edn., Addison Wesley Longman 1998, pp.400-429.

3. WHO Regional Office of Europe, Air Quality Guidelines, 2000.

4. J. Kaminski, Technologies and costs of SO_2 emissions reduction from the energy sector, Appl. Energy 75 (2003) 165-172.

5. G. Van Houte, Desulfurization of flue gases in fluidized beds of modified limestone, J. Air Pollut. Control Assoc. 28 (10) (1978) 1030-1033.

6. M.B. Chang, J.H. Balbach, M. J. Rood, M.J. Kushner, Removal of SO_2 from gas streams using a dielectric barrier discharge and combined plasma photolysis, J. Appl. Phys. 69(1991) 4409-4417.

7. L.M. Dong, Z. Wu, J.X. Yang, X.C. Chi, Chemical kinetics model for sulfur dioxide removal in flue gas using corona discharge, Annual Report Conference on Electrical Insulation and Dielectric Phenomena, 2003.

8. W.M. Sun, B. Pashaie, S. Dhali, F.I. Honea, Non-thermal plasma remediation of SO_2/NO using a dielectric barrier discharge, J. Appl. Phys. 79 (1995) 3438-3444.

9. Y.H. Shi, M.H. Fan, N. Li, R.C. Brown, S.W. Sung, The recovery of acetic acid with sulfur dioxide,   Biochem. Eng. J. 22 (3) (2005) 207-210.

10. Y.H. Shi, M. Fan, N. Li, R.C. Brown, J.(H). van Leeuwen, The extraction of lactic acid with sulfur dioxide, Biochem. Eng. J. 24(2005) 157-160.

11. M. Fan, R.C. Brown, S.W. Sung, Y. Zhuang, A process for synthesizing polymeric ferric sulfate using sulfur dioxide from coal combustion, Proceedings - Annual International Pittsburgh Coal Conference 17th. (2000), 2222-2229.

12. A.D. Butler, M. Fan, R.C. Brown, A.T. Cooper, J.H. van Leeuwen, S. Sung, Absorption of dilute SO_2 gas stream with conversion to polymeric ferric sulfate for use in water treatment, Chem. Eng. J. 98(2004), 265-273.

13. American Coal Ash Association (ACAA), Fly ash facts for highway engineers, 2003.

14. W.L. Daniels, B. Stewart, K. Haering, C. Zipper, The potential for beneficial reuse of coal fly ash in southwest Virginia mining environment, Powell River Project. Virginia Polytechnic Institute and State University, 2002.

15. H. Rostami, W. Brendley, Alkali ash material: a novel fly ash based cement, Environ. Sci. Technol. 37(2003), 3454-3457.

16. C.F. Cai, Q. Chu, Y.L. Wang, Preparation and ceramic composite from fly ash and industrial sludge by sintering and its application, Shanghai Huanjing Kexue, , 25(2006), 51-54 (In Chinese).

17. D.M. Wang, L.C. Chen, A method for manufacturing geopolymer cement, based on fly ash. Faming Zhuanli Shengqing Gongkai Shuomingshu, 2006, CN 1007-7649, 20050622 (patent written in Chinese).

18. S.M. Pathan, L.A.G. Aylmore, T.D. Colmer, Properties of several fly ash materials in relation to use as soil amendments, J. Environ. Qual. 32 (2003) 687-693.

19. I.A.M. Yunusa, D. Eamus, D.L. DeSilva, Fly ash: an exploitable resource for management of Australian agricultural soils, Fuel 85 (2006) 2337-2344.

20. N. Kalra,   M.C. Jian, H.C. Joshi, et al., Fly ash a soil conditioner and fertilizer, Bioresour. Technol. 64(1998) 163-167.

21. N. Kalra, R.C. Harit, S.K. Sharma, Effect of fly ash incorporation on soil properties of texturally variant soils, Bioresour. Technol. 75(2000) 91-93.

22. S.M. Pathan, L.A.G. Aylmore, T.D. Colmer, Properties of several fly ash materials in relation to use as soil amendments, J. Environ. Qual. 32(2003) 687-693.

23. K. Majumdar, N. Singh, Effect of soil amendments on sorption and mobility of metribuzin in soils, Chemosphere, 66 (2007) 630-637.

24. I.A.M. Yunusa, D. Eamus. D.L. DeSilva, B.R. Murray, M.D. Burchett, G.C. Skilbeck, C. Heidrich Fly ash: an exploitable resource for management of Australian agricultural soils, Fuel 85 (2006) 2337-2344.

25. W. J. Greenlees,   J. M. Pitt,   M. R. Dawson,   C. D. Chriswell,   S. W. Melvin, Stabilizing cattle feedlot soil with fluidized bed combustor ash, Transactions of the American Society of Agricultural Engineers, 41(1) (1998), 203-211.

26. S.K. Rautaray, B.C. Ghosh, B.N. Mittra, Effect of fly ash, organic waste and chemical fertilizers on yield, nutrient uptake heavy metal content and residual fertility in a rice-mustard cropping sequence under acid lateritic soils, Bioresour. Technol. 90(2003)   275-283.

27. L.P. Singh, Z.A. Siddiqui, Effects of fly ash and *Helminthosporium oryzae* on growth and yield of three cultivars of rice, Bioresour. Technol. 86 (2003) 73-78.

28. D. Chatterjee, B. Ruj, A. Mahata, Adsorption and photocatalysis of color removal from waste water using fly ash and sunlight, Catal. Commun. 2 (2001) 113-117.

29. G.S. Gupta, G. Prasad, V.N. Singh, Removal of chrome dye from aqueous solutions by mixed adsorbents fly ash and coal. Water Res. 24 (1990) 45-50.

30. D. Chatterjee, B. Ruj, A. Mahata, Adsorption and photocatalysis of color removal from waste water using fly ash and sunlight, Catal. Commun. 2 (2001) 113-117.

31. D. Mohan, K.P. Singh, G. Singh, K. Kumar, Removal of dyes from wastewater using fly ash, a low cost adsorbent. Ind. Eng. Chem. Res. 41(2002) 3688-3695.

32. V.V.B. Rao, S.R.M. Rao, Adsorption studies on treatment of textile dyeing industrial effluent by fly ash, Chem. Eng. J. 116 (2006) 77-84.

33. K. Ravikumar, S. Ramalingam. S. Krishnan, K. Balu, Application of response surface methodology to optimize the process variables for reactive red and acid brown dye removal using a novel adsorbent, Dyes Pigments 70 (2006) 18-26.

34. K.C. Cheung, T.H. Venkitachalam, Improving phosphate removal of sand infiltration system using alkaline fly ash, Chemosphere 41(2000) 243-249.

35. N. Moreno, X. Querol, C. Ayora, Utilization of zeolites synthesized from coal fly ash for the purification of acid mine waters, Environ. Sci. Technol. 35 (2001) 3526-3534.

36. M. Fan, R.C. Brown, T.D. Wheelock, A.T. Cooper, M. Nomura, Y. Zhuang, Production of a complex coagulant from fly ash, Chem. Eng. J. 106 (2005) 269-277.

37. R.D. Myers, M. Ghosh, J. B. MacLeod, M. K. Bridle, Integrated water treatment and flue gas desulfurization process, 2006, United States Patent 7037434.

38. E. Cereda, G.M. Braga, Marcazzan, M. Pedretti, G.W. Grime, A. Baldacci, Occurrence mode of major and trace elements in individual fly ash particles, Nucl. Instrum. Methods Phys. Res., Sect. B 104 (1995) 625-629.

39. J.C. Hower, J.D. Robertson, G.A. Thomas, A.S. Wong, W.H. Schram, U.M. Graham, R.F. Rathbone, T.L. Robl, Characterization of fly ash from Kentucky power plants, Fuel 75 (4) (1996) 403-411.

40. R. Giere, L.E. Carleton, G.R. Lumpkin, Micro and nanochemistry of fly ash from a coal fired power plant, Am. Mineral. 88 (2003) 1853-1865.

41. M. Fan, R.C. Brown, S. Sung, C.P. Huang, S.K. Ong, J.(H.) van Leeuwen, Comparison of polymeric and conventional coagulants in arsenic(V) removal, Water Environ. Res. 75 (2003) 308-313.

CHAPTER 4 THE KINETICS OF SO$_2$ SCRUBBING WITH FLY ASH SLURRY WITH CONCOMITANT PRODUCTION OF A USEFUL WASTEWATER COAGULANT

A paper to be submitted to the Journal of Hazardous Materials

Ling Li[a], Maohong Fan[b], Robert C. Brown[c], Jacek A. Koziel[d,a], J(Hans) van Leeuwen[*a,d,e]

[a] Department of Civil and Environmental Engineering, Iowa State University, Ames, IA, 50011

[b] School of Materials Science and Engineering, Georgia Institute of Technology, Atlanta, GA, 30332

[c] Center for Sustainable Environmental Technologies, Iowa State University, Ames, IA, 50011

[d] Department of Agricultural and Biosystems Engineering, Iowa State University, Ames, IA, 50011

[e] Department of Food Science and Human Nutrition, Iowa State University, Ames, IA, 50011

[*] Corresponding author. Tel.:+1-515-294-5251, Fax: +1-515-294-8216, Email: leeuwen@iastate.edu

4.1 ABSTRACT

This research was aimed at recovering iron Fe and Al compounds to produce a useful complex coagulant from fly ash using SO$_2$ from flue gas oxidized to SO$_3$ by NaClO$_3$. The reaction kinetics of wet SO$_2$ scrubbing from simulated flue gas with fly ash slurry was studied. The SO$_2$ scrubbing experiments were carried out in a jacketed glass reactor system with a simulated flue gas containing SO$_2$ and N$_2$ in the gas phase and fly ash slurry in the liquid phase. Sodium chlorate was added to oxidize SO$_2$ to SO$_3$, producing H$_2$SO$_4$ in the slurry. The reaction orders of both Fe$_2$O$_3$ and Al$_2$O$_3$

extraction from unground fly ash slurry were shown to be 1.5th order and that of ground fly ash slurry were both shown to be of the order of 1.1. The empirical Arrhenius expressions were also derived from the reaction rate constants obtained at each reaction temperature. Reaction kinetics of ground and unground fly ash were compared showing that particle size and surface area have great impacts of the reaction rate. The mass transfer process of SO_2 with ClO_3^- was semi-quantified using a two-film theory model and the mass transfer coefficient under the experimental conditions was also evaluated.

Key words: fly ash; SO_2 absorption; reaction kinetics

4.2 INTRODUCTION

The emission of SO_2 in flue gas from coal combustion is a worldwide problem [1]. The most harmful impact of SO_2 on the environment is acid rain, which causes acidification of water bodies, soils, corrosion of material surfaces, and reduced growth of plants. In addition, when present with humidity in the air, SO_2 increases secondary fine particulate pollutant levels and reduces visibility [2]. Wet and dry SO_2 scrubbing with calcium sorbents have been used as the main SO_2 removal technologies for decades. However, the primary disadvantage of this traditional technique is the disposal of large amounts of byproduct slurry and separation and/or dewatering costs on top. Therefore, any possible use for SO_2 would be very attractive. Recent studies in our research group show that SO_2 can be used as a raw material in producing

polymeric ferric sulfate (PFS), an effective wastewater treatment coagulant, using inexpensive ferrous sulfate solution and sodium chlorate [3, 4].

Another important waste from coal combustion is fly ash, which is a fine particulate material rich in Si, Fe, and Al oxides. Trace elements, like Ca, Mg, Na, K are also present. The total amount of aluminum and iron oxides in fly ash can be as high as 75% [5], making it possible to extract those compounds for the production of aluminum sulfate and ferric sulfate, which are important wastewater treatment coagulants. Most iron- and aluminum-based sulfates on the market are produced from their ores. However, decreasing supplies of the minerals increase the cost of producing iron- and aluminum-based sulfates from the ores.

We have demonstrated the possibility of producing a complex polymeric Fe-Al coagulant by absorption and oxidation of SO_2 in fly ash slurry. This is providing a significant advantage for SO_2 removal using a power plant waste material and producing a valuable byproduct. Fan *et al.* investigated the synthesis and properties of PFS with SO_2 and proved that PFS had advantages over either $Al_2(SO_4)_3$ or $Fe_2(SO_4)_3$ [6, 7]. In addition, PFS is less corrosive and leaves less iron residual in water compared to other traditional iron coagulants [6]. Recent research in our group also demonstrated that the complex polymeric coagulant containing both polymeric aluminum sulfate (PAS) and polymeric ferric sulfate (PFS) performed better than conventional iron- and aluminum-based coagulants in removing the colloidal fraction of chemical oxygen demand (COD), turbidity and arsenic from water [8]. Considering the advantages and disadvantages of individual Fe- and Al-based coagulants, a

complex coagulant composed of both iron and aluminum could provide an alternative solution to the coagulation of wastewater [9]. Although fly ash containing suitable amounts of Fe and Al can be used as the raw material to produce Fe- and Al-based complex coagulant, it is important to consider the potential leaching problem. Some researchers observed trace elements leaching from fly ash, resulting in ground water and soil contamination [10]. Therefore, a case-by-case test of fly ash application is still necessary.

The performances of the produced complex coagulant in the removal of total suspended solids and turbidity have been evaluated in our previous research [3, 6]. However, in order to develop this technology into a commercial process, more research needs to be done, and reaction kinetics is one of the most important aspects. This paper focuses on investigating the reaction kinetics of Fe_2O_3 and Al_2O_3 in fly ash with H_2SO_4 for their reaction orders and Arrhenius expressions under different reaction conditions. The optimum conditions of producing the complex coagulant from fly ash with the absorption of SO_2 were determined based on the reaction kinetics.

4.3 THE CHEMISTRY OF PRODUCING POLYMERIC COAGULANTS

T The production of the complex polymeric iron-aluminum coagulant from fly ash with the absorption of SO_2 consists of the following steps.

Fe$_2$O$_3$ and Al$_2$O$_3$ in fly ash react quickly with the added H$_2$SO$_4$ to produce Fe^{3+} and Al^{3+} (reaction 1 and 2).

$$Fe_2O_3 + 3H_2SO_4 \Rightarrow 3H_2O + Fe_2(SO_4)_3 \tag{1}$$

$$Al_2O_3 + 3H_2SO_4 \Rightarrow 3H_2O + Al_2(SO_4)_3 \tag{2}$$
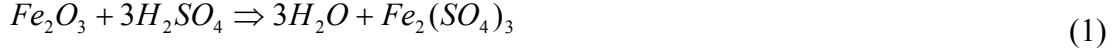
When SO$_2$ from the simulated flue gas dissolves in water, ClO$_3^-$ in the fly ash slurry oxidizes SO$_2$ to SO$_3$, resulting in additional SO$_4^{2-}$ and H$^+$ (reactions 3 and 4),

$$SO_2 \Leftrightarrow SO_{2(aq)} \tag{3}$$

$$ClO_3^- + 3H_2O + 3SO_2 \Rightarrow 3SO_4^{2-} + 6H^+ + Cl^- \tag{4}$$
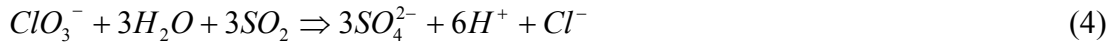
Hydrolysis of iron and aluminum sulfates follows (reactions 5, 6 and 7)

$$H_2O \Leftrightarrow H^+ + OH^- \tag{5}$$

$$2Fe^{3+} + \frac{6-n}{2}(SO_4^{2-}) + n(OH^-) \Rightarrow [Fe_2(OH)_n(SO_4)_{\frac{6-n}{2}}] \tag{6}$$

$$2Al^{3+} + \frac{6-m}{2}(SO_4^{2-}) + m(OH^-) \Rightarrow [Al_2(OH)_m(SO_4)_{\frac{6-m}{2}}] \tag{7}$$
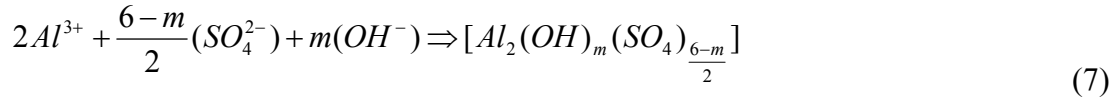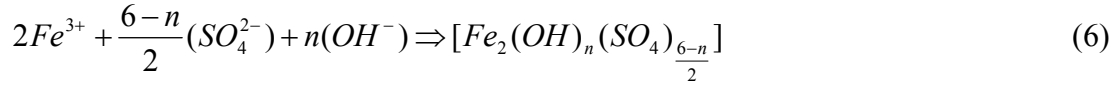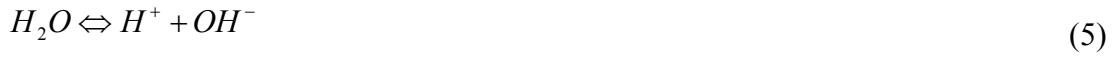
Polymerization of ferric sulfate (PFS) and polymeric aluminum sulfate (PAS) follows (reactions 8 and 9) [8].

$$p[Fe_2(OH)_n(SO_4)_{\frac{6-n}{2}}] \Rightarrow [Fe_2(OH)_n(SO_4)_{\frac{6-n}{2}}]_p \tag{8}$$

$$q[Al_2(OH)_n(SO_4)_{\frac{6-m}{2}}] \Rightarrow [Al_2(OH)_m(SO_4)_{\frac{6-m}{2}}]_q \tag{9}$$
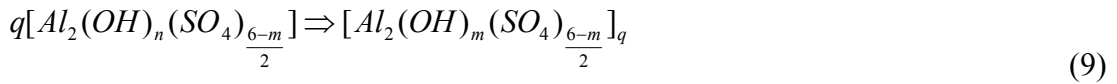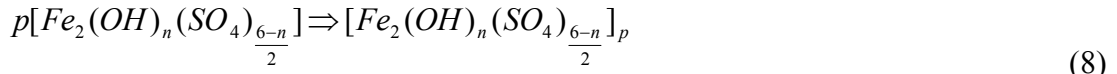
The produced PFS and PAS based complex coagulate were successfully used in the removal of total suspended solids and turbidity in wastewater. This paper focuses on determining reaction kinetics in order to optimize the reaction conditions.

4.4 EXPERIMENTAL ASPECTS

4.4.1 APPARATUS

The reaction of Fe_2O_3 and Al_2O_3 in fly ash with H_2SO_4 was conducted in a 500 ml jacketed glass reactor (ChemGlass Inc., Vineland, NJ, USA). The schematic of the reaction system used to determine reaction kinetics is shown in Fig. 4.1. There are five inlets on the reactor lid. A Teflon propeller was connected through the center inlet, stirring at 200 rpm. Prepared fly ash slurry was introduced into the reactor through the inlet with a funnel. A pump was connected to this inlet to periodically dose oxidizer, i.e. $NaClO_3$ solution, as needed. After the fly ash slurry was added into the reaction, stirring with the propeller was started, the funnel was removed and the inlet was sealed carefully with a glass stopper. A thermometer for temperature monitoring was connected to the third inlet. The fourth inlet was used to introduce the simulated flue gas, which contained N_2 and SO_2, into the reactor. The fifth inlet was connected to a condenser, through which the outlet gas stream was released into the hood. The condenser was used to avoid water vapor escape in the outlet gas stream and return the condensate back to the reactor. A ZRF NDIR gas analyzer (Fuji Electric Co., Tokyo, Japan) was used to analyze SO_2 concentration in the outlet gas stream. A Dow Corning Fluid (Dow Chemical Co., Midland, MI, USA) was circulated through the reactor jacket by a Neslab RTE 111 heater unit.
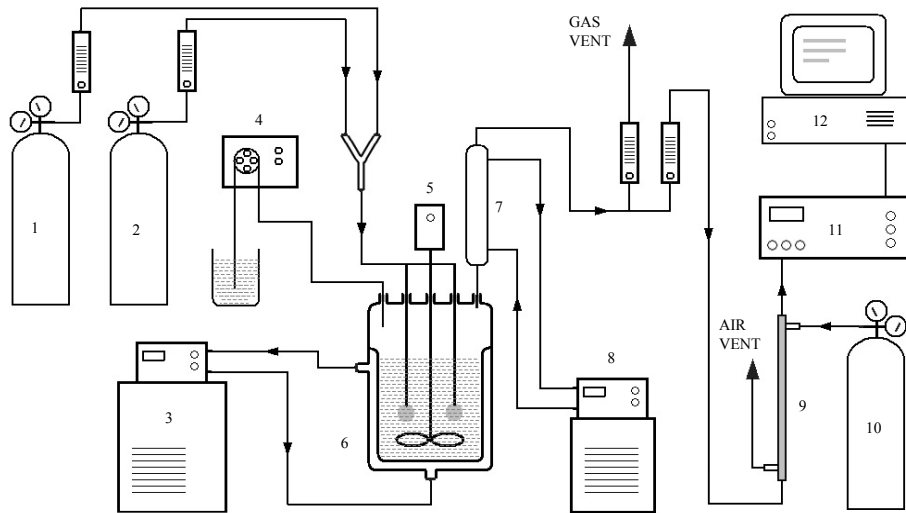
1. Nitrogen tank   2. Simulated flue gas tank   3. Reactor heater unit   4. Oxidizer pump

5. Stirrer motor   6. Jacketed reactor   7. Condenser   8. Condenser chiller unit

9. Sample gas dryer   10. Air tank   11. Gas analyzer   12. Data acquisition computer

Fig.4. 1 Laboratory flue gas scrubber for the simultaneous synthesis of a complex coagulant from fly ash and flue gas

4.4.2 OPERATION PROCEDURES

The fly ash sample was provided by HeadWaters Resource Inc. (South Jordan, UT, USA). The contents of Fe_2O_3 and Al_2O_3 in the fly ash were 25.48% and 21.03% respectively. In order to minimize the influence of soluble alkali, the fly ash sample was washed with hot water and dried at 115 °C before being cooled down to room temperature. In each run, 100 g pretreated fly ash and 100 ml water were added into the reactor through a funnel. The fly ash slurry was stirred at 200 rpm at room temperature for about 1 hour to obtain a homogenous distribution. A heater unit was used to control the reaction temperature, which was monitored with a thermometer inserted into the reactor. When the desired temperature was reached, 3.6 M H_2SO_4 was introduced into the reactor through a funnel and the simulated flue gas was bubbled through the stirred fly ash slurry at the same time. The flue gas was simulated

by mixing 4% SO_2 and nitrogen to make a final concentration of SO_2 was controlled around 4000 ppm, which is at the high end of sulfur dioxide concentration in flue gas [11]. Sodium chlorate was added into the reactor system after the simulated flue gas was introduced, resulting in the oxidation of SO_2. This experiment was run at seven different temperatures, 70, 80, 90, 100, 110, 120, and 130 °C for 6 hours. The mixture was sampled with a 1 ml pipette every 30 min.

4.4.3 DETERMINATION OF THE CONCENTRATIONS OF SO₂, IRON AND ALUMINUM

The concentrations of SO_2 were analyzed with a ZRF NDIR gas analyzer, which was calibrated with a 0.5% SO_2 gas before each run. The concentrations of Al^{3+} in the produced coagulant were analyzed with an Agilent HP-4500 ICP-MS (Agilent Technologies, Santa Clara, CA, USA). The analysis of total Fe^{3+} in the produced coagulant was completed with a HACH 3000 (Hach Company, Loveland, CO, USA) spectrophotometer. All the samples were diluted properly according to the detection limits of the instrument prior to the analysis, and the instrument was calibrated with standard solutions at different concentrations before each run. A potassium permanganate titration method was used to determine ferrous iron concentration in the final product.

4.5 RESULTS AND DISCUSSION

4.5.1 DETERMINATION OF REACTION MECHANISM

Concentrations of $Fe_2(SO_4)_3$ and $Al_2(SO_4)_3$ in the produced complex coagulant are listed in Table 4.1 and 4.2, The concentrations of both Fe^{3+} and Al^{3+} increased with time and reaction temperature. Since H_2SO_4 takes part in the conversion of Fe_2O_3 and Al_2O_3 in the fly ash, we derived the reaction kinetics based on the change of H_2SO_4 concentration. Let C_{s0} be the initial concentration of H_2SO_4, C_s be the concentration of H_2SO_4 in the reaction, and C_f and C_a be the concentration of $Fe_2(SO_4)_3$ and $Al_2(SO_4)_3$ respectively. According to the theory of multiple reactions, Eqs (1) and (2) can be considered as rreversible parallel reactions [12, 13]. Since Fe_2O_3 and Al_2O_3 are solids, the reaction rate of $Fe_2(SO_4)_3$ and $Al_2(SO_4)_3$ formation can be expressed as below.

$$\frac{dC_f}{dt} = k_1[C_s]^{n_1} \tag{10-a}$$

$$\frac{dC_a}{dt} = k_2[C_s]^{n_2} \tag{11-a}$$

Because H_2SO_4 takes part in the reaction of both Fe_2O_3 and Al_2O_3 in the fly ash, the change of H_2SO_4 concentration is in proportion to the change of overall concentration of both $Fe_2(SO_4)_3$ and $Al_2(SO_4)_3$. Therefore, Eq.(10-a) and (11-a) can be expressed as

$$\frac{dC_f}{dt} = k_1[C_{s0} - 3(C_f + C_a)]^{n_1} \tag{10-b}$$

$$\frac{dC_a}{dt} = k_2[C_{s0} - 3(C_f + C_a)]^{n_2} \tag{11-b}$$

After dividing Eq. (10) by Eq. (11), we get

$$\frac{dC_f}{dC_a} = \frac{k_1}{k_2}[C_{s0} - 3(C_f + C_a)]^{n_1 - n_2} \tag{12}$$

The ratio of $Fe_2(SO_4)_3$ and $Al_2(SO_4)_3$ concentrations should be constant at each temperature, which indicates that the reaction orders, n_1 and n_2 are equal [9]. The statistical confidence level of this calculation is 95%, which indicates that there is a 95% certainty that the ratio of $Fe_2(SO_4)_3$ and $Al_2(SO_4)_3$ concentrations is constant at each temperature. The ratio of $Fe_2(SO_4)_3$ and $Al_2(SO_4)_3$ concentrations is presented in Fig. 4.2. Let n equal to n_1 and n_2, then Eq. (10) and (11) can be presented as:

$$\frac{dC_f}{dt} = k_1[C_{s0} - 3(C_f + C_a)]^n \tag{13}$$

$$\frac{dC_a}{dt} = k_2[C_{s0} - 3(C_f + C_a)]^n \tag{14}$$

The sum of Eq. (13) and (14) gives

$$\frac{d(C_f + C_a)}{dt} = (k_1 + k_2)[C_{s0} - 3(C_f + C_a)]^n \tag{15}$$

Since n_1 and n_2 are equal, Eq. (12) can be simplified to

$$\frac{dC_f}{dC_a} = \frac{k_1}{k_2} \tag{16}$$

Integration of Eq. (16) gives

$$C_f = \frac{k_1}{k_2} C_a + C_{t,0} \tag{17}$$

where $C_{t,0}$ is the constant at t = 0. Since when the reaction started, the concentrations of both $Fe_2(SO_4)_3$ and $Al_2(SO_4)_3$ are zero, $C_{t,0}$ must be zero. Therefore, the relationship of k_1 and k_2 can be derived from Eq. (17)

$$\frac{k_1}{k_2} = \frac{C_f}{C_a} \tag{18}$$

Integration of Eq. (15) results in

$$\frac{1}{[C_{s0} - 3(C_f + C_a)]^{n-1}} = 3(n-1)(k_1 + k_2)t + \frac{1}{C_{s0}^{n-1}} \tag{19}$$

The values of C_f and C_a measured in the experiments are listed in Table 4.1 and 4.2, and C_{s0} is 3.6 M. The relationship between $1/[3.6-3(C_f + C_a)]^{0.5}$ and t is plotted in Fig. 4.3. The linear relationship indicates that the value of n is 1.5, in other words, the reaction order of reaction (13) or (14) is 1.5. Therefore, Eq. (19) can be simplified to

$$\frac{1}{[C_{s0} - 3(C_f + C_a)]^{0.5}} = 1.5(k_1 + k_2)t + \frac{1}{C_{s0}^{0.5}} \tag{20}$$

The slope can be used to calculate k_1 and k_2 from Eq. (20):

$$k_1 + k_2 = \frac{1}{1.5} slope \tag{21}$$

The simultaneous solution of Eq. (18) and (21) provides the reaction constants, k_1 and k_2. The values of k_1 and k_2 are listed in Table 4.3.

Table 4. 2 Concentrations of $Fe_2(SO_4)_3$ (mol/L) in the complex coagulant produced under different conditions

time, min	70 ºC	80 ºC	90 ºC	100 ºC	110 ºC	120 ºC	130 ºC
30	0.0291	0.0294	0.0421	0.0617	0.0872	0.0828	0.1177
60	0.0325	0.0360	0.0591	0.0730	0.1036	0.1155	0.1529
90	0.0377	0.0439	0.0715	0.0921	0.1334	0.1597	0.1780
120	0.0463	0.0499	0.0779	0.1016	0.1462	0.1937	0.2220
150	0.0521	0.0577	0.0914	0.1213	0.1663	0.2032	0.2471
180	0.0613	0.0661	0.1049	0.1368	0.1876	0.2354	0.2835
210	0.0659	0.0740	0.1190	0.1452	0.2155	0.2644	0.3249
240	0.0751	0.0806	0.1325	0.1631	0.2393	0.2852	0.3463
270	0.0832	0.0914	0.1461	0.1732	0.2587	0.3211	0.3676
300	0.1016	0.1083	0.1490	0.1881	0.2666	0.3338	0.3902
330	0.1068	0.1125	0.1625	0.2102	0.2904	0.3640	0.4166
360	0.1120	0.1215	0.1866	0.2305	0.3250	0.3981	0.4379

Table 4. 3 Concentrations of $Al_2(SO_4)_3$ (mol/L) in the complex coagulant produced under different conditions

time, min	70 ºC	80 ºC	90 ºC	100 ºC	110 ºC	120 ºC	130 ºC
30	0.0663	0.0809	0.0966	0.1219	0.1304	0.1816	0.1647
60	0.0783	0.0959	0.1247	0.1381	0.1471	0.2025	0.1889
90	0.0838	0.1092	0.1493	0.1575	0.1641	0.2535	0.2328
120	0.1021	0.1143	0.1653	0.1840	0.1763	0.2818	0.2706
150	0.1094	0.1445	0.1704	0.1927	0.1983	0.3115	0.2943
180	0.1185	0.1548	0.1927	0.2151	0.2208	0.3390	0.3199
210	0.1359	0.1722	0.2161	0.2289	0.2522	0.3701	0.3297
240	0.1459	0.1855	0.2280	0.2427	0.2684	0.3918	0.3696
270	0.1592	0.1997	0.2368	0.2591	0.2939	0.4129	0.4082
300	0.1635	0.2206	0.2568	0.2812	0.3008	0.4379	0.4327
330	0.1709	0.2493	0.2768	0.2961	0.3402	0.4493	0.4762
360	0.1895	0.2628	0.3063	0.3440	0.3739	0.4802	0.5054

Table 4. 4 Reaction rate constant for reaction (1) and (2) at different temperatures

Temperature	70ºC	80ºC	90ºC	100ºC	110ºC	120ºC	130ºC
$k_1 \times 10^5$ (mole$^{-0.5} \cdot$L$^{0.5} \cdot$s^{-1})	4.114	5.198	8.160	11.065	19.935	32.595	46.994
$k_2 \times 10^5$ (mole$^{-0.5} \cdot$L$^{0.5} \cdot$s^{-1})	8.079	12.156	15.141	17.797	24.070	47.059	54.746
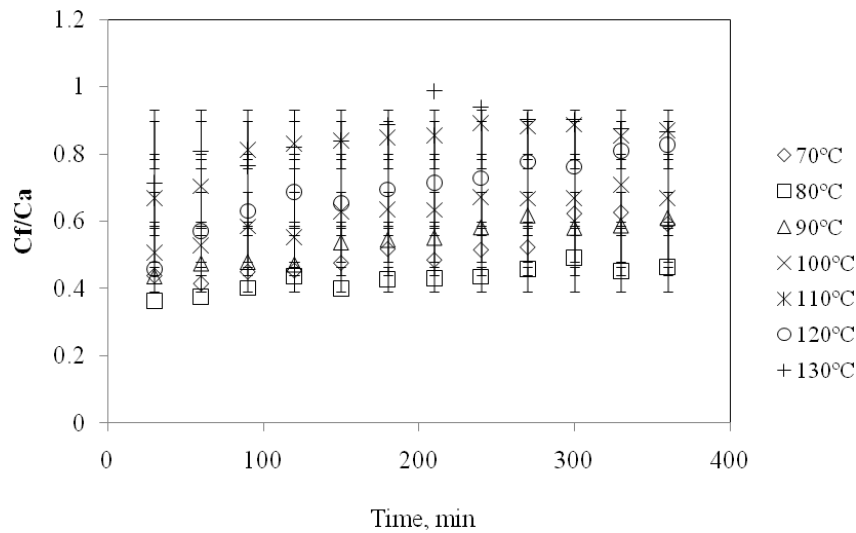
Fig.4. 2 Ratio of $Fe_2(SO_4)_3$ and $Al_2(SO_4)_3$ concentrations at different reaction times and temperatures (confidence level is 95%)
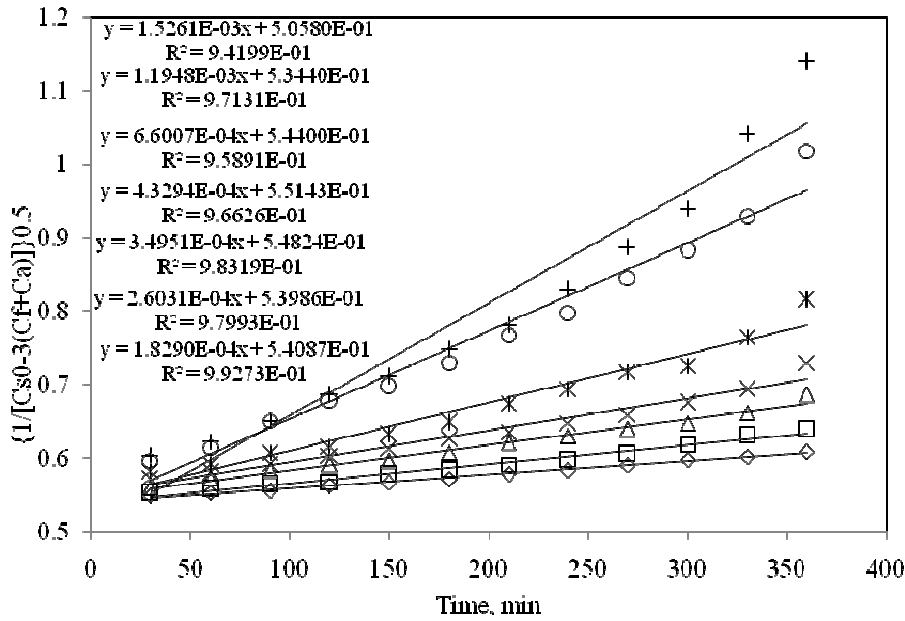
Fig.4. 3 The relationship between $\{1/[C_{s0}-3(C_f+C_a)]\}^{0.5}$ and time t used to determine reaction rates k_1 and k_2 at different temperatures

4.5.2 DETERMINATION OF ARRHENIUS EXPRESSIONS

The Arrhenius expression has been used to present the relationship between

reaction rate constant and reaction temperature, as shown in Eq. (22).

$$k(T) = A\exp(\frac{-E}{RT}) \tag{22}$$

where A is frequency factor, E is activation energy (J/mole), T is absolute temperature

(K) and R is gas constant (8.314 J/mole•K). Since this experiment was conducted in a

relatively narrow temperature range (70-130 ºC), the variation of frequency factor and

activation energy can be neglected [9, 12]. The values of A and E for reaction (1) and

(2) can be determined by the plotting $-ln(k)$ vs. $1/T$, which indicates a linear

relationship between $-\ln(k)$ and 1/T, with regression coefficient higher than 95%, as

shown in Fig. 4.4. The relationship of the measured reaction rate constant and

temperature can then be presented as below:

$$k_1(T) = 843.027 \exp(\frac{-4.852 \times 10^4}{RT})$$ (23)

$$k_2(T) = 26.923 \exp(\frac{-3.641 \times 10^4}{RT})$$ (24)

These results show that the activation energy of reaction (1) is greater than that of reaction (2), indicating that the reaction of Al_2O_3 is more sensitive to the reaction temperature.
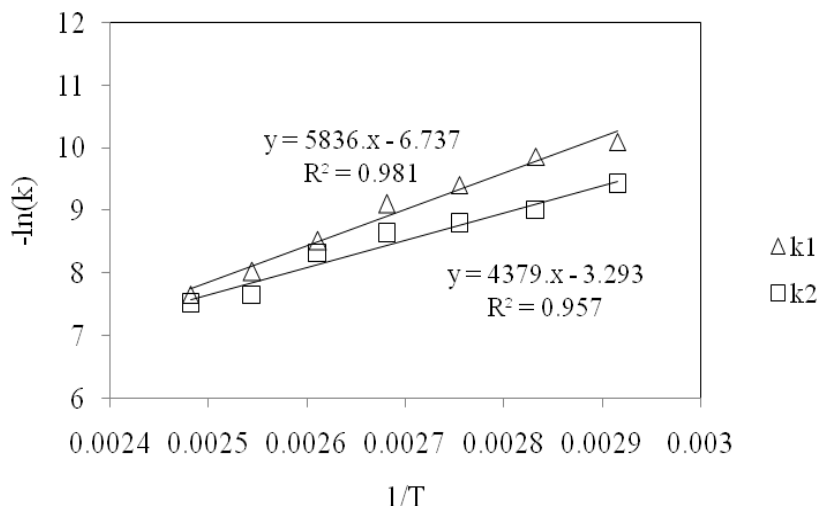
Fig.4. 4 Plots of $-\ln(k)$ and $1/T$ to calculate the constants in Arrhenius expression
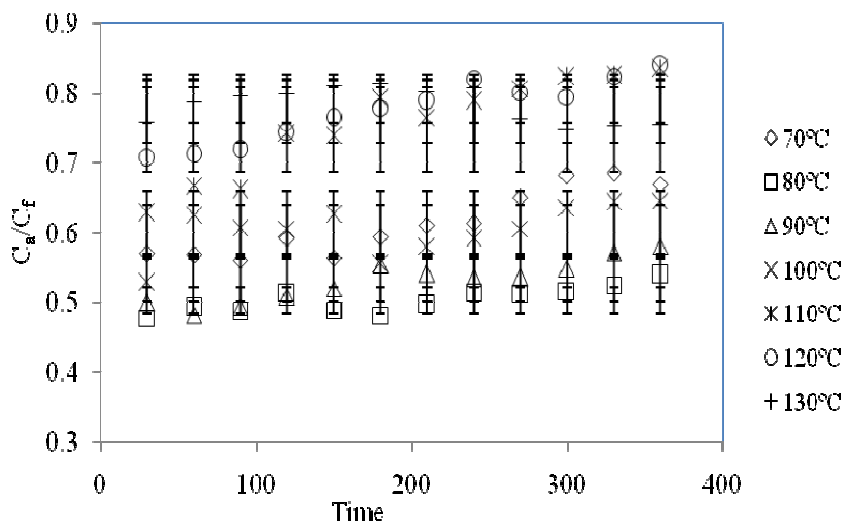
Fig.4. 5 Ratio of $Fe_2(SO_4)_3$ and $Al_2(SO_4)_3$ concentrations for ground fly ash at different reaction times and temperatures (confidence level is 95%)

4.5.3 KINETICS USING GROUND FLY ASH

To improve the conversion efficiency of Fe_2O_3 and Al_2O_3, the fly ash sample was ground and all the other experimental conditions were kept the same. The conversion efficiency of Fe^{3+} and Al^{3+} in the produced complex coagulant at 130 °C was increased by 10.6% and 11.7% , respectively. The increase in conversion efficiency for Fe^{3+} at different temperatures was in the range of 1.9-17.0%, and that for Al^{3+} was in the range of 1.5-11.7%. The concentrations of $Fe_2(SO_4)_3$ and $Al_2(SO_4)_3$ for the ground fly ash are listed in Table 4.4 and 4.5.

The reaction mechanism of ground fly ash is similar to that in the unground fly ash sample. The ratio of $Fe_2(SO_4)_3$ and $Al_2(SO_4)_3$ concentrations is presented in Fig. 4.5, which indicates that the ratio is constant with a statistical confidence level of 95%. Eq. (10) through Eq. (19) can be used to describe the reaction kinetics. When n is equal to 1.1, there is a good linear relationship between $1/[3.6-3(C_f +C_a)]^{0.1}$ and t, as shown in Fig. 6. Therefore, Eq. (19) can be written as

$$\frac{1}{[C_{s0} - 3(C_f + C_a)]^{0.1}} = 0.3(k_1 + k_2)t + \frac{1}{C_{s0}^{0.1}} \tag{25}$$

The slope can be used to calculate k_1 and k_2 from Eq. (25)

$$k_1 + k_2 = \frac{1}{0.3} Slope \tag{26}$$

Solve k_1 and k_2 by combining Eq. (18) and Eq. (26), and the results are listed in Table 4.6.

Table 4. 5 Concentrations of $Fe_2(SO_4)_3$ (mol/L) in the complex coagulant produced from the ground fly ash sample under different conditions

time, min	70 ºC	80 ºC	90 ºC	100 ºC	110 ºC	120 ºC	130 ºC
30	0.0598	0.0624	0.0653	0.0729	0.1059	0.1920	0.2218
60	0.0758	0.0805	0.0824	0.0957	0.1515	0.2466	0.2887
90	0.0824	0.0916	0.1000	0.1253	0.1796	0.2778	0.3141
120	0.0911	0.1085	0.1189	0.1475	0.2202	0.3234	0.3447
150	0.0992	0.1167	0.1324	0.1728	0.2433	0.3533	0.3832
180	0.1073	0.1237	0.1495	0.1919	0.2770	0.3794	0.4334
210	0.1124	0.1330	0.1572	0.2171	0.2958	0.4197	0.4502
240	0.1190	0.1430	0.1666	0.2276	0.3145	0.4522	0.4826
270	0.1281	0.1500	0.1761	0.2393	0.3314	0.4639	0.4881
300	0.1337	0.1576	0.1843	0.2560	0.3457	0.4678	0.4896
330	0.1383	0.1628	0.1931	0.2609	0.3576	0.4887	0.4976
360	0.1393	0.1663	0.1979	0.2640	0.3707	0.5017	0.5056

Table 4. 6 Concentrations of $Al_2(SO_4)_3$ (mol/L) in the complex coagulant produced from the ground fly ash sample under different conditions

time, min	70 ºC	80 ºC	90 ºC	100 ºC	110 ºC	120 ºC	130 ºC
30	0.1048	0.1308	0.1306	0.1375	0.1685	0.2714	0.2920
60	0.1335	0.1631	0.1712	0.1530	0.2268	0.3462	0.3666
90	0.1469	0.1883	0.2025	0.2063	0.2712	0.3867	0.3949
120	0.1538	0.2117	0.2337	0.2436	0.2966	0.4348	0.4312
150	0.1761	0.2389	0.2545	0.2752	0.3291	0.4616	0.4724
180	0.1807	0.2580	0.2701	0.3456	0.3497	0.4865	0.5326
210	0.1841	0.2683	0.2902	0.3737	0.3858	0.5321	0.5610
240	0.1938	0.2786	0.3111	0.3844	0.3985	0.5502	0.5969
270	0.1969	0.2934	0.3285	0.3951	0.4110	0.5787	0.6390
300	0.1961	0.3062	0.3356	0.4023	0.4194	0.5884	0.6541
330	0.2017	0.3110	0.3378	0.4053	0.4332	0.5920	0.6595
360	0.2081	0.3079	0.3406	0.4088	0.4437	0.5964	0.6684

Table 4. 7 Reaction rate constant of ground fly ash for reaction (1) and (2) at different temperatures

| Temperature, ºC	70	80	90	100	110	120	130
$k_1 \times 10^5$ (mole$^{-0.1} \cdot$L$^{0.1} \cdot$s^{-1})	6.331	10.270	13.625	24.507	35.740	91.970	159.824
$k_2 \times 10^5$ (mole$^{-0.1} \cdot$L$^{0.1} \cdot$s^{-1})	10.321	20.420	25.658	40.526	47.230	118.657	204.009
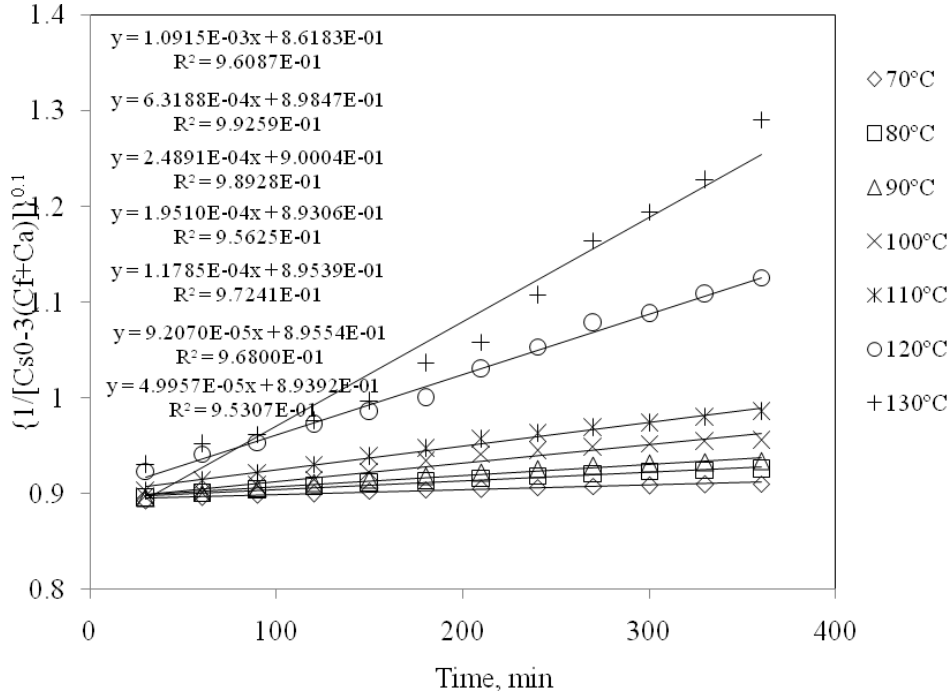
Fig.4. 6 The relationship between $\{1/[C_{s0}-3(C_f+C_a)]\}^{0.1}$ and time t used to determine reaction rates k_1 and k_2 for ground fly ash sample at different temperatures
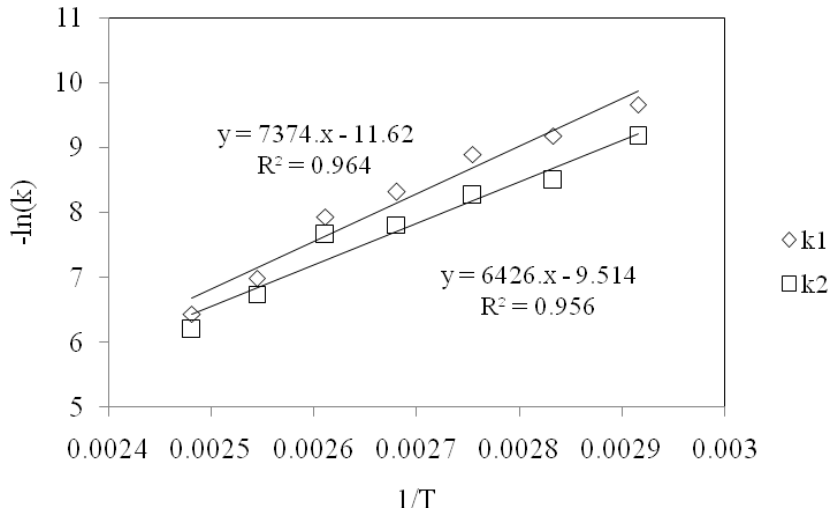
Fig.4. 7 Plots of $-ln(k)$ and $1/T$ to calculate the constants in Arrhenius expression for ground fly ash

Similarly, the values of A and E for ground fly ash for reaction (1) and (2) can be determined by the linear relationship between $-ln(k)$ and $1/T$, with regression coefficient higher than 95%, as shown in Fig. 4.7. The relationship of the reaction rate constant and temperature can then be presented as below

$$k_1(T) = 1.113 \times 10^5 \exp(\frac{-6.131 \times 10^4}{RT}) \tag{27}$$

$$k_2(T) = 1.355 \times 10^4 \exp(\frac{-5.343 \times 10^4}{RT})$$ (28)

Results in Table 4.6 show that the reaction rate constants for both reactions for ground fly ash are greatly improved at every reaction temperature, which indicates that reaction rate is apparently affected by particle size and structure. In a fluid-solid reaction system, the reaction rate constant increases with smaller particles [13]. In addition, grinding increased the surface area of the fly ash particles, which also helps in improving the reaction rate constant. Considering the mass transfer process between liquid phase and solid phase, smaller particle sizes caused by grinding increase the mass diffusivity, resulting in greater mass transfer efficiency, which also enhances reaction [14]. These results Eq. (27) and (28) show that the activation energy of reaction (1) is greater than that of reaction (2), indicating that the reaction of Al_2O_3 is more sensitive to the reaction temperature. Moreover, the increase in frequency factor for Al_2O_3 is more than that of Fe_2O_3, which indicates that the sensitivity of Al_2O_3 reaction to temperature is increased significantly more. The reason for this is that the aluminosilicate crystalline structure is destroyed by grinding, and more Al_2O_3 particles are present in the reaction system.

4.5.4 MASS TRANSFER EVALUATION OF SO$_2$ ABSORPTION

The kinetics of SO_2 absorption in wet limestone scrubbing has been studied since wet limestone scrubbing became a commercial flue gas desulfurization process in the 1970s. However, there are still some problems regarding SO_2 modeling, particularly the SO_2 absorption [15], which depends on reaction conditions. Therefore, a number

of preliminary experiments were run in order to evaluate the physical characteristics

of the gas-liquid mass transfer coefficients. The product of mass transfer coefficient

and specific surface area ($k_g a$) of gas phase was evaluated by purging SO_2 containing

gas into 0.1M NaOH solution, since SO_2 can be considered to be depleted completely

at such a high pH value and therefore the mass transfer of liquid phase can be

neglected. The product of mass transfer coefficient and specific surface area ($k_L a$) of

liquid phase was evaluated by using 0.1M HCl solution to absorb SO_2, where only

physical absorption is considered [16].

The absorption of SO_2 involves two steps, as shown in Eq. (3) and (4). The reaction

between dissolved SO_2 and sodium chlorate is instantaneous and irreversible;

therefore, most of the dissolved SO_2 is consumed by reaction (4) and the reaction

occurs at the gas-liquid interface. Assume each gas bubble follows a plug-flow pattern

in the reactor, the driving force for SO_2 absorption can be considered as the difference

of the average pressure of SO_2 in bulk flow and the partial pressure of SO_2 in

equilibrium with liquid phase, defined as p_{SO_2}, as shown in Eq. (29). The average

pressure of SO_2 in bulk flow can be evaluated by taking the logarithmic average of the

inlet and outlet pressure [16]. The physical properties of SO_2 absorption and

diffusivity are listed in Table 4.7 and the experimental results for SO_2 absorption are

summarized in Table 4.8.

$$\Delta p_{SO_2} = p_{SO_2}\big|_{ave} - H_{SO_2} C_{SO_2(aq)} \tag{29}$$

A diffuser was used to improve SO_2 removal efficiency. Based on the data in Table

4.7 and 4.8, the enhancement factor of SO_2 mass transfer and overall mass transfer

coefficient can be estimated. Since the reaction of SO_2 with ClO_3^- is instantaneous and irreversible, the enhancement factor for infinitely fast reaction Φ_a can be calculated using Eq. (30) [17].

$$\phi_a = 1 + \frac{C_{ClO_3^-,0}}{nC_{SO_2,0}} \left(\frac{D_{ClO_3^-}}{D_{SO_2}}\right)^{0.5} \tag{30}$$

where n is 1/3, the molar ratio of ClO_3^- to SO_2 in reaction (4), $C_{ClO_3^-}$ is the initial concentration of ClO_3^-, C_{SO_2} is the aqueous concentration of SO_2, $C_{ClO_3^-}$ and D_{SO_2} are the diffusivity coefficients of ClO_3^- and SO_2 respectively. With the value of Φ_a, the liquid film enhancement factor Φ can be evaluated using a graph method [17]. The overall mass transfer coefficient can be evaluated by Eq. (31).

$$\frac{1}{K_g a} = \frac{1}{k_g a} + \frac{1}{k_L a H \phi} \tag{31}$$

The results of mass transfer coefficient for SO_2 absorption with/without diffuser are summarized in Table 4.9.

Table 4. 8 Physical properties of SO_2 absorption and diffusivity

Temp. °C	Henry's constant, mol/(L.atm)[a]	D_{SO2} m²/s,[a]	D_{ClO3} m²/s,[a, b]	SO_2 rate constant k, s⁻¹[c]
70	0.396	1.9115×10^{-9}	1.510×10^{-9}	7.129×10^{8}
80	0.322	2.1858×10^{-9}	1.554×10^{-9}	6.952×10^{8}
90	0.270	2.5286×10^{-9}	1.645×10^{-9}	6.781×10^{8}
100	0.220	2.7715×10^{-9}	1.788×10^{-9}	6.613×10^{8}
110	0.184	3.2836×10^{-9}	1.997×10^{-9}	6.450×10^{8}
120	0.155	3.6502×10^{-9}	2.288×10^{-9}	6.290×10^{8}
130	0.132	4.0833×10^{-9}	2.688×10^{-9}	6.135×10^{8}

a: Ref. [18]

b: Ref. [19]

c: Ref. [20]

Table 4. 9 Experimental results for SO_2 absorption in fly ash slurry

Temp.	p_{SO_2}|in, atm	p_{SO_2}|out, atm		r_{SO_2}, mole/(m³.s)		$k_g a$, mole/(L.s. atm)		$k_L a$, s⁻¹	
ºC		No diffuser	with diffuser	No diffuser	with diffuser	No diffuser	with diffuser	No diffuser	with diffuser
70	0.0054	0.0020	0.0010	0.138	0.141	1.301×10^{-1}	1.962×10^{-1}	1.297×10^{-1}	2.966×10^{-1}
80	0.0054	0.0029	0.0010	0.196	0.206	9.054×10^{-2}	1.759×10^{-1}	9.930×10^{-2}	3.083×10^{-1}
90	0.0054	0.0057	0.0019	0.344	0.382	5.739×10^{-2}	1.160×10^{-1}	6.163×10^{-2}	2.310×10^{-1}
100	0.0054	0.0089	0.0036	0.472	0.552	3.703×10^{-2}	6.525×10^{-2}	4.539×10^{-2}	1.684×10^{-1}
110	0.0054	0.0113	0.0052	0.540	0.654	2.305×10^{-2}	4.392×10^{-2}	3.963×10^{-2}	1.148×10^{-1}
120	0.0054	0.0130	0.0064	0.570	0.711	1.414×10^{-2}	3.232×10^{-2}	2.105×10^{-2}	8.935×10^{-2}
130	0.0054	0.0139	0.0085	0.573	0.691	1.120×10^{-2}	2.455×10^{-2}	7.718×10^{-3}	6.856×10^{-2}

Table 4. 10 Mass transfer coefficients for SO_2 absorption in fly ash slurry

Temp.	Gas phase resistance L·s·atm/mole		Liquid phase resistance L·s·atm/mole		Overall resistance L·s·atm/mole		Overall mass transfer coefficient, mole/(L·s·atm)	
ºC	No diffuser	with diffuser	No diffuser	with diffuser	No diffuser	with diffuser	No diffuser	with diffuser
70	8.405	4.084	1.108×10^{-1}	1.108×10^{-1}	8.516	4.195	0.117	0.238
80	11.86	4.889	1.292×10^{-1}	4.596×10^{-2}	11.991	5.048	0.083	0.198
90	18.70	8.216	1.447×10^{-1}	1.243×10^{-1}	18.840	8.745	0.053	0.118
100	28.61	15.33	1.723×10^{-1}	3.346×10^{-1}	28.778	15.661	0.035	0.064
110	45.39	23.03	1.917×10^{-1}	7.233×10^{-1}	45.578	23.520	0.022	0.043
120	73.20	31.33	2.181×10^{-1}	1.116	73.417	31.934	0.014	0.031
130	91.59	41.30	2.454×10^{-1}	1.895	91.833	42.028	0.011	0.024

It was observed from Table 4.9 that when a diffuser was used, the mass transfer resistance in the gas phase was reduced greatly. It was also observed from Table 4.9 that over 95% overall mass transfer resistance is from the gas phase, which indicates that the mass transfer of SO_2 into the slurry is gas-film controlled. The total mass transfer resistance for both phases was also reduced in the experimental temperature range. The results indicate that the reaction of SO_2 with ClO_3^- is mass transfer controlled.

In a reaction system where mass transfer also takes place, a dimensionless number, the Damköhler number is usually used to determine the effect of mass transfer on the chemical reaction. Damköhler number is defined as the ratio of the chemical reaction

rate to the mass transfer rate [21]. The chemical reaction rate of SO_2 with ClO_3^- can

be presented as

$$r_{SO_2} = kC_{SO_2} \tag{32}$$

where k is the SO_2 reaction rate constant described in Table 4.7 and C_{SO_2} is the

concentration of SO_2 in liquid phase. In the reaction of SO_2 with ClO_3^-, mass transfer

is gas film controlled, therefore, the mass transfer rate can be presented as

$$N_A = K_G \Delta p_{SO_2} \tag{33}$$

where N_A is the mass transfer rate, K_G is the overall mass transfer coefficient

calculated in Table 4.9 and p_{SO_2} is the driving force of SO_2 absorption as defined in

Eq.(29).

Damköhler number can then be determined by the following equation

$$D_a = \frac{kC_{SO_2,0}{}^2}{K_G \Delta p_{SO_2}} \tag{34}$$

Damköhler number at different temperatures is listed in Table 4.10.

Table 4. 11   Damköhler number at different temperatures

Temp. ºC	70	80	90	100	110	120	130
D_a no diffuser	1.227×10^4	2.005×10^4	5.909×10^4	11.110×10^4	16.979×10^4	23.267×10^4	22.347×10^4
D_a with diffuser	33.192×10^5	25.437×10^5	20.103×10^5	15.453×10^5	12.014×10^5	9.525×10^5	6.682×10^5
D_a with diffuser/D_a no diffuser	270.451	126.885	33.870	13.910	7.075	4.094	2.990

It was observed from Table 4.10 that the Damköhler number at each reaction

temperature for both diffusing methods is at least in the order of 10^4, which indicates

that the global rate of SO_2 absorption is dominated by mass transfer [21]. The

Damköhler number with diffuser is higher than that without diffuser at each

temperature. It was also noted that using a diffuser increased the overall mass transfer

coefficient in Table 4.9. Therefore, a diffuser in the reaction system cannot only

enhance mass transfer procedure of SO_2 adsorption, but also increase the reaction rate. The ratio of D_a with diffuser to D_a without diffuser indicates that the adsorption procedure of SO_2 with ClO_3^- is not favored by higher temperatures.

Since the reaction of SO_2 with ClO_3^- can be considered as an instantaneous irreversible reaction, the SO_2 diffusion in a homogeneous chemical reaction system, mass balance on SO_2 over a thickness x of the aqueous phase can be expressed in Eq. (32). The mass transfer model of SO_2 and ClO_3^- in a single gas bubble is shown in Fig. 4.8 and can be described as follows:
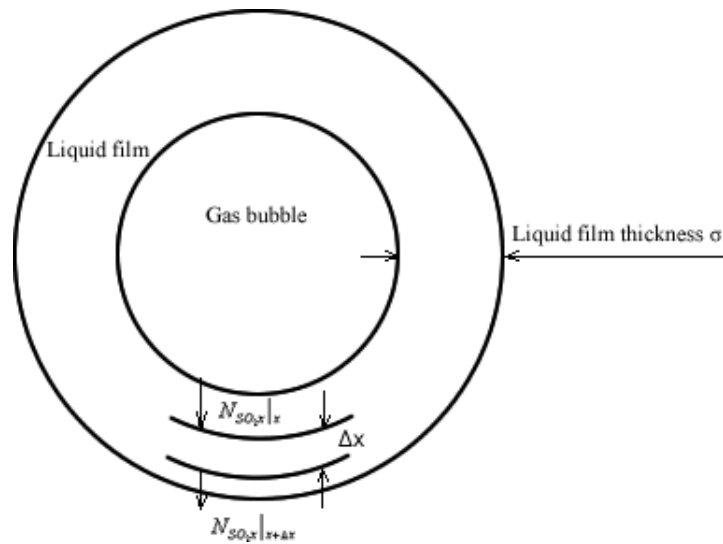
Fig.4. 8 Absorption of SO_2 gas bubble by ClO_3^- with a homogeneous reaction in the liquid phase

$$\frac{dN_{SO_2x}}{dx} + k'C_{SO_2} = 0 \tag{35}$$

where N_{SO_2} represents the molar flux of SO_2 at the position of x. Assume the dissolved SO_2 undergoes a first order reaction with ClO_3^-, and k' is the reaction rate for the reaction of SO_2 with ClO_3^-. Since the SO_2 concentration is low in the liquid phase, the flux of SO_2 can be written as below [14]

$$N_{SO_2,x} = -D\frac{dC_{SO_2}}{dx} \tag{36}$$

where D is the diffusion coefficient of SO_2 in liquid phase.

The absorption of SO_2 with ClO_3^- could be expressed by substituting Eq. (35) into Eq. (36), leading to the following differential equation

$$D\frac{d^2C_{SO_2}}{dx^2} - k.C_{SO_2} = 0 \tag{37}$$

When a stirrer and the diffuser are applied in the system, the gas-absorption process could be semi-quantified with the following reasonable assumptions. Gas bubbles are evenly distributed into the system, and each gas bubble is surrounded by a stagnant liquid film, as depicted in Fig. 8. A semi-steady concentration profile in the liquid film is quickly established after the gas bubbles are formed. The concentration of SO_2 outside the stagnant liquid film changes slowly and is considered constant, $C_{SO_2, \sigma}$.

Based on the assumptions mentioned above, the boundary conditions can be described below

B.C.1: at $x=0$, $C_{SO_2}=C_{SO_2,0}$ (38-a)

B.C.2: at $x=\sigma$, $C_{SO_2}=C_{SO_2, \sigma}$ (38-b)

With these boundary conditions, Eq. (37) can be solved:

$$\frac{C_{SO_2}}{C_{SO_2,0}} = \frac{\sinh\alpha\cosh\alpha\beta + (A-\cosh\alpha)\sinh\alpha\beta}{\sinh\alpha} \tag{39}$$

where α is a dimensionless group $\sqrt{k'\sigma^2/D}$, and β is a dimensionless length, x/σ. A is $C_{SO_2, \sigma}/C_{SO_2,0}$, a constant which can be solved by analyzing the mass balance at $x=\sigma$. Since the concentration of SO_2, $C_{SO_2, \sigma}$ is considered at constant, the amount of SO_2

entering the bulk liquid at $x=\sigma$ over the entire bubble surface is equal to the amount of

SO_2 consumed in the bulk liquid.

$$-SD\frac{dC_{SO_2}}{dx}\Big|_{x=\sigma} = Vk'C_{SO_2,\sigma} \tag{40}$$

where V is the total volume of liquid phase. Therefore, the constant A in Eq. (39) can

be solved by substituting Eq. (40) into Eq. (39).

$$A = \frac{1}{\cosh\alpha + (V/S\sigma)\alpha\sinh\alpha} \tag{41}$$

Since the value of α is very large, A is very nearly zero. Therefore, Eq. (39) can be

simplified to

$$\frac{C_{SO_2}}{C_{SO_2,0}} = \frac{\sinh\alpha\cosh\alpha\beta - \cosh\alpha\sinh\alpha\beta}{\cosh\alpha} \tag{42}$$

For large values of α, $C_{SO_2}/C_{SO_2,0}$ increases with σ, which indicates that the amount

of SO_2 reacts with ClO_3^- in the liquid film increases. Therefore, the untreated SO_2 in

gas phase decreases, resulting in an improvement in SO_2 removal efficiency. The

experimental results of SO_2 absorption showed that the stirrer and diffuser helped in

improving SO_2 removal efficiency, indicating that the system is mass transfer

controlled. This result also indicates that lower initial SO_2 concentration will result in

higher removal efficiency.

4.6 CONCLUSIONS

The reaction kinetics for Fe_2O_3 and Al_2O_3 in fly ash under different reaction

conditions including reaction temperatures, reaction time, and particle size was

successfully derived. The model established shows that Fe_2O_3 and Al_2O_3 have the

same reaction orders at the same reaction temperature. For unground fly ash, the reaction order of Fe_2O_3 or Al_2O_3 is 1.5 and for ground fly ash, the reaction order of Fe_2O_3 or Al_2O_3 is 1.1. Grinding increased the availability of Fe_2O_3 and Al_2O_3, especially the latter in the reaction system, which results in a higher reaction rate constant of the ground fly ash. Grinding of fly ash results in smaller particle size and higher surface area, which increased the reaction rate. At the same reaction temperature, the reaction rate constant for Fe_2O_3 is higher than that of Al_2O_3, and the activation energy in Arrhenius expression for Fe_2O_3 is greater than that of the reaction of Al_2O_3. Therefore, reaction temperature has a larger impact on the extraction of Al_2O_3 from fly ash than that of Fe_2O_3.

The mass transfer coefficient of SO_2 absorption and dimensionless number D_a describing the ratio of the chemical reaction rate to the mass transfer rate were evaluated. The results show that the absorption procedure of SO_2 with the reaction system is mass transfer controlled. Semi-quantification of SO_2 absorption indicates that proper stirring and diffusing of the gas bubbles can enhance SO_2 mass transfer.

4.7 ACKNOWLEDGEMENT

4.8 REFERENCES

1. WHO Regional Office of Europe, Air Quality Guidelines, 2000.

2. National Air Pollution Control Administration, Air quality criteria for sulfur oxides, Washington D.C. 1970.

3. M. Fan, R.C. Brown, S.W. Sung, Y. Zhuang, A process for synthesizing polymeric ferric sulfate using sulfur dioxide from coal combustion, Proceedings - Annual International Pittsburgh Coal Conference 17th. (2000), 2222-2229.

4. A.D. Butler, M. Fan, R.C. Brown, A.T. Cooper, J.(H) van Leeuwen, S. Sung, Absorption of dilute SO_2 gas stream with conversion to polymeric ferric sulfate for use in water treatment, Chem. Eng. J. 98(2004), 265-273.

5. American Coal Ash Association (ACAA), Fly ash facts for highway engineers, 2003.

6. M. Fan, S. Sung, R.C. Brown, T.D. Wheelock, F.C. Laabs, Synthesis, characterization, and coagulation of polymeric ferric sulfate, J. Environ. Eng. (2002) 483-490.

7. M. Fan, R.C. Brown, Y. Zhuang, A.T. Cooper, M. Nomura, Reaction kinetics for a novel flue gas cleaning technology, Environ. Sci. Technol. 37(2003) 1404-1407.

8. M. Fan, R.C. Brown, T.D. Wheelock, A.T. Cooper, M. Nomura, Y. Zhuang, Production of a complex coagulant from fly ash, Chem. Eng. J. 106 (2005) 269-277.

9. M. Fan, R.C. Brown, J.(H) van Leeuwen, M, Nomura, Y. Zhuang, The kinetics of producing sulfate based complex coagulant form fly ash, Chem. Eng. Process. 42 (2003) 1019-1025.

10. R. Mohapatra, J.R. Rao, Review: Some aspects of characterization, utilization, and environmental effects of fly ash, J. Chem. Technol. Biotechnol. 76 (2001) 9-26.

11. R.D. Myers, M. Ghosh, J. B. MacLeod, M. K. Bridle, Integrated water treatment and flue gas desulfurization process, 2006, United States Patent 7037434.

12. S.M. Walas, Chemical Reaction Engineering Handbook of Solved Problems, Gordon and Breach Publishers, Amsterdam, 1995.

13. O.O. Levenspiel, Chemical Reaction Engineering, 3rd Edition, John Wiley & Sons, Inc., New York, 1999.

14. R. B. Bird, W. E. Stewart, E. N. Lightfoot, Transport Phenomena, 2nd Edition, John Wiley & Sons, Inc., New York, 2002.

15. S. Olausson, M. Wallin, I. Bjerle, A model for the absorption of sulphur dioxide into a limestone slurry, Chem. Eng. J. 51 (1993) 99-108.

16. A. Lancia, D. Musmarra, F. Pepe, Modeling of SO_2 absorption into limestone suspensions, Ind. Eng. Chem. Res. 36 (1997) 197-293.

17. O. O. Levenspiel, The Chemical Reaction Omnibook, Oregon State University

Bookstores, Corvallis, Oregon, 1996.

18. C. Chen, M. Zeng, G. Liu, C. Chai, Y. Yao, B. Liu, Chemical Engineering Principles, Tianjin Science and Technology Publishers, Tianjin, 1993.

19. P. Byrne, Mathematical modeling and experimental simulation of chlorate and chlor-alkali cells, Doctorial thesis, Chemical and Engineering and Technology, KTH, Stockholm, 2001.

20. R. Atkinson, D.L. Baulch, R.A. Cox, J.N. Crowley, R.F. Hampson, R.G. Hynes, M.E. Jenkin, M.J. Rossi, J. Troe, Evaluated kinetic and photochemical data for atmospheric chemistry: Volume I - gas phase reactions of O_x, HO_x, NO_x and SO_x species, Atmos. Chem. Phys. 4(2004) 1461 – 1738.

21. V. Inglezakis, S. Poulopoulos, Adsorption, Ion Exchange and Catalysis: Design of Operations and Environmental Applications, 1st edition, Elsevier Science & Technology Books, 2006.

CHAPTER 5 CONCLUSIONS

5.1 GENERAL CONCLUSIONS AND RECOMMENDATIONS

The procedure and reaction kinetics of producing a complex coagulant from fly ash with concomitant flue gas scrubbing was investigated. The reaction of fly ash with sulfuric acid successfully converted Fe_2O_3 and Al_2O_3 in fly ash to Fe^{3+} and Al^{3+}, which formed polymeric ferric sulfate (PFS) and polymeric aluminum sulfate (PAS) due to a series reactions. At the same time, SO_2 was removed by the added sodium chlorate in the fly ash slurry. Reaction temperature, gas dispersing methods, and the concentration of SO_2 in feed play important roles in SO_2 removal. The produced complex coagulant was effective in removing total suspended solids (TSS) and turbidity. pH value plays an important role in the coagulant performances. For TSS and turbidity removal, the produced complex coagulant favors a neutral to slight alkaline pH value. The complex coagulant performed better in turbidity removal than conventional iron or aluminum sulfate coagulant at low concentrations.

The reaction order of Fe_2O_3 or Al_2O_3 with sulfuric acid is the same at the same temperature. The reaction order of each compound for the unground fly ash is 1.5 and for the ground fly ash is 1.1. Investigation of Arrhenius expressions for both unground and ground fly ash found that the activation energy for Fe_2O_3 is higher than that of Al_2O_3, therefore, temperature has greater impact on the reaction of Al_2O_3 in fly ash. A semi-quantified analysis shows that the reaction of SO_2 with ClO_3^- in the fly ash

slurry is mass transfer controlled and that a proper stirring and diffusing of the gas bubbles can enhance the mass transfer of SO_2 in the reaction with ClO_3^- in the fly ash slurry.

5.2 RECOMMENDATIONS ON FUTURE INVESTIGATIONS

This research provides a possible utilization of fly ash in the production of an effective complex coagulant with the removal of SO_2 in flue gas. However, there are still some possible concerns of this procedure.

a) The produced waste. Although over 70% of Fe_2O_3 and 40% of Al_2O_3 can be extracted from the fly ash, the inactive silicate and aluminosilicate still amount over 50%. However, the silicate and aluminosilicate materials could react with calcium hydroxide at ordinary temperatures to produce cementitious compounds in the presence of water if the physical and chemical properties meet the requirement. Therefore, future research on utilizing the inactive silicate and aluminosilicate slurry is necessary.

b) The oxidant. Sodium chlorate was added as the oxidant in this study. Although sodium chlorate is effective in oxidizing SO_2, it is a non-selective herbicide. If residual sodium chlorate is discharged into the environment, it may impose harmful impacts on various plants. Therefore, a strict control of sodium chlorate discharge or finding an alternative oxidant is also important.

APPENDIX

Synthesis, Properties and Environmental Applications of Nanoscale Iron-Based Materials: A Review

Ling Li[†], Maohong Fan[*], Robert C. Brown[†], J(Hans) van Leeuwen[†], Jianji. Wang , Wenhua Wang ,

Yonghui Song[ℓ], Panyue Zhang[F].

Center for Sustainable Environmental Technology, Iowa State University, Ames, Iowa 50011, USA

Department of Chemistry, Henan Normal University, Xinxiang, Henan 453007, China

School of Environmental Science and Engineering, Shanghai Jiao Tong University, Shanghai 200240, China

Chinese Research Academy of Environmental Sciences, Beijing 100012, China

Sino-German Center for Environmental Technology, Hunan University, Changsha, Hunan 410082, China

* Corresponding author. phone: (515)294-3951; fax: (515)294-3091; E-mail:fan@ameslab.gov

† Iowa State University

‡ Henan Normal University

* Shanghai Jiao Tong University*

ℓ Chinese Research Academy of Environmental Sciences

F Hunan University

ABSTRACT: Due to their special properties, people have been increasingly interested in studying applications of nanoscale metal materials in environmental engineering. Literature about the current research on the synthesis, properties and environmental applications of nanoscale iron-based materials is reviewed and summarized in this paper. Different physical and chemical methods used for synthesizing nano iron-based particles with desired size, structure and surface property are described herein. We also emphasize important properties of nano-iron-based particles, including the density and intrinsic reactivity of surface sites. These properties directly influence the chemical behavior of such particles and, consequently, affect their applications in water and wastewater treatment and in air pollution control. Environmental applications of nano-iron particles are discussed in detail, including removal of chlorinated organics, heavy metals, and inorganics.

KEY WORDS: nanoparticle; properties; environmental applications.

A.1. INTRODUCTION

Nanoscale metal materials refer to metals with nanoscale particle size and structures, typically in the range of 1 to 100 nm. Recent research has shown that many of these materials' properties depend upon particle size in the nanoscale regime[25]. Moreover, structure of nanomaterials also results in the novel and significant changes in physical and chemical properties: e.g. coercive force in magnetic materials can be changed[4, 5, 32, 52, 66], surface reactivity and catalytic capability can be enhanced[25, 43], and mechanical strengths can be increased by a factor of 5 or more[25]. Among structural issues, the surface effects of nanoparticles are extremely important. For example, the surface chemistry of crystallites pushed down to the nanoscale range can differ from microscale particles and their unique reaction chemistry can be observed. Also, their huge specific surface area allows nanoparticles to be considered as surface-produced on the macroscale, thus affecting their bulk properties[25]. For certain spherical nanoparticles in the range of 3 nm, about 50% of the atoms or ions are on the surface, allowing both the possibility of manipulating of bulk properties by surface effects and near-stoichiometric chemical reactions[25]. In most cases, failure occurs on the surfaces of materials. Therefore, optimization of surface structure may effectively improve the overall behavior of the nanoparticles.

In environmental applications, nano-based iron materials are turning out to be remarkably effective tools for cleaning up contaminated soil and groundwater. Because of their smaller size, nano-based iron materials are much more reactive than conventional iron powders, and they can be suspended in slurry and pumped straight to the contaminated site easily. Elemental iron itself has no known toxic effect, considering it is one of the most abundant metals on Earth. When exposed to air, elemental iron oxidizes to brick-red iron oxide. When metallic iron oxidizes in the presence of organic contaminants, such as trichloroethane (TCA), trichloroethene (TCE), tetrachloroethene (PCE), or carbon tetrachloride, these organic components can be broken down into simple carbon compounds that are less toxic. Moreover, oxidizing iron can reduce heavy metals such as lead, nickel or mercury, to an insoluble form that tends to stay locked in soil. Accordingly, this article will elaborate on the preparation, properties, and environmental applications of nanoscale iron-based materials.

A.2. SYNTHESIS OF NANOSCALE IRON-BASED MATERIALS

The methods of preparation are determining factors in producing different sizes and shapes of nanoscale particles. Researchers have recently developed different synthesis methods that can be classified into two categories: i.e., either a physical or a chemical synthesis method.

A.2.1 Physical Synthesis Methods

A.2.1.1 Inert Gas Condensation

Inert gas condensation (IGC) has been accepted by many researchers[8, 40, 41, 62]. Gleiter[18] was the first to synthesize nanoscale iron particles through IGC. Sanchez-Lopez et al.[47] successfully prepared nanoscale iron particles with an average diameter of 17 nm using IGC. Nakayama et al.[41] prepared nanoscale iron oxide powder using IGC combined with co-evaporation, in-situ oxidation and in-situ compaction techniques, and produced particles with average size between 8 and 28 nm.

A.2.1.2 Severe Plastic Deformation

Studies of the severe plastic deformation (SPD) of metals were initiated by Bridgman in 1952[56]. SPD methods provide significant deformations at relatively low temperatures under the high pressures employed. Such conditions can result in significant refinement of microstructure or nanostructure, including ultra-fine-grained structures containing mostly high-angle grain boundaries[60].

A. 2.1.3 High-Energy Ball Milling

High-energy ball milling uses conventional mechanical grinding techniques to break coarse metal grains into micro- or nano-scale particles. The continual ball-particle collision can break the size of individual grains down to only a few nanometers and result in the repeated deformation, fracture, and welding of the particles. Australia's Advanced Powder Technology Pty. Ltd. has successfully commercialized a wide range of nanopowders by ball milling[12]. Del Bianco et al.[13] achieved 10 nm iron particles by ball milling. Malow et al.[35] compacted nanocrystalline iron produced by ball milling into samples nearing full density, realizing iron particles between 15 and 24 nm at an isothermal annealing temperature of 800 K.

A.2.1.4 Ultrasound Shot Peening

Ultrasound shot peening (USSP) was developed by Tao et al.[57] using high-frequency (20 kHz) ultrasonic equipment and an industrial-pure iron plate as the sample. The USSP process delivers repeated mechanical loads at high speeds in random directions onto the sample surface, generating grain dislocations. Further USSP treatment will recombine or rearrange these dislocations, inducing changes in the relative positions of the grains. Such a refinement process may result in the formation of ultrafine grains, depending on load intensity and strain rate. The transmission electron microscopy (TEM) results of Tao showed that the initially coarse grain structure in the surface layer was refined to ultrafine grains with an average size of 10 nm. TEM graphs indicated that the grains were mostly uniform and equiaxed.

A.2.2 Chemical Synthesis Methods

A.2.2.1 Reverse Micelle (or Microemulsion)

Reverse micelle synthesis offers an excellent method for preparing nanoparticles with a very narrow size distribution and highly uniform morphology [4, 64]. Carpenter[4] used a reverse micelle system of cetyltrimethyl ammonium bromide, octane, n-butanol, and aqueous reactants to reduce ferrous sulfate ($FeSO_4$) by sodium borohydride ($NaBH_4$). By coating a thin layer of gold, the nano-iron particles were protected from oxidation. The resulting nanoparticles were 7 nm in diameter coated with a 1 nm gold shell. Li et al.[26] used a similar system and achieved nearly spherical nanoscale iron particles with diameter of less than 10 nm. Further research by Wiggins et al.[64] on Fe- Au nanoparticles showed that nanoparticles with a 3 nm Au core, a 1 nm Fe layer, and a 2 nm Au coating were obtained using the reverse micelle method. Song et al.[54] used a system of sodium dodecyl benzene sulfonate, styrene, benzene, ammonium peroxydisulfate, ethanol, ferrous sulfate, and hydrochloric acid to prepare nanoscale α-Fe_2O_3. The resulting particles had an average diameter of about 10 nm and uniform size distribution.

A.2.2.2 Controlled Chemical Coprecipitation

In controlled chemical coprecipitation procedure, an appropriate precipitator is added to the solution and pH value is controlled within a proper range. Nanoscale particles can then be obtained by aging, filtering, washing, drying, and decomposing the resulting ultra-fine precursor. Commonly used precipitators include $NaHCO_3$, Na_2CO_3, $(NH_4)_2CO_3$, NaOH and ammonia. Liu et al.[32] used controlled chemical coprecipitation to prepare nanoscale iron oxide particles with an average size less than 5 nm. In preparing nanoscale Fe_3O_4 particles, Jiang et al.[20] added urea into the NH_4OH base solution to manipulate the pH of a ferrite solution. The average diameter of synthesized Fe_3O_4 particles can be adjusted from 8 to 50 nm by controlling the amount of urea decomposing in the ferrite solution. Kim et al.[24] reported successful preparation of non-ionic surfactant coated nanoscale Fe_3O_4 particles with an average size of 2-6 nm.

A.2.2.3 Chemical Vapor Condensation

Because a wide range of precursors is commercially available[63], the chemical vapor condensation (CVC) process was developed for preparing a variety of materials. Choi et al.[10] reported that magnetic nanoparticles of Fe were synthesized by CVC using the precursors of iron carbonyl ($Fe(CO)_5$) as the source under a flowing helium atmosphere. They realized spherical nanoparticles with an average size of 5 to 13 nm and uniform distribution.

A.2.2.4 Pulse Electrodeposition

Recent research has also reported that nanoscale iron-based materials can be prepared successfully by pulse electrodeposition PED[42]. Natter et al.[42] used a Fe anode and an inert Ti cathode to prepare nano-Fe. The electrolyte (citrate bath) contained 50 g/L $(NH_4)_2Fe(SO_4)_2$, 20 g/L citric acid trisodium salt, 10 g/L citric acid, and 40 g/L boric acid. The bath temperature was 303 K. A current with short pulse widths was applied to control grain size. Results showed that the nanoscale iron particles as prepared had an average size of 19 nm and thermal stability up to 550 K.

A.2.2.5 Liquid Flame Spray

One of the advantages of liquid flame spray (LFS) is that almost any element that can be fed in the form of liquid can be used to form nanoparticles. Makela et al.[34] reported the preparation of nanoscale Fe, Pd and Ag by LFS. Their results showed that the average particle size of the three metals was in the range of 10-50 nm (e.g. a 40 nm particle size for nano-iron). Standard deviation of the generated size distributions was within 1.35-1.5.

A.2.2.6 Liquid Phase Reduction

The basic idea of liquid phase reduction (also called borohydride reduction) is to add a strong reductant into a metallic ion solution to reduce it to nanoscale metal particles. This method was accepted by Glavee et al.[17] as early as 1995 to prepare nanoscale iron particles. The nano-iron particles synthesized by this method are referred to as Fe^{BH} in this paper. Because its simplicity and productivity, iron nanoparticles synthesized by liquid phase reduction have been the most thoroughly investigated and one of the most widely used in environmental applications. The most commonly used reductant is $NaBH_4$. Successful use of both ferric chloride ($FeCl_3 \cdot 6H_2O$) and ferrous sulfate ($FeSO_4 \cdot 7H_2O$) as the aqueous phase iron solution has been reported [9, 15, 22, 31, 67]. Nurmi et al[43] and Liu et al[31] investigated the structure and characteristic of nano-iron particles synthesized by this method. The two authors reached the same conclusion regarding particle size, but the specific surface area calculated by Nurmi was lower than that by Liu and that had been previously reported[22, 46]. And many other authors investigating nano-iron particles by liquid phase reduction reached similar results regarding particle size and specific surface area. Zhang[67] reported that nanoparticles produced by their method had an average particle size of 60.2 nm. Most particles (>80%) had diameters less than 100nm, with 30% less than 50 nm. The average specific surface area of the particles was about 35 m^2/g. The results of Choe et al.[9] showed particle size in the range of 1-100nm and specific surface area of 31.4 m^2/g. Nanoparticles obtained by Kanel et al.[22] ranged from 10-100nm, with a specific surface area of 24.4-37.2 m^2/g.

Ponder et al. [45, 46] developed a supported resin or silica-gel zerovalent iron nanoparticles by borohydride reduction. These materials ("ferregals") have been proven to be effective in decreasing heavy metal contaminants. The synthesized resin supported particles had an average size of 10-30 nm and specific surface area of

24.4 ± 1.5 m^2/g. The specific surface areas of the unsupported nano-iron by borohydride reduction and the resin supported were additive to give the specific surface area of resin-supported ferregal. While the silica gel-supported ferregal had a specific surface area one order of magnitude higher. Ponder et al.[45] also reported that decreasing the size of the nano-iron particles and dispersing them on the support increased the specific surface area, as well as the ratio of surface to bulk iron atoms, and should thereby increase both the reaction rate and the fraction of iron atoms available for the reaction.

A.2.2.7 Gas Phase Reduction

A commercial iron nanoparticle product known as RNIP (Toda Kogyo Corp., Schaumberg, IL) is widely used in environmental applications synthesized by gas phase reduction. RNIP (referred to Fe^{H2} by Nurmi et al.[43], we also use this symbol here) is produced by heat-reducing goethite or hematite particles with H$_2$ at high temperature (350-600 ^{o}C). After cooling and transferring the iron particles into water in a gas phase, a surface oxidation shell is formed on the particle surface in water. After dried, the iron nanoparticles are ready for the reduction of organohalogen compounds and/or heavy metals[59]. RNIP is known to be two phase material consisting of Fe$_3$O$_4$ and α-Fe^0. The obtained particles have an average particle size of 50-300 nm and specific surface area of 7-55 m^2/g. An Fe content is usually no less than 65% by weight.

A.3. PROPERTIES

A.3.1 Core-Shell Structure

Core-shell, a structure typical of iron nanoparticles, plays an important role in environmental remediation[31]. It is assumed that the reactivity of core-shell nanoparticles is driven by oxidation of the Fe^0 core[31, 43]. Due to their ultra-fine size and high specific surface area, zero-valent iron nanoparticles can be easily oxidized in air. Because oxidation strongly depends on particle size[32], many researchers using ultra-fine particles apply a passivated layer consisting of an oxide or a stable noble metal shell to protect iron nanoparticles from oxidation[4, 43]. The commercial available iron nanoparticle, Fe^{H2} also has an oxide shell formed from controlled exposure of Fe^0 in water[59]. Other researchers using iron oxide nanoparticles apply stable noble metal, metal oxide, organic material, or polymer to increase particle properties[6, 55, 58].

Nurmi et al.[43] investigated the structure of Fe^{H2} and Fe^{BH} (prepared by borohydride reduction), the two types of iron nanoparticles widely used in environmental remediation. X-ray Diffraction (XRD) patterns on the as-received Fe^{H2} indicated two phases, α-Fe^0 and Fe$_3$O$_4$ with the metal-to-oxide proportion of 70 to 30%. This agrees well with the manufacturer's description[59] and the analysis by Liu et al.[31]. The mean crystalline size for Fe^0 was ~30 nm, while that for Fe$_3$O$_4$ was ~60 nm. In contrast,

mean crystalline size for Fe^0 in Fe^{BH} was <1.5 nm. And Fe^{BH} had a much higher initial Fe^0 content (97±8%)[31].

The TEM data of Fe^{H2} and Fe^{BH} are shown in Figures A.1 and A,2. The TEM data (Figure A.1) show that as received Fe^{H2} is composed of aggregates of faceted plates and smaller irregular particles. The small irregular particles consist of a nearly single-crystal Fe^0 core with a polycrystalline oxide shell. The TEM images of Fe^{BH} appear similar to one another (Figure A.2). The material is comprised of <1.5 nm crystals that are aggregated into approximately spherical 20-100 nm diameter particles which are further aggregated into the chains shown in Figure A.2A. The cores are made of either very small grains or are amorphous, and the shells are apparently amorphous.

FIGURE A.1. TEMs of Fe^{H2}. (A) Low magnification image of as-received sample. (B) Higher resolution image of irregularly shaped metal particle. (C) Higher resolution image of oxide shell around metal particle. (D) Low resolution image of flash-dried sample[43].

X-ray photoelectron spectroscopy (XPS) data showed that the Fe^{H2} surfaces are made of mostly Fe and O with small amount of S and some other elements, like, Na and Ca[43]. No borate or boride was observed in Fe^{H2} samples. The manufacturer claims that the reduced sulfur plays an important role in the reactivity[59]. In contrast, Fe^{BH} surfaces contain less S and more B. XPS data showed that B on Fe^{BH} surfaces was mostly borate with some boride. The boron content could affect the particle properties and reactivity[31].

The electron holography of iron nanoparticles by Signoretti et al.[52] showed similar results. The individual particle has a core-shell structure, with several particles (5 in the sample) aggregated into chain structure (Figures A.2-4). Other references also showed that the prepared nanoparticles aggregated into chain or floc structure [19, 23, 26, 32, 63, 67]. Aggregation of nanoparticles is difficult to avoid under environmental conditions. One consequence of aggregation is that the specific surface area of highly aggregated nanoparticles is likely to be very different from the specific surface area measured on dispersed nanoparticles. This issue is especially important with respect

to the determination of reactive surface area and reactive sites on the particle surface. And aggregation of nano-iron particles prevents their flow through porous media such as soil[49], which may result in their transport in contaminated sites decreased. Summaries of particle size and structure are listed in Table A.1.
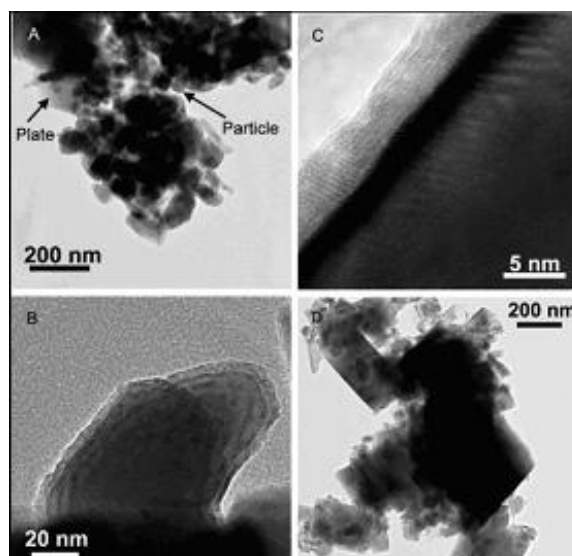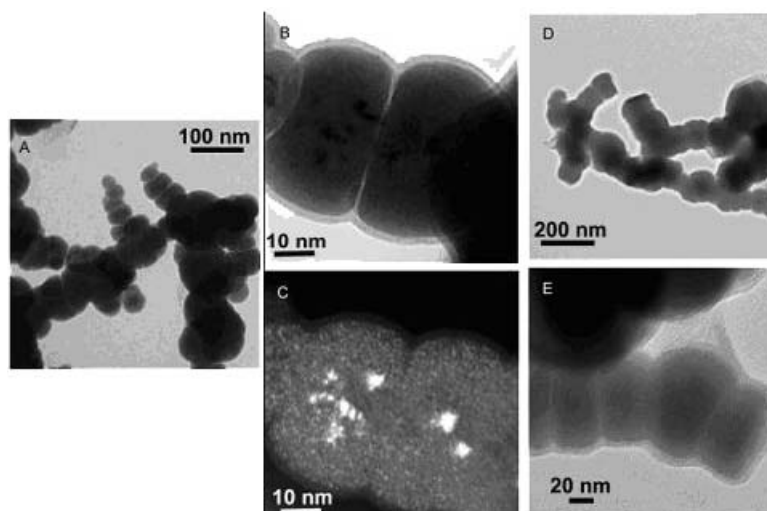

FIGURE A.2. TEMs of Fe[BH]. (A) Low magnification image of as-received sample. (B) Higher resolution image of metal particle. (C) Dark field image of metal particle highlighting small metal crystallites in particle. (D) Low resolution image of flash-dried sample. (E) Higher resolution image of flash-dried sample showing spreading of coating layer between particles[43].
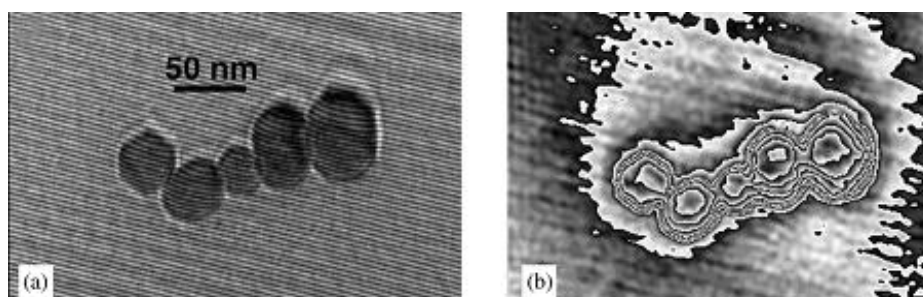
FIGURE A.3. (A) Hologram of a nanoparticle chain; (B) phase contour map (modulo 2p=6) extracted from the hologram in (A) [52]
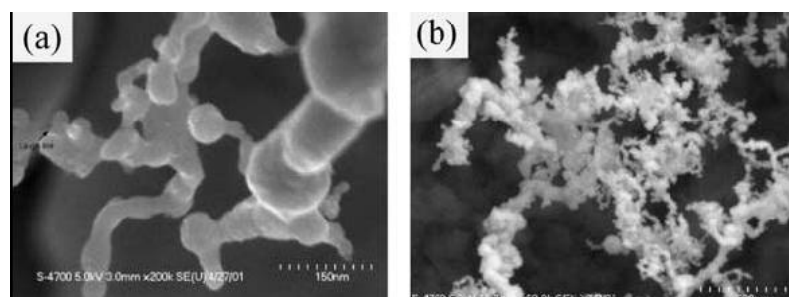
FIGURE A.4. FESEM images of the Fe nanoparticle: individual nanoparticles in (A), and aggregated particles in (B)[23].

TABLE A.1. Summary of physical properties obtained by different researchers

sample	Ref. No.	TEM particle size (nm)	Shell thickness (nm)	TEM structure	remark
Fe^{H2}	43	38	~3.4	irregular Fe^0 core + oxide shell*	gas phase reduction; as-received
Fe^{H2}	43	44	>3.4	irregular Fe^0 core + oxide shell*	gas phase reduction; flash-dried
Fe^{BH}	43	59	~2.3	▪ small crystallites < 1.5 nm ▪ 20-100 nm spherical aggregates with an amorphous coating ▪ chains of 20-100 nm particles	borohydride reduction; as-received
Fe^{BH}	43	67	~3.2	as above	borohydride reduction; flash-dried
Fe/Au	4	7	1	Fe core + gold shell	reverse micelles
Au/Fe/Au	64	8	1Fe, 2 Au	Fe layer+ Au coating	reverse micelles
Fe_2O_3	54	20-40	N/A	Fe_2O_3 core + thin polystyrene shell	reverse micelles
Fe_3O_4	24	2-6	1-2	Fe_3O_4 core +nonionic surfactant layer	controlled chemical coprecipitation
Fe/Co	63	12-18	3-4	Fe+Co metallic core and oxide shell	chemical vapor condensation
Fe	3	11.5	2.7	Fe core + oxide shell*	reverse micelles
Fe/Gd	50	20	~5	Fe/Gd + B_2O_3/H_3BO_3 shell	arc-discharge
Fe	45	10-30	N/A	Fe core + oxide shell*	85% Fe^0
Fe	2	200	10-20	Fe core+ carbon layer	1-3 min annealing, 300-800°C
Fe	1	13±2	2-4	Fe core +oxide shell *	inert gas condensation
Fe	33	30-50	N/A	Fe core + oxide shell *	as prepared
Fe	53	7-21	2-3	-Fe core + oxide shell *	inert gas condensation

*It has been reported that the oxide layer generally formed on iron is either γ-Fe_2O_3 or Fe_3O_4[1, 53].

A.3.2 Specific Surface Area

As with particle size, core-shell structure, and composition, specific surface area is also an important factor affecting the chemical and physical properties of

nanoparticles. Nanoparticles have been proven to have relatively large specific surface area, determined by certain researchers using BET measurement. Recent research has shown that nano-iron particles have greater rates of reaction with contaminants, thus making them more effective in reducing certain kinds of contaminants. Surface properties are summarized in Table A.2.

TABLE A.2. Summary of shape and surface properties

Sample	Ref. No.	BET specific surface area (m^2/g)	Shape	Remark
Fe	52	N/A	not spherical	as-prepared
Fe^{H2}	43	29	irregular	as-received
Fe^{BH}	43	33.5	irregular	as-received
Fe	61	33.5	not spherical	borohydride reduction
Pd/Fe	67,30	35±2.7	roughly spherical	borohydride reduction
Fe	9	31.4	N/A	borohydride reduction
Fe	22	24.4(unreacted) 37.2 (corroded)	amorphous	borohydride reduction
Fe	46	24.4±1.5(ferregal) 21.7±1.5(unsupported)	N/A	borohydride reduction
Fe	23	13.87 and 15.08 for 2 samples	irregular	hard sphere model and $7.87g/m^3$ for Fe
Fe	45	24.4±1.5(supported) 21.7±1.5(unsupported)	irregular	85% Fe^0
Fe	68	33.9	N/A	N/A
Fe/Ag	65	35	irregular	iron core + silver shell
Fe	48	18	N/A	83% Fe^0
Ni/Fe	48	59	not spherical	53.1% Fe^0,15.6% Ni

Table A.2 shows us that the specific surface areas of nanoscale metal particles are fairly high. Zhang et al.[68] compared the surface areas of nanoscale metal particles with those of commercially available microscale metal particles, and concluded that the surface areas of the former one were 1-2 orders higher. Such a large specific area provides more sites where reaction occurs, which is one reason why nanoscale iron particles might exhibit greater rates of reaction with contaminants[43, 67]. Also, these huge surface areas allow the nanoscale iron particles to be viewed as surfaces produced on a macroscale level[25]. Other possible reasons why nanoscale iron particles might exhibit enhanced reactivity include higher density of reactive surface sites and greater intrinsic reactivity of surface sites[43].

A.3.3 Magnetic Properties of Nanoscale Iron

Magnetic properties of nano-iron particles play an important role in magnetic recording, magnetic fluids, biomedical applications and catalysis[52]. However, researchers in environmental applications tend to avoid these magnetic properties.

Because with their high surface area and magnetic dipole-dipole attraction, magnetic nanoparticles tend to aggregate[32], resulting in much larger chains and loss of reactivity and transfer of nanoparticles in contaminated sites. Therefore, dispersion of magnetic nanoparticles is a critical factor to improving their efficiency of reaction. He and Zhao[19] applied water-soluble starch to stabilize the Fe-Pd nanoparticles. The starched nanoparticles were presented as discrete particles and displayed much less aggregation. Their results also indicated that the starched nanoparticles had a greater reactivity.
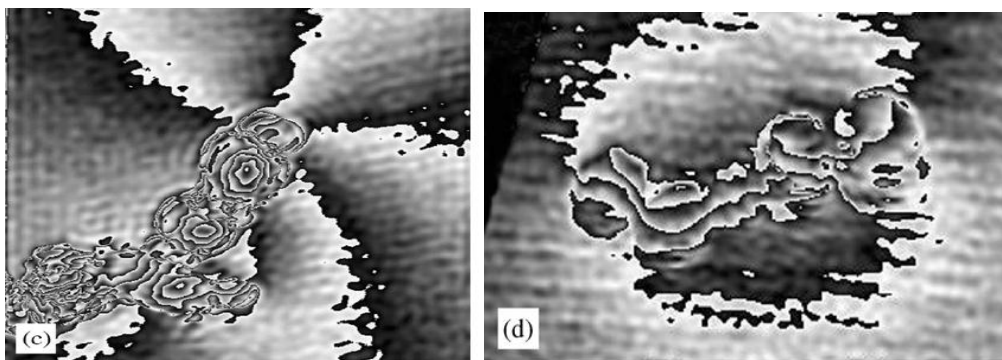
FIGURE A.5. Magnetic phase map of iron nanoparticle chain[52]

A.4. ENVIRONMENTAL APPLICATIONS

As discussed in the third section of this paper, compared with microparticles, nanoscale iron-based particles have higher rates of reactivity due to their high specific surface area and more reactive surface sites. In addition, due to their ability to remain in suspension, nano-iron particles can be injected into contaminated soils, sediments, and aquifers[67]. But because of the aggregation of nanoiron particles, it is difficult to make them stay in suspension stably. Schrick et al[49] demonstrated that carbon support significantly inhibited aggregation and increased transport of the nano-iron particles. Many reports have indicated that nano-iron has been accepted as a versatile tool for the remediation of groundwater, soil, and air on both the experimental and field scales. It has also been reported that nano-iron can effectively react with diverse environmental contaminants, including chlorinated organics[26, 31, 61, 65, 67, 68], heavy metals[14, 22, 45, 46], and inorganics[9, 27]. Examples of common environmental contaminants that can be reduced by nano-iron are listed in Table A.3.

TABLE A.3. Common environmental contaminants that can be transformed by nanoscale iron particles

Chemicals	Types of nanoparticle and corresponding ref.
Chlorinated methanes	
Carbon tetrachloride (CCl_4)	Fe^0 (43, 15), Fe-Pd (15), Fe_2O_3 (36)
Chloroform ($CHCl_3$)	Fe^0 (15) , Fe-Pd (15)
Dichloromethane (CH_2Cl_2)	Fe-Pd (30)
Chloromethane (CH_3Cl)	Fe-Pd (30)
Tetrachloromethane (CCl_4)	Fe-Pd (30)
Chlorinated ethenes	
Tetrachloroethene (C_2Cl_4)	Fe^0 (15), Fe-Pd (15, 68)
Trichloroethene (C_2HCl_3)	Fe^0 (26, 61, 31), Fe-Pd (61, 68), Fe-Ni (48)
cis-Dichloroethene ($C_2H_2Cl_2$)	Fe^0 (15), Fe-Pd (15)
trans-Dichloroethene ($C_2H_2Cl_2$)	Fe-Pd (68)
1,1-Dichloroethene ($C_2H_2Cl_2$)	Fe^0 (15), Fe-Pd (15, 68)
Vinyl chloride (C_2H_3Cl)	Fe^0 (15), Fe-Pd (15, 68, 29)
Polyhalogenated methanes	Fe_2O_3 (44)
Organochloride Pesticides	Fe^0 (67), Fe-Pd (67)
polychlorinated biphenyl	Fe^0 (33,61), Fe-Pd (67, 61)
Heavy metal ions	
Arsenic (As(III), As(V))	Fe^0 (22, 14)
Lead (Pb(II))	supported Fe^0 (46, 45)
Chromium (Cr(VI))	supported Fe^0 (46, 45)
Inorganic anions	
Nitrate (NO^{-3})	Fe^0 (9)
Carbon monoxide (CO)	Fe_2O_3 (27)
Selenate (Se(VI))	Fe^0 (38), Fe-Pd (38)

A.4.1 Degradation of Chlorinated Organic Compounds

A.4.1.1 Application of Nanoscale ZVI

Nano-iron particles can reduce almost all halogenated hydrocarbons to benign compounds such as hydrocarbons, chloride, and water[67, 61]. Experiments by Zhang[67] showed that reductions of trichloroethane (TCA), trichloroethene (TCE) and tetrachloroethene (PCE) by synthesized nano-iron (Fe^{BH}) were highly effective. Ethane was the major product of all the tests. Removal greater than 99% was achieved in 24 hours with nanoscale ZVI. The results of their field-scale pilot test corresponded closely to the laboratory results, with concentrations of TCE, PCE, and DCE reduced by nanoscale ZVI to levels near or below groundwater quality standards within 6 weeks.

Li et al.[26] investigated the degradation of TCE using two types of nano-iron particles. Their results showed that nano-iron is an effective tool for degrading TCE. The time required for complete reduction of TCE was different for different initial TCE concentrations, nano-iron loading and particle sizes (e.g. reduction time proved to be lower with lower initial TCE concentrations, smaller particle sizes, and higher nano-iron loading). Liu et al.[31] used two types of widely used nano-iron particles: synthesized Fe^{BH} and commercially available Fe^{H2} (RNIP) in TCE degradation under conditions of high TCE concentration (limited iron) and low TCE concentration (excess iron). Their results also indicated that faster reduction could be achieved through lower TCE concentrations and smaller particle sizes. According to their calculation, Fe^{H2} displayed pseudo-first-order kinetics under both conditions and Fe^{BH} displayed pseudo-first-order kinetics for excess iron and zero-order kinetics for limited iron. The model-derived rate constant for TCE degradation, K_{TCE} of Fe/B $(1.4 \times 10^{-2} Lm^{-2}h^{-1})$, was one order of magnitude higher than for Fe^{H2} $(3 \times 10^{-3} Lm^{-2}h^{-1})$, and two orders higher than for non-nano ZVI provided by other researchers $(4.96 \times 10^{-4} Lm^{-2}h^{-1}$ [37], $3.9 \pm 3.6 \times 10^{-4} Lm^{-2}h^{-1}$ [21]). The final products of TCE transformation by Fe^{BH} under both conditions were similar: 70-80% ethane and 20-30% C_3-C_6 products. For Fe^{H2}, the primary products were 84.3% acetylene and 7.8% ethene under limited iron conditions and 74.5% ethene and 20.9% ethane under excess iron conditions. Under the conditions of Wang and Zhang[61], TCE was completely dechlorinated within 1.7 hours using their synthesized nanoscale ZVI particles. The final products were identified as hydrocarbons, including ethane, ethene, propane, butane, butene, and pentane.

Lowry et al.[33] investigated the efficiency of dechlorination of dissolved polychlorinated biphenyl (PCBs) by microscale and nanoscale ZVI particles in a water-methanol solution. Based on the product formation, dechlorination rate constants were pseudo-first-order. With commercial microscale iron powders, no PCB dechlorination was observed after 180 days, while the 45-day experiment with nanoscale ZVI indicated that PCB was effectively dechlorinated. Wang and Zhang[61] also investigated the dechlorination of PCBs in an ethanol-water mixture under ambient conditions by nanoscale ZVI. Over a 17-hour experiment, about 25% of total PCB was reduced. The calculated surface-area-normalized rate constant for the synthesized nanoscale ZVI was $3.0 \times 10^{-3} Lh^{-1}m^{-2}$, indicating a pseudo-first-order reaction.

In the dechlorination of tetrachloromethane and trichloromethane, Lien and Zhang[30] found that, in chlorinated organic water solution or mixture, nanoscale ZVI particles were mostly suspended in liquid phase, whereas microscale ZVI usually settled at the bottom of the bottle. Therefore, transport or diffusion of the chlorinated organics to the suspended nanoscale ZVI may have contributed to the faster reaction compared with the microscale ZVI.

A.4.1.2 Application of Bimetallic Nanoscale Iron Particles

Although nanoscale ZVI has been proven to be effective in degrading chlorinated organics, its intrinsic structure may limit its reaction rate. As discussed earlier, nano-iron particles have a core-shell structure with an Fe^0 core and an oxide or a noble metal shell. The decrease of iron reactivity over time is probably due to the formation of surface oxide layers [30, 61], a phenomenon confirmed through the oxygen electron energy-loss spectroscopy test by Liu et al.[31], which indicated that oxygen atoms concentrated in the shells of the particles and oxidized the iron cores. Recent research has found that, because noble metals such as Pd, Ni, or Ag formed on the iron particle surface oxidize less rapidly than Fe^0 (thus preserving the Fe^0 core for chlorinate organics degradation[31]), coating nanoscale ZVI particles with a thin layer of noble metal can greatly increase reactivity[19, 30, 48, 61]. Zhang et al. [30, 61] also found that laboratory-synthesized nano-irons were more reactive than commercially available nano-iron particles. This is likely because, having less surface oxidation and/or surface contamination due to their relative lack of exposure to air, the former form a "fresher" metal surface, enabling the oxide layer to play an important role in the reaction.

Although the exact mechanism of this enhanced reactivity is unknown yet, some researchers offer plausible explanations. When nanoscale ZVI is attached to a noble metal, galvanic cells are formed in the coupled bimetallic particles. Iron serves as the electron donor and, preferably, becomes reacted with the contaminants, whereas the noble metal (cathode) is protected[30, 48]. Also, noble metals such as Pd may further promote dechlorination reactions by their catalytic functions [30, 61]. He and Zhao reported that the degradation of TCE can be greatly enhanced when a small portion of Pd (~0.1% of Fe) was coated on the Fe particles[19]. Zhang et al.[68] found that physically mixing Fe and Pd particles together produced no better than Fe particles alone, and that reactivity can be enhanced only by coating Pd on the surface of nano-iron to form bimetallic particles. A comparison of dechlorination of chlorinated methanes by nanoscale Fe, Fe-Pd, and microscale Fe is listed in Table A.4, which reveals that nanoscale Fe-Pd is more effective than nanoscale Fe. Zhang et al. [28, 29, 68] reported successful use of Fe-Pd nanoparticles to dechlorinate chlorinated ethenes, chlorinated ethanes, trichloroethene (TCE), tetrachloroethene (PCE), dichloroethene (DCE) and vinyl chloride (VC). Also, field assessment of TCE, TCA, and PCE with nanoscale Fe-Pd particles was achieved[67].

TABLE A.4. Comparison dechlorination of chlorinated methanes by microscale, nanoscale ZVI and nanoscale Fe-Pd

	Fe load (g/20 mL)	Initial conc. (mg/L)		Reduction time (h)		Percentage reduced (%)		Final products	
		CCl_4	$CHCl_3$	CCl_4	$CHCl_3$	CCl_4	$CHCl_3$	CCl_4	$CHCl_3$
Micro Fe	20	15.9	N/A	72	N/A	>98	N/A	$CHCl_3$ (reduced completely after 100 h) CH_4, CH_2Cl_2	N/A
Nano Fe	0.25	15.86	14.8	20	>80	100	95	CH_4(41%), CH_2Cl_2 (51%)	CH_4(38%), CH_2Cl_2 (59%)
Fe-Pd	0.25	15.4	14.3	1	1	below detection	>98	CH_4 (53% after 2h), CH_2Cl_2 23%)	CH_4 (70%), CH_2Cl_2 (17%)

As mentioned in the characteristic section in this paper, aggregation of nano-iron particles can reduce their reactivity and flow through porous media, thus decrease remediation efficiency. He and Zhao[19] applied water-soluble starch as stabilizer to avoid aggregation of the Fe-Pd nanoparticles. Their results showed that the starch-stabilized Fe-Pd nanoparticles were clearly discrete and well dispersed. The presence of starch (0.2% by weight) prevented aggregation of the nano-iron particles and thus maintained the high surface area and reactivity of the particles. In degradation of TCE, starch-stabilized Fe-Pd nanoparticles showed much greater efficiency and reactivity compared with the non-starch Fe-Pd nanoparticles. At an initial TCE concentration of 52 mg/L and Fe dose of 0.1 g/L, the starch-stabilized Fe-Pd nanoparticles reduced ~98% TCE within 1 h, while the non-starch Fe-Pd nanoparticles eliminated ~78% TCE within 2 h. The reaction rate based on specific surface area was 0.67 $Lh^{-1}m^{-2}$, indicating a pseudo-first-order reaction. While Lien and Zhang[29] reported a reaction rate value of 0.018 $Lh^{-1}m^{-2}$ for their Fe-Pd nanoparticles, where the initial TCE concentration was 20 mg/L and the Fe dose was 5 g/L. the difference between these two reaction rates suggested that the starch stabilizer not only increased the specific surface area, but also greatly enhanced the reactivity of the nanoparticles.

Besides Pd, other noble metals such as Ni and Ag have also been used to treat TCE and chlorinated benzene-contaminated water. Schrick et al.[48] investigated the dechlorination of TCE by Fe-Ni bimetallic nanoscale particles. The results indicated that Fe-Ni nanoparticles were effective in reducing TCE to saturated hydrocarbons. According to their observation, ethylene and butane were the dominant reduction

products in the early stage (35 min), whereas after a much longer time (27 h), the final products were mostly butane, hexane, and octane. With 0.1 g Fe-Ni nanoparticles, 40 ml 1.8×10^{-4} M TCE was reduced below the detection limit within 2 hours. Although the reduction rate was about 1 order of magnitude lower than that of Fe-Pd nanoparticles, Fe-Ni is still competitive, considering that the price of Pd is hundreds of times higher. Compared with Pd, Ag is also a cost-effective substitute in chlorinated organic reduction. Xu et al.[65] investigated the dechlorination of chlorinated benzenes using nanoscale Fe-Ag bimetallic particles. At room temperature, 4 mg/L hexachlorobezene was reduced below detectable limits after 4 days. Tetrachlorobenzene and trichlorobenzene were the most abundant byproducts, accounting for more than 80%. Only a trace amount was degraded to dichlorobenzene.

Clearly, bimetallic nano-iron particles can effectively degrade chlorinated organics. However, because some researchers are afraid they may pose an environmental risk by introducing undesirable metals into groundwater and soil[30], further research is needed.

A.4.1.3 Application of Nanoscale Iron Oxide Particles

Some papers have reported that nanoscale iron oxide particles can be applied to reduce polyhalogenated methanes. As discussed previously, bimetallic nano-iron particles may reduce carbon tetrachloride (CT) effectively, but some of the byproducts are of greater toxicological concern than carbon tetrachloride itself, e.g. chloroform (CF) and dichloromethane (DCM). Evidence from some studies suggested that mixed valence Fe^{II}-Fe^{III} nanoparticles may promote formation of the relatively benign carbine-hydrolysis products such as HCOO[16, 36, 44]. McCormick and Adriaens[36] investigated carbon tetrachloride transformation on the surface of nanoscale biogenic magnetite particles. During their 120-hour experiment, over 93% of CT was reduced, with a significant fraction (~38%) reduced fully to carbon monoxide. Furthermore, an additional 9% of the CT was dechlorinated to CH_4. The experiment of Elsner et al.[16] also indicated a similar result: at pH 7, about 20% of total CT was reduced to CO, and 40% to HCOO$^-$. Under the experimental conditions of Pecher et al.[44], the major products of different polyhalogenated methanes were trihalomethane and formate (HCOO$^-$); however, the amount of HCOO$^-$ (approx. 70%) was much higher than trihalomethane (approx. 35%). Therefore, the larger fraction of relatively benign products of carbon tetrachloride suggested that Fe^{II}-Fe^{III} particles may have beneficial applications in the remediation of CT-contaminated groundwater or soil.

A.4.2 Removal of Metallic Ion

Besides chlorinated organics, metallic ions such as arsenic (As), lead (Pb), and chromium (Cr) are significant threats to the environment and human health. These metallic ions are introduced into the environment through both natural processes

(biochemical reaction, natural erosion, volcanic emissions) and human activities (mining, industrial disposal, coal burning, auto exhaust).

A.4.2.1 Removal of Arsenic

Arsenic is a known carcinogen, and drinking water with high concentrations of As may result in bladder cancer, lung cancer, or skin cancer. The World Health Organization has set a maximum guideline concentration of 0.01 mg/L or 10 ppb for As in drinking water. Recent research [14, 22] on the adsorption of As(III) and As(V) has indicated that nano-iron particles can be effective tools for removing As from groundwater.

Kanel et al.[22] used different concentrations (0.5, 2.5, 5, 7.5, and 10 g/L) of nanoscale ZVI to investigate the adsorption of As(III) (1 mg/L at pH 7) onto the particles' surface. Their results showed that, except for the treatment at 0.5 g/L, more than 80% of total As was adsorbed within 7 min and ~99% within 60 min. Theoretical calculation indicated that the adsorption of As was a pseudo-first-order reaction. The surface-area-normalized rate constants were 0.0057-0.0115 $Lm^{-2}min^{-1}$, 1-3 orders of magnitude higher than for microscale ZVI. The adsorption of As onto nanoscale ZVI followed Freundlich as well as Langmuir isotherms, and the maximum adsorption calculated by Freundlich was 3.5 mg As(III)/g nanoscale ZVI at 25 °C The As adsorption was also effective within a wide range of pH, with the extent of removal 88.6-99.99% at pH 4-10. It was also found that, in the presence of competing anions such as $S_iO_4^{2-}$, HCO_3^-, or PO_4^{3-}, a greater amount of nanoscale ZVI might be required to remove As, since these anions can reduce the As uptake.

Dixit and Hering[14] compared the adsorption of Arsenic (III) and Arsenic(V) onto selected nanoscale iron oxide. Both As(III) and As(V) adsorb strongly onto iron oxide, however, the adsorption behavior of arsenic depends on its oxidation state, experimental conditions, and the mineralogy of the iron oxide. In the pH range of 4-10, the adsorption of As(III) on both amorphous iron oxide and goethite decreased with increasing pH. Also, less As(III) was absorbed at high pH. For As(V), the dependence of adsorption on pH was quite different. With amorphous iron oxide, adsorption showed that the maximum value was between pH 6-9. Adsorption was high with goethite across a wide range of pH, and no pH dependence was observed. With magnetite, the extent of adsorption increased gradually over almost the entire experimental pH range (3.5-10.5). Dixit and Hering also investigated the effects of phosphate, which strongly adsorbs onto iron oxide particles and competes with As for active surface sites. The results showed that, in the presence of phosphate, the fraction of As adsorbed to iron oxide particles was reduced substantially. With amorphous iron oxide, As(V) adsorption at pH 4 decreased from >95% to about 80% and As(III) from 75% to undetectable levels. With goethite, the original adsorption of total As at pH 4 was >90%. In the presence of 100 μM phosphate, As(V) adsorption decreased to 65% and As(III) to 15%.

A.4.2.2 Removal of Chromium and Lead

Chromium and lead are also significant environmental hazards in drinking water. The US EPA has set a maximum limit of 0.1 ml/L for Cr and 0.015 mg/L for Pb. While some studies have examined the reduction of aqueous Cr(VI) and Pb(II) by ZVI, Ponder et al.[45, 46] proved that supported nanoscale ZVI (Ferragels)is more effective.

The supported nanoscale ZVI rapidly separated and immobilized Cr(VI) and Pb(II) from aqueous solutions, reducing Cr(VI) to Cr(III) and Pb(II) to Pb(0), while oxidizing the ZVI to goethite. Based on tests of 0.5 g in contact with 100mL of 50 mM solutions for 8 days, 1.00 g of nanoscale ZVI removed and immobilized 0.12 mM of Cr(VI) and 0.018 mM of Pb(II). Over the 68 days of the experiment, the average removal rate of Cr(VI) was 0.0185 mmol Cr/day/g Fe, 7-12 times greater than with the equivalent weight of commercial microscale iron particles. The rate of removal and immobilization of aqueous Cr(VI) and Pb(II) could be fit to pseudo-first-order reaction kinetics in both the aqueous ion and iron. The apparent rate constant for both Cr(VI) and Pb(II) were >5 times higher than for the commercial microscale ZVI particles, although there was more Fe in the latter. There was a rapid disappearance of Cr(VI) and Pb(II) during the initial stage. For both Cr(VI) and Pb(II), the initial stage appeared to be complete after 10 min. The initial high removal rate and the following slower rate indicated that the mechanism was physical rather than chemical.

A.4.3 Removal of Inorganic Contaminants

A.4.3.1 Removal of Selenium

Selenium-contaminated water is also harmful to human health. According to US EPA regulations, long-term Selenium exposure above maximum contaminant levels has the potential to cause hair and fingernail loss, as well as damage to kidneys, livers, and the nervous and circulatory systems. US EPA has set a maximum contaminant level of 0.05 mg/L for Se as the drinking water standard (from the US EPA website). Previous studies reported that ZVI is an attractive method for removing selenium from aqueous solutions, reducing selenium to elemental Se[38, 39]. Mondal et al.[38] investigated the removal of Se by synthesized nanoscale Fe and Fe-Ni bimetallic particles. During their 5-hour experiment, nearly 100% of selenate was removed by Fe and Fe-Ni particles (although, removal by Fe-Ni particles was greater). At a particle concentration of 0.1 g/L, the Se removal by Fe particles was 155 mg/g, whereas removal by Fe-Ni particles was 225 mg/g. Experimental data at pH 7.7 showed that, for certain Se(VI) concentrations, the removal percentage of both Fe and Fe-Ni particles increased with particle concentration. Specific removal increased with concentrations below 1 g/L of Se. For Fe-Ni bimetallic particles, Ni content also affected Se removal. Under conditions of 0.5 g/L Fe-Ni particles and 50.04 mg/L initial concentration of Se(VI), maximum selenate reduction occurred when the Ni

content in the bimetallic powder was between 30-50%. As for pH, results indicated that high pH limited Se removal. At pH 11, almost no removal was observed, whereas at pH 3.5 and pH 7.7, the total removal was 77.4% and 90%, respectively. The rate kinetics of removal was first-order at low Se concentration, while shifting to zero-order at higher concentrations.

A.4.3.2 Denitrification

As the cultivation of land and the use of artificial fertilizers increase, higher levels of nitrates leach from soil into rivers, lakes, and aquifers. Water highly contaminated by nitrates may be harmful to newborn babies, and it is possible that nitrates contribute to stomach cancer as well.

A couple of technologies have been applied to remove nitrates from water in past years, while ZVI or nanoscale ZVI have emerged only recently as effective alternatives for nitrate removal[7, 9, 51]. Investigating the kinetics of denitrification by nanoscale ZVI, Choe et al.[9] showed that complete denitrification in an aqueous solution can be achieved in a few minutes by bringing the solution into contact with nanoscale ZVI powders under ambient conditions with no pH control. Compared with microscale ZVI, within 30 min the final product was not ammonia but N_2 gas. It was observed that the reaction followed pseudo-first-order with respect to nitrate concentration, and the rate constant was independent of the initial nitrate concentration within the applied concentration range. With respect to Fe dosage, the denitrification approximated a first-order reaction in relatively low Fe dosages (<50 g/L) and a zero-order reaction in high Fe dosages (>50 g/L). Also, the effects of mixing intensity (rpm) on the denitrification rate suggested that the denitrification appeared to be coupled with the oxidative dissolution of iron through a largely mass transport-limited surface reaction (<40 rpm). The kinetics of nitrate reduction was therefore dominated by concentrations of the reactants nitrate and iron in the aqueous solution, as well as by the mixing intensity.

A.4.3.3 Removal of Carbon Monoxide

Nanoscale iron oxide has significant potential as a highly effective catalyst to reduce carbon monoxide, not only because of its small particle size and high surface area, but also because of its dual functions for CO oxidation. In the presence of oxygen, iron oxide reacts as a catalyst of CO oxidation, and in the absence of oxygen, as a direct CO oxidant by losing the lattice oxygen. The final products are relatively benign carbon and carbon dioxide.

Li et al.27 investigated the removal of CO by commercially available ultrafine iron oxide nanoparticles, comparing nanoscale and non-nanoscale Fe_2O_3 as the CO catalyst. In addition, the experiment analyzed nanoscale Fe_2O_3 as a direct CO oxidant. In the first instance, the inlet gas mixture contained 3.44% CO and 20.6% O_2 at a flow rate of 1000 ml/min at 350 °C. 50 mg of nano Fe_2O_3 can catalyze oxidation of almost 100% of CO to CO_2. The calculated reaction constant was $19 s^{-1} m^{-2}$ at 300 °C. The

average activation energy (14.5 kcal mol^{-1}) was larger than the typical activation energy of supported metal catalysts (<10 kcal mol^{-1}). Under identical conditions, the same amount of non-nano Fe_2O_3 can catalyze oxidation of only less than 5% of CO to CO_2. In addition, the initial light off temperature of nano Fe_2O_3 was more than 100 °C lower than that of non-nano Fe_2O_3. A linear relationship between the effluent CO_2 concentration and the inlet CO concentration indicated that the catalytic oxidation of CO was first-order with respect to CO. Also, the increase in O_2 concentration had very little effect on CO_2 production in the effluent gas, which indicated that the reaction order of O_2 was approximately zero. In the absence of O_2, Fe_2O_3 can also behave as a reagent to oxidize CO to CO_2. This property is important in certain potential applications, such as a burning cigarette, where the amount of O_2 is insufficient to oxidize the entire CO present. The reaction of nano Fe_2O_3 with CO in the absence of O_2 is quite complicated. With sequential reductive reactions, Fe_2O_3 can be reduced to FeO, Fe_3O_4, and Fe. Because all of the iron oxides can react with CO, a significant amount of CO will be consumed during the procedure. Furthermore, there was more CO depleted than CO_2 produced, which indicated that there should be carbon deposited on the surface. When the reaction produces CO_2 and carbon deposits, the carbon can also react with Fe to form iron carbides such as Fe_3C or Fe_3C_7, thus deactivating the Fe catalyst. The reaction of CO stops once the Fe is completely transformed to iron carbide, or its surface is completely covered by iron carbide or carbon deposit. The significant amount of CO removed by Fe_2O_3 nanoparticles through the catalytic oxidation, direct oxidation, and the disproportion reactions forming iron carbides make it a very promising material in certain applications, like carbon monoxide removal from auto exhaust and burning cigarette.

A.5. DISCUSSION

Because of their high efficiency in the removal or reduction of contaminants, nano-iron particles have advantages over regular iron-based materials in both in-situ and ex-situ environmental engineering applications. However, further study is needed before widespread adoption of nano-iron particles in environmental engineering. First, although some researchers have offered theories, the reaction mechanisms between nano-iron particles and contaminants in both aqueous and soil phases are still unclear. Secondly, adequate delivery and transport models of nanoparticles in soil and groundwater are critical to engineering applications, yet remain to be developed. Finally, the lifetime of these highly reactive particles will continue to be a significant issue requiring further research.

REFERENCES

1. Baker, C., Hasanain, S.K., Shah, S.I., The magnetic behavior of iron oxide passivated iron nanoparticles, *J. Appl. Phys.*, 96, 6657, 2004.

2. Bokhonov, B., Korchagin, M., The formation of graphite encapsulated metal nanoparticles during mechanical activation and annealing of soot with iron and nickel, *J. Alloys and Compds.*, 333, 308, 2002.

3. Carpenter, E.E., Calvin, S., Stroud, R.M., Harris, V.G., Passivated iron as core-shell nanoparticles, *Chem. Mater.*, 15, 3245, 2003.

4. Carpenter, E.E., Iron nanoparticles as potential magnetic carriers, *J. Magn. Magn. Mater.*, 225, 17, 2001.

5. Chamberlin, R.V., Magnetic relaxation of iron nanoparticles, *J. Appl. Phys.*, 91, 6961, 2002.

6. Chang, Y.C., Chen, D.H., Preparation and adsorption properties of monodisperse chitosan-bound Fe3O4 magnetic nanoparticles for removal of Cu(II) ions, *J. Colloid and Interface Sci.*, 283, 446, 2005

7. Chew, C.F., Zhang, T.C., In-situ remediation of nitrate-contaminated ground water by electrokinetics/iron wall processes, *Water Sci. Technol.*, 38, 135, 1998.

8. Choa, Y.H., Nakayama, T., Sekino, T., Niihara, K., Synthesis and mechanical/magnetic properties of nano-grained iron-oxides prepared with an inert gas condensation and pulse electric current sintering process, *Metals and Materials (Seoul)*, 5, 135, 1999.

9. Choe, S., Chang, Y.Y., Hwang, K.Y., Khim, J., Kinetics of reductive denitrification by nanoscale zero-valent iron, *Chemosphere*, 41, 1307, 2000.

10. Choi, C.J., Dong, X.L., Kim, B.K., Characterization of Fe and Co nanoparticles synthesized by chemical vapor condensation, *Scripta Mater.*, 44, 2225, 2001.

11. Choi, C.J., Dong, X.L., Kim, B.K., Microstructure and magnetic properties of Fe nanoparticles synthesized by chemical vapor condensation. *Mater. Transactions*, 42, 2046, 2001.

12. Dallimore, M.P., Mechanochemical processing - a versatile, low cost technology for the manufacture of nano-powders, *Mater. Technol.*, 14, 4, 1999.

13. Del Bianco, L., Hernando, A., Navarro, E., Pasquini, L., Structural configuration and magnetic effects in as-milled and annealed nanocrystalline, *J. Physique IV: Proceedings*, 8, 107, 1998.

14. Dixit, S., Hering, J.G., Comparison of arsenic (V) and arsenic (III) sorption onto iron oxide minerals: implications for arsenic mobility, *Environ. Sci. Technol.*, 37, 4182, 2003.

15. Elliott, D.W., Zhang, W.X., Field assessment of nanoscale bimetallic particles for groundwater treatment, *Environ. Sci. Technol.*, 35, 4922, 2001.

16. Elsner, M., Haderlein, S. B., Kelerhals, T., Luzi, S., Zwank, L., Angst, W., Schwarzenbach, R.P., Mechanisms and products of surface-mediated reductive dehalogenation of carbon tetrachloride by Fe (II) on goethite, *Environ. Sci. Technol.*, 38, 2058, 2004.

17. Glavee, G. N., Klabunde, K.J., Sorensen, C., Hadjipanayis, G. C., Chemistry of borohydride reduction of iron ( ) and iron ( ) ions in aqueous and nonaqueous media. Formation of nanoscale Fe, FeB and Fe2B powders, *Inorg. Chem.*, 34, 28, 1995.

18. Gleiter, H., Nanocrystalline materials, *Prog. Mater. Sci.*, 33, 223, 1989.

19. He, P., Zhao, D.Y., Preparation and characterization of a new class of starch-stabilized bimetallic nanoparticles for degradation of chlorinated hydrocarbons in water, *Environ. Sci. Technol.*, 39, 3314, 2005.

20. Jiang, W.Q., Yang, H.C., Yang, S.Y., Horng, H.E., Hung, J.C., Chen, Y.C., Hong, C.Y., Preparation and properties of superparamegnetic nanoparticles with narrow size distribution and biocompatible, *J. Magn. Magn. Mater.*, 283, 210, 2004.

21. Johnson, T.L., Scherer, M.M., Tratnyek, P.G., Kinetics of halogenated organic compounds degradation by iron metal, *Environ. Sci. Technol.*, 30, 2634, 1996.

22. Kanel, S.R., Manning, B., Charlet, L., Choi, H., Removal of arsenic (III) from groundwater by nanoscale zero-valent iron, *Environ. Sci. Technol.*, 39, 1291, 2005.

23. Kecskes, L.J., Woodman, R.H., Effect of powder characteristics on the sinterability of microwave-plasma-synthesized iron nanopowders, *Scripta Mater.*, 48, 1041, 2003.

24. Kim, D.K., Zhang, Y., Voit, W., Rao, K.V., Kehr, J., Bjelke, B., Muhammed, M., Superparamegnetic iron oxide nanoparticles for bio-medical applications, *Scripta Mater.*, 44, 1713, 2001.

25. Klabunde, K.J., Stark, J., Koper, O., Mohs, C., Park, D. G., Decker, S., Jiang, Y., Lagadic, I., Zhang, D., Nanocrystals as stoichiometric reagents with unique surface chemistry, *J. Phys. Chem.*, 100, 12142, 1996.

26. Li, F., Vipulanandan, C., Mohanty, K.K., Microemulsion and solution approaches to nanoparticle iron production for degradation of trichloroethylene, *Colloid Surf. A: Physicochem. Eng.*, 223, 103, 2003.

27. Li, P., Miser, D.E., Rabiei, S., Yadav, R.T., The removal of carbon monoxide by iron oxide nanoparticles, *Appl. Catal. B: Environmental*, 43, 151, 2003.

28. Lien, H.L., Zhang, W.X., Hydrodechlorination of chlorinated ethanes by nanoscale Pd/Fe bimetallic particles, *J. Environ. Eng.*, 131, 4, 2005.

29. Lien, H.L., Zhang, W.X., Nanoscale iron particles for complete reduction of chlorinated ethenes, *Colloid Surf. A:*, 191, 97, 2001.

30. Lien, H.L., Zhang, W.X., Transformation of chlorinated methanes by nanoscale iron particles, *J. Environ. Eng.*, 125, 1042, 1999.

31. Liu, Y.Q., Majetich, S.A., Tilton, R.D., Sholl, D.S., Lowry, G.V., TCE dechlorination rates, pathways, and efficiency of nanoscale iron particles with different properties, *Environ. Sci. Technol.*, 39, 1338, 2005.

32. Liu, Z.L., Wang, H.B., Lu, Q.H., Du, G.H., Peng, L., Du, Y.Q., Zhang, S.M., Yao, K.L., Synthesis and characterization of ultrafine well-dispersed magnetic nanoparticles, *J. Magn. Magn. Mater.*, 283, 258, 2004.

33. Lowry, G.V., Johnson, K.M., Congener-specific dechlorination of dissolved PCBs by microscale and nanoscale zero valent iron in a water/methanol solution, *Environ. Sci. Technol.*, 38, 5208, 2004.

34. Makela, J.M., Keskinen, H., Forsblom, T., Keskinen, J., Generation of metal and metal oxide nanoparticles by liquid flame spray process, *J. Mater. Sci.*, 39, 2783, 2004.

35. Malow, T.R., Koch, C.C., Miraglia, P.Q., Murty, K.L., Compressive mechanical behavior of nanocrystalline Fe investigated with an automated ball indentation technique, *Mater. Sci. Eng.*, A252, 36, 1998.

36. McCormick, M.L., Adriaens, P., Carbon tetrachloride transformation on the surface of nanoscale biogenic magnetite particles, *Environ. Sci. Technol.*, 38, 1045, 2004.

37. Miehr, R., Tratnyek, P.G., Bandstra, J.Z., Scherer, M.M., Alowitz, M.J., Bylaska, E.J., Diversity of contaminant reduction reactions by zero valent iron: role of the reductate, *Environ. Sci. Technol.*, 38, 139, 2004.

38. Mondal, K., Jegadeesan, G., Lelvani, S.B., Removal of selenate by Fe and NiFe nanosized particles, *Ind. Eng. Chem. Res.*, 43, 4922, 2004.

39. Morrison, S.J., Metzler, D.R., Dwyer, B.P., Removal of As, Mn, Mo, Se, U, V and Zn from groundwater by zero-valent iron in a passive treatment cell: reaction progress modeling, *J. Contam. Hydrol.*, 56, 99, 2002.

40. Nakayama ,T., Yamamoto, T.A., Choa, Y. H., Niihara, K., Synthesis and magnetic properties of nanocluster composite, *Ceramic Transactions*, 108, 257, 2000.

41. Nakayama, T., Choa, Y. H., Yamamoto, T. A., Niihara, K., Nanocrystalline iron oxide manufactured by IGC-PECS process, *Funtai oyobi Funmatsu Yakin*, 45, 1207, 1998.

42. Natter, H., Schmelzer, M., Loffler, M.S., Krill, C.E., Fitch, A., Hempelmann, R., Grain-growth kinetics of nanocrystalline iron studied in situ by synchrotron real-time X-ray diffraction, *J. Phys. Chem. B:*, 104, 2467, 2000.

43. Nurmi, J.T., Tratnyek, P.G., Sarathy, V., Baer, D.R., Amonette, J.E., Characterization and properties of metallic iron nanoparticles: spectroscopy, electrochemistry, and kinetics, *Environ. Sci. Technol.*, 39, 1221, 2005.

44. Pecher, K., Haderlein, S.B., Schwarzenbach, R.P., Reduction of polyhalogenated methanes by surface-bound Fe (II) in aqueous suspensions of iron oxide, *Environ. Sci. Technol.*, 36, 1734, 2002

45. Ponder, S.M., Darab, J.G., Bucher, J., Caulder, D., Craig, I., Davis, L., Edelstein, N., Lukens, W., Nitsche, H., Rao, L.F., Shuh, D.K., Mallouk, T.E., Surface chemistry and electrochemistry of supported zero-valent iron nanoparticles in the remediation of aqueous metal contaminants, *Chem. Mater.*, 13, 479, 2001.

46. Ponder, S.M., Darab, J.G., Mallouk, T.E., Remediation of Cr (IV) and Pb(II) aqueous solutions using supported, nanoscale zero-valent iron, *Environ. Sci. Technol.*, 34, 2564, 2000.

47. Sanchez-Lopez, J.C., Justo, A., Fernandez, A., Conde, C.F., Conde, A., Preparation and thermal evolution of vapor-condensed nanocrystalline iron, *Philosophical Magazine B: Phys. of Condens. Matter.*, 76, 663, 1997.

48. Schrick, B., Blough, J.L., Jones, A.D., Mallouk, T.E., Hydrodechlorination of trichloroethylene to hydrocarbons using bimetallic nickel-iron nanoparticles, *Chem. Mater.*, 14, 5140, 2002.

49. Schrick, B., Hydutsky, B. W., Blough J. L., Mallouk, T. E., Delivery vehicles for zerovalent metal nanoparticles in soil and groundwater, *Chem. Mater.*, 16, 2187, 2004.

50. Si, P.Z., Brueck, E., Zhang, Z.D., Tegus, O., Buschow, K.H. J., Zhang, W.S., Klaasse, J.C. P., de Boer, F.R., Synthesis, structure, and magnetic properties of Fe-Gd nanocapsules coated with B_2O_3/H_3BO_3 and Fe_3BO_5-$GdBO_3$, *Physica B: Condens. Matter.*, 353, 1, 2004.

51.Siantar, D.P., Schreier, C.G., Chou, S.S., Reinhard, M., Treatment of 1, 2-dibromo-3-chloropropane and nitrate-contaminated water with zero-valent iron or hydrogen/palladium catalysts, *Water Res.*, 30, 2315, 1996.

52. Signoretti, S., Del Bianco, L., Pasquini, L., Matteucci, G., Beeli, C., Bonetti, E., Electron holography of gas-phase condensed Fe nanoparticles, *J. Magn. Magn. Mater.*, 262, 142, 2003.

53. Signorini, L., Pasquini, L., Savini, L., Carboni, R., Boscherini F., Bonetti E., Giglia, A., Pedio, M., Mahne N., Nannarone S., Size-dependent oxidation in iron/iron oxide core-shell nanoparticles. *Phys. Rev. B*, 68, 195423, 2003.

54. Song, G.P., Bo, J., Guo, R., The characterization and property of polystyrene compounding of α-Fe_2O_3 in the nano-scale, *Colloid Polym. Sci.*, 282, 656, 2004

55. Sudakar, C., Kutty, T.R.N., Structural and magnetic characteristics of cobalt ferrite-coated nano-fibrous γ-Fe_2O_3, *J. Magn. Magn. Mater.*, 279, 363, 2004.

56. Sus-Ryszkowska, M., Wejrzanowski, T., Pakiela, Z., Kurzydlowski, K. J., Microstructure of ECAP severely deformed iron and its mechanical properties, *Mater. Sci. Eng.*, A369, 151, 2004.

57. Tao, N.R., Sui, M.L., Lu, J., Lu, K., Surface nanocrystallization of iron induced by ultrasonic shot peening, *Nano Struc. Mater.*, 11, 433, 1999.

58. Teng, X.W., Yang, H., Synthesis of face-centered tetragonal FePt nanoparticles and granular films from Pt@ Fe$_2$O$_3$ core-shell nanoparticles, *J. American Chem. Soc.*, 125, 14559, 2003.

59. Uegami, M., Kawano, J., Kakuya, K., Okita, T., Okinaka, K., Iron composite particles for purifying soil or groundwater. *European Patent Application*, 2004.

60. Valiev, R.Z., Islamgaliev, R.K., Alexandrov, I.V., Bulk nanostructured materials from severe plastic deformation, *Prog. Mater. Sci.*, 45, 103, 2000.

61. Wang, C.B., Zhang, W.X., Synthesizing nanoscale iron particles for rapid and complete dechlorination TCE and PEBs, *Environ. Sci. Technol.*, 31, 2154, 1997.

62. Wang, H.B., Wang, X.Y., Zhang, J.H., Xu, Z.Y., Internal friction of nano-grained Fe-25%Ni alloy bulk, *Jinshu Xuebao*, 40, 523, 2004.

63. Wang, Z.H., Choi, C.J., Kim, B. K., Kim, J. C., Zhang, Z.D., Microstructure and magnetic property of Fe-Co nanoparticles prepared by chemical vapor condensation process, *J. Alloys and Compds.*, 351, 319, 2003.

64. Wiggins, J., Carpenter, E.E., O'Connor, C.J., Phenomenological magnetic modeling of Au:Fe:Au nano-onions, *J. Appl. Phys.*, 87, 5651, 2000.

65. Xu, Y., Zhang, W.X., Subcolloidal Fe/Ag particles for reductive dehalogenation of chlorinated benzenes, *Ind. Eng. Chem. Res.*, 39, 2238, 2000.

66. Zavaliche, F., Bensebaa, F., L'Ecuyer, P., Veres, T., Cochrane, R.W., The role of non-collinear spins on the magnetic properties of uncoupled nanometer-size particles, *J. Magn. Magn. Mater.*, 285, 204, 2005.

67. Zhang, W.X., Nanoscale iron particles for environmental remediation: an overview, *J. Nanoparticle Res.*, 5, 323, 2003.

68. Zhang, W.X., Wang, C.B., Lien, H.L., Treatment of chlorinated organic contaminants with nanoscale bimetallic particles, *Catalysis Today*, 40, 387, 1998.